ISSN: •2708-6437(Online)
•2708-6429(Print)

Journal of Engineering Advancements

Editor-in-Chief:

Prof. Dr. Mohammad Mashud

Volume 04 Issue 03

SciEn

Published by:
SciEn Publishing Group

Journal of Engineering Advancements
Apt. # 6 C-D, House # 191
Road # 12/A, Dhanmondi R/A
Dhaka-1209, Bangladesh
Email: jea@scienpg.com Website: www.scienpg.com/jea/

SciEn

Published in: September 2023
Published by: SciEn Publishing Group

Price: Each Issue BDT 200.00 (US$ 15) **ISSN:** 2708-6437 (Online) 2708-6429 (Print)

Journal of Engineering Advancements
Apt. # 6 C-D, House # 191
Road # 12/A, Dhanmondi R/A
Dhaka-1209, Bangladesh
Email: jea@scienpg.com Website: www.scienpg.com/jea/

Journal of Engineering Advancements

Volume 04, Issue 03 September 2023

CONTENTS

Original Articles

Journal of Engineering Advancements

SciEn

Published by: SciEn Publishing Group

Apt. # 6 C-D, House # 191, Road # 12/A
Dhanmondi, Dhaka-1209, Bangladesh
Email Address: jea@scienpg.com

www.scienpg.com/jea/

This page is left intentionally blank

SciEn
Journal of Engineering Advancements Vol. 04(03) 2023, pp 57-63 https://doi.org/10.38032/jea.2023.03.001

An Investigation on Effects of In-Leaf and Out-of-Leaf Conditions on Propagated Radio Broadcast FM Signal

Aderemi Temitayo Adesanya and Julius Jide Popoola*

Department of Electrical and Electronics Engineering, Federal University of Technology Akure (FUTA), Ondo State, Nigeria

Received: April 06, 2023, Revised: July 21, 2023, Accepted: July 26, 2023, Available Online: August 14, 2023

ABSTRACT

The daily increasing desire for the right information at any place, anytime, and anywhere by people has made broadcast media indispensable media for disseminating information to the public. Propagation models are deployed in planning and designing wireless communication systems. Different environments do require a unique propagation model. In this paper, least squares regression analysis was utilized to create the path loss models for the in-leaf and out-of-leaf conditions of a teak (Tectona grandis) plantation. The developed model was found to be more suitable compared to the existing Weissberger's and COST235 models because it gives the least difference in root mean square error of 3.9 dB in the two scenarios compared to COST 234 and Weissberger, which stand at 11.2 dB and 10.8 dB, respectively, and the developed model was closer to the assessed path loss obtained from the measurement carried out. The results of the study establish a standard model that can be deployed in the effective planning and design of wireless communication links for very high bands within the radial distance in the tropical rain forest of 30m to 45m foliage depth. This study confirms the need for distinctive models for radio signals at different locations under different conditions.

Keywords: Propagation Model, Path Loss, Root Mean Square Error, FM, Coverage Areas.

1 Introduction

The wireless signal strength of propagated radio waves from the transmitter to the receiver usually decreases as the distance between the transmitter and the receiver increases [1]. This is because, in a wireless communication system, the transmission and reception of radio signals through the wireless channel are usually affected by both environmental and physical factors. These environmental and physical or geographical factors negatively affect the maximum range of the signal as well as limit the quality of service (QoS) of the communication system [2]. This is because as the radio signal propagates outwardly from the transmitting antenna, the radio signal strength is dispersed over an increasingly greater area, which causes the radio signal to attenuate as it travels away from the transmitter. This attenuation grows gradually with distance, resulting in a rapid reduction in radio signal strength as the signal propagates far from the transmitting antenna. The presence of vegetation along the radio propagation path has been observed as one of the environmental factors causing significant attenuation of radio signals propagated from radio stations. In addition, the presence of vegetation along the radio propagation path has been observed as the major problem responsible for much of the reduction in the radio signal coverage area or range [3]. This reduction in radio signal coverage range, or attenuation, occurs normally as a result of scattering, absorption, reflection, and diffraction, which propagated radio signals usually suffer from when traveling from the transmitter to the receiver [1],[2]. As reported by these authors, reflection, diffraction, and scattering are major propagation mechanisms that impact radio wave propagation in wireless communication.

In wireless communication, radio signal reflection occurs when a propagating radio wave impinges upon an obstruction or obstacle that has very large dimensions compared to the wavelength of the propagating radio wave. On the other hand, diffraction happens when an electromagnetic wave that is traveling between the transmitter and receiver comes into contact with an obstruction that is impermeable and larger than the wavelength of the propagating electromagnetic wave [4]. According to Huygen's principle, secondary waves are produced behind the obstructing body even though the transmitter and receiver are not in the line of sight (LOS) [5]. Primarily, diffraction explains how radio waves travel in both rural and urban environments without LOS paths. This process, according to [4], is also called shadowing since the diffracted wave can reach a receiver even when it is shadowed by any obstruction. Similarly, scattering occurs when the medium through which the electromagnetic wave travels or propagates consists of obstacles with dimensions that are small compared to the wavelength of the propagation signal. Most often, as reported by [5], scattered waves are usually produced by rough surfaces, small obstacles, or irregularities in the channel. In addition, in practice, vegetation, lampposts, street signs, and stairs within buildings can induce scattering in radio communication signals. According to [6], quantitative knowledge of the excess propagation loss experienced by radio signals due to the presence of leaves or foliage is important in planning a communication link in any vegetated channel. Research conducted by [7] on individual trees revealed that as trees develop leaves, there is an increase in the additional attenuation observed across them. The study observed a significant difference in propagation loss between the states when the tree is in-leaf compared to when it is out-of-leaf, which is primarily attributed to the presence of leaves. Furthermore, the experiment demonstrated that when the tree is in full leaf condition, leaves contribute to a larger percentage of the overall attenuation. However, the research did not explicitly state that leaves have a substantial impact on radio waves, especially at microwave frequencies. To predict the best behavior of radio

*Corresponding Author Email Address: remtex7070@gmail.com

broadcast FM signals in Teak (*Tectona grandis*) plantations, a propagation model was created using three existing FM (modulation) broadcasting stations in Ondo State, Nigeria. The study involved assessments and measurements of the three FM radio station signals and the modeling of an appropriate model for in-leaf and out-of-leaf. Condition. The effectiveness of radio propagation is determined by essential factors such as distance, transmission power, antenna gain, and terrain. To ensure optimal signal quality within their coverage area, radio stations must have knowledge of the terrain. This understanding is crucial for enhancing the signal quality and meeting the recommended signal levels of 60 dB for urban FM broadcasting stations and 48 dB for rural FM broadcasting stations, as outlined in the 5th edition of the Nigerian broadcasting code [8]. Moreover, radio stations should consider the reduction in signal strength during the rainy season, which typically ranges between 3 and 5 dB compared to the dry season [9]. Therefore, for the planning and designing of radio stations and wireless communication systems located within the tropical rainforest region covered by this study, they can predict propagation loss for their service area using the path loss model developed in this study. Section 3 provides all-inclusive information on all the steps taken to complete the study. The remainder of the work is arranged as follows for both a reasonable and sequential presentation: A quick summary of the important material is presented in Section 2. Section 3 provides wide-ranging information on the method used to conduct the study. In Section 4, the results are given and discussed, and Section 5 concludes the study with a summary of the results.

2 Concept and Evaluation of Related Studies

The propagation model is a mathematical formula that empirically describes how radio wave propagation changes with frequency, distance, and other factors [10]. Since the route loss experienced along any radio link is the most important factor in determining the propagation of the link, radio propagation models frequently focus on predicting the area of coverage for a transmitter or modeling the distribution of signals over different places. [2],[4] opined that radio propagation models play a vital role in designing wireless communication systems and employed least squares regression analysis to develop a versatile propagation model for very high-frequency broadcasting radio stations in vegetation and/or rocky environments. The developed model was later evaluated by comparing its path loss prediction result with two existing path loss models in the literature. The results of the comparative performance analyses show that the two existing models predict the highest difference in propagation path loss compared with that from the developed least squares regression model. The generated model outperformed the projected value favorably for every route and the whole coverage area of the transmitter station used as a case study, according to the comparison between the two. Also, the study's findings support those of other researchers who have concluded that no single propagation model can perfectly account for all topographies, uses, and environments. [11] Carried out exponential models of the signal strength of a television station in Nigeria. In the paper, the line of sight and signal strength of ultra-high frequency (UHF) television signals in Osun State, Nigeria, were investigated. Regression analysis was performed to identify the exponential models that may be used to calculate signal strength for a given line of sight at the authorized routes in the state after propagation curves for the signal along various routes were plotted. However, the work covers much of the urban centers [10]. A study on the electric field strength distribution of UHF television signal propagation in Ekiti State Adopting the free space path loss model, the findings show the field strength distribution of the broadcasting station in major towns and villages, its elevation pattern, and the many levels of coverage that its residents can access there. Fagbohun is silent on the propagation through foliage accuracy and reliability prediction model for microcellular urban propagation environments; the work is mainly for mobile wireless networks. [12] Carried out a comparative analysis of path loss prediction models for urban microcellular environments. Path losses were predicted using the three path loss prediction models: free space, Hata, and Egli. The estimated route loss values and actual measured data from a Visafone base station in Uyo, Nigeria, were contrasted. According to the comparative analysis, free space, Hata, and Egli had mean square errors (MSE) of 16.24 dB, 2.37 dB, and 8.40 dB, respectively. According to the findings, Hata's model is the most. [9] In a review of radio wave constriction in forest environments, the classic analytical methods of propagation loss modeling and prediction are described first. And suggest that the difference in path loss for trees in-leaf and out-of-leaf is about 3 to 8 dB in the UHF and VHF bands. This provides data on the physical processes that radio waves undergo when propagating through a forest. However, the paper does not specify the specific woodland. In order to determine the RF loss through packed eucalyptus leaves as a function of the effective water path of the waves at a frequency of 2.4 GHz, [13] developed a plane wave model that includes a calculation of the water content of leaves. When the water content of the leaves is given as an effective water path (EWP) in millimeters, there is a positive non-linear connection between the RF loss in decibels (dB) and the latter. It was suggested that more research be done to connect this mathematical model of radio propagation to actual measurements of water content and RF loss through whole trees with a view to evaluating plant water status for monitoring plant physiology. [14] Carried out experimental studies of radio wave attenuation were carried out in a tomato greenhouse using a network of wireless sensors that sent a signal in the 2.4 GHz ISM band. There is a sizable margin of uncertainty between the recorded attenuation data and the values of the current empirical vegetation attenuation models. A regularized regression approach based on the modified exponential decay model (EDM) was used to reduce the number of variables and construct an empirical model. Unlike Weissberger's model, which included the height of the nodes' antennas (both for transmitting and receiving), this model is more straightforward since, as predicted, the height variable has a greater influence on attenuation than the distance variable. It was advocated that to utilize new empirical models and to understand how the model will act if the device moves in accordance with a particular plant development, it is critical to explore the compensating component of the suggested modified equation derived from the modified exponential decay model (MED) in future studies. The proposed empirical foliage loss models for the horizontal propagation path can be classified as the modified exponential decay (MED) models, as well as the Weissberger model [15]. ITU Recommendation (ITU-R) model [16], the COST235 model, the fitted ITU-R (FITU-R) Model [17], the modified gradient model, such as the maximum attenuation (MA) model, the nonzero gradient (NZG) model, and the dual gradient (DG) model The exponential decay model was first proposed by Weissberger, and its main modified versions include the ITU-R model, the COST235 model, and the FITU-R model. In general, the exponential decay model, as reported in [12], is expressed in Eq. (1).

$$L(dB) = A * F^B * {d_t}^c \tag{1}$$

F stands for frequency in MHz, and d is the depth of the tree in meters. Where A, B, and C are the fitted parameters from a variety of experiments with regression techniques. Depending on the frequency, kind of foliage, and propagation methods, among other factors, many parameter values have been suggested. The

Table 1 lists the distinguishing information about the three FM radio stations' transmitters, including their site coordinates, transmitter frequency, transmitter aerial height, and other relevant details. Experimental Set-up and Measurement Techniques

For the three radio station coverage zones, site surveys and route planning were done. The elevation and latitude of each location where measurements were collected were determined using the Germin GPSMAP 78s Global Positioning System. The line-of-sight distance (in km) to the transmitting antenna was also calculated using this information. A BC-1173 field strength meter and a 10 dB gain 75-ohm dipole antenna were used to test the strength of the signal. Adaba 88.9 FM's transmitter output power was kept constant (upon request) at 15 kW, and Orange FM's transmitter output power was kept at 15 kW. The received signal strength was measured between the hours of 8 a.m. and 6 p.m. each day between the months of December and June, at a height of 6 feet above the ground. Six measurements were taken at the same location each month, each no more than 5 km apart. The data collection at the Teak (*Tectona grandis*) Plantation is depicted in Fig. 2.

simplicity of the exponential decay model is a plus, but a significant disadvantage is that [18] findings about measurement geometry and foliage size are ignored.

3 Methodology

The steps employed in this study are presented in Fig. 1.

3.1 Data Collection

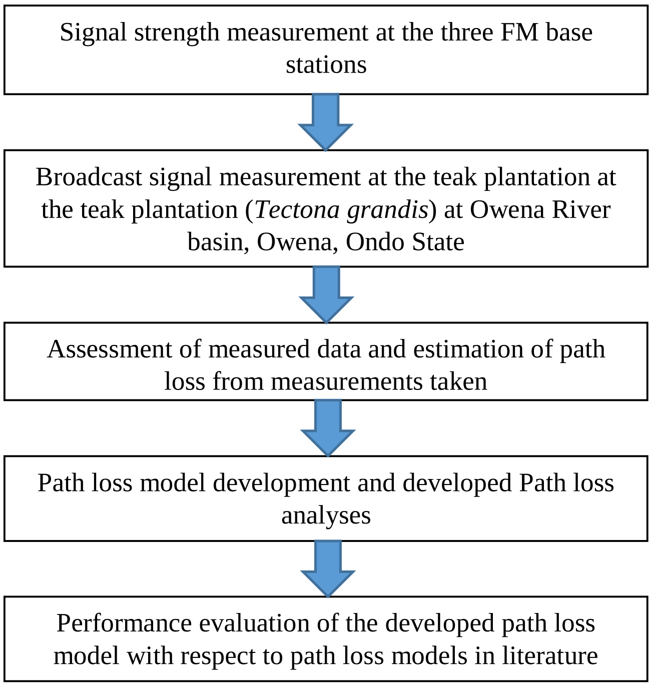

Fig. 1 Research Methodology

Table 1 Transmitter Data

S/N	PARAMETER	ADABA FM	ORANGE FM	POSITIVE FM
1	Frequency of operation	88.9 FM	94.5MHz	102.5MHz
2	Frequency Bandwidth	200 kHz	300 KHz	500 KHz
3	Transmitter Power(maximum)	35 KW	35 KW	35 KW
4	Transmitting Power (actual)	25 kW (71%)	15 kW	15 kW
5	Maximum Deviation	295 kHz	250 kHz	220 kHz
6	Antenna Gain	85.6 dB	96.8dB	98.6 dB
7	Antenna Polarization	Vertical	Vertical	Vertical
8	Antenna Maximum Height	250m(800ft)	150m(500ft)	200m(700ft)
9	Maximum elevation	427m	276m	482m
10	Coordinates	LAT7.324390, LON 5.125180	LAT 7.29025 LON5.193556	LAT 7.253056 LON 5.131083

(a)

(b)

Fig. 2 (a) Out-Of-Leaf Data Measurement at the Teak Plantation (*Tectona Grandis*) (b) In-Leaf Data Measurement at the Teak Plantation (*Tectona Grandis*)

3.2 Path Loss Model Development for Conditions for Being In and Out of Leaf

Radio signal travels through the Teak (*Tectona grandis*) tree plantation as well as the ground-level bushes in forest zones, there is significant restriction and spreading of the transmitted radio signal to the headset. The signal will be significantly constrained because of potential communication connection incursions this is frequently overlooked when designing communication frameworks. In the absence of moisture, the Teak (*Tectona grandis*) tree plantation foliage offers little resistance, but following rainstorms, the trees in the plantation and other elements of the Teak (*Tectona grandis*) tree plantation mature. This affects how the wave is attenuated when it passes through the Teak (*Tectona grandis*) tree plantation. Following the broad contours of the optimization technique and learning from the analysis of the previously established model [9], the surplus Eq. (2) represents the extra attenuation caused by the Teak (*Tectona grandis*) tree plantation.

$$P_l = A * f^B * {d_t}^c \tag{2}$$

Based on observed data from the three FM radio stations used at 88.9 MHz, 94.5 MHz, and 102.5 MHz, the three variables A, B, and C in Eq. (2) were experimentally optimized by least squares regression techniques. Since measurements made in the plantation of teak (Tectona grandis) trees reveal a linear connection between the relevant LOS due to distance and the projected project signal loss, stands for the frequency of operation, stands for the teak (Tectona grandis) depth in meters, and is propagation loss.

3.2.1 Out-of-Leaf Propagation Model

The empirically optimized constants through least squares regression methods of the out-of-leaf measured data are shown in Eq. (3).

$$P_{l(out\ of\ leaf)} = 0.5934 * f^{0.2441} * {d_t}^{0.9840} \tag{3}$$

3.2.2 In-Leaf Propagation Model

The empirically optimized constants through regression methods of the in-leaves measured data are shown in Eq. (4).

$$P_{l(in\ leaf)} = 0.6213 * f^{0.5440} * {d_t}^{0.6443} \tag{4}$$

It is necessary to establish how much the signal loss propagation model hinges on other factors, such as the operational frequency, the location, and the depth of the Teak (*Tectona grandis*) tree plantation. The difference between the signal strength predicted by the developed model and the actual signal recorded in this dependency is measured by the root mean square error (RMSE). By comparing the anticipated errors of the various propagation models with the supplied measurement data, accuracy is evaluated. The computed RMSE values were derived using Eq. (5).

$$S = \sqrt{\frac{\Sigma_{i=1}^{K}(P-M)^2}{k}} \tag{5}$$

Thus, for a total of k data points, P stands for the developed model value, and M is the measured data of propagation loss *i*.

3.3 Propagation Model in Literature

The following traditional path loss models are contrasted with the measurement-based path loss model developed in this study.

3.3.1 Weissberger Model and COST 235 Model

When a signal path is obstructed by dense, arid, in-leaf trees prevalent in temperate locations, Weissberger's modified exponential decay model is suitable [9],[15] and is stated in Eqs. (6) and (7) [9]. Also applicable is the COST235 model, as stated in Eqs. (8) and (9) [19].

Out of Leaf

$$P_{ld} = 1.33 * f^{0.284} * {d_t}^{0.588} \tag{6}$$

In-Leaf

$$P_{fW} = 0.45 * f^{0.284} * d_t \tag{7}$$

Out-of-Leaf

$$P_{ld} = 26.6 * f^{-0.2} * {d_t}^{0.5} \tag{8}$$

In-Leaf

$$P_{fW} = 15.6 * f^{-0.009} * {d_t}^{0.26} \tag{9}$$

4 Results and Discussion

The standard evaluation tests conducted on the developed propagation model are covered in this section. There are two broad classifications for the tests. The tests used to gauge how well the developed model performed when applied under the in-leaf and out-of-leaf circumstances of the Teak (*Tectona grandis*) tree plantation make up the first class. Subsection 4.1 provides the results of these evaluations. The second phase of the performance evaluation test that was carried out included a comparison of the developed propagation path loss, estimated results from the developed model, and two more models from the literature.

4.1 Measurement Analysis

By correlating the path loss estimation with the path loss that was observed during measurement in the Teak (*Tectona grandis*) tree plantation, the performance of the developed propagation model was evaluated in this subsection. The extracted results from the measured data were used to plot the graph for the three radio stations.

Their assessment of the measured signal data was done to determine the level of obstruction by the Teak (*Tectona grandis*) trees along the LOS of the three radio station signals. From Fig.

3, Fig. 4, and Fig. 5, it is clear that both measured and estimated data obey the Friis transmission Eq. (10) [20].

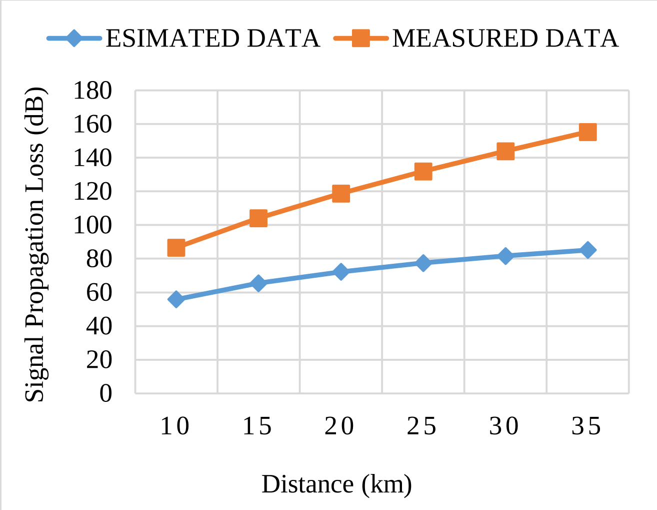

Fig. 3 Adaba FM Signal Propagation Loss

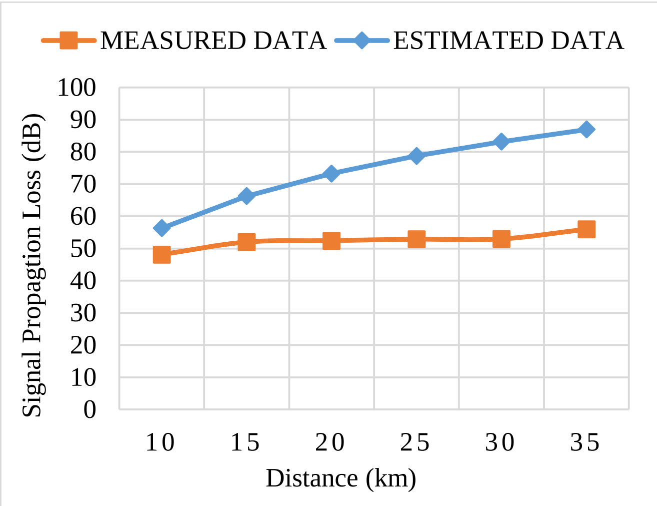

Fig. 4 Orange FM Signal Propagation Loss

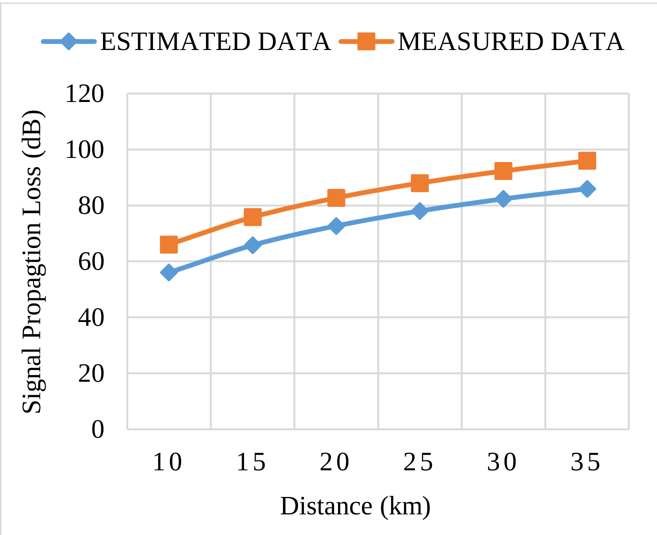

Fig. 5 Positive FM Signal Propagation Loss

The developed model prediction estimates are congruent with the estimated data from measurements.

$$P_l = 10\ log\left(\frac{4\pi d}{\lambda}\right) \tag{10}$$

When representing the reduction in signal strength caused by distance, this cluster dataset does not provide a precise depiction of what occurs under the two distinct situations of the teak trees' in-leaf and out-of-leaf circumstances at the Owena Dam River Basin.

4.2 Assessment of the Developed In-Leaves and Out-of-Leaf Model

By contrasting the model that was created with the existing Weissberger and COST235 models, the model that was developed was validated. The model that was created was applied to the teak (*Tectona grandis*) plantation in the Owena Dam River Basin of Ondo State to determine the route loss with the help of the canopy under the distinct circumstances of in and out-of-leaf.

And all were subjected to the root mean square error test. When regression analysis is performed, the result is a model that predicts the value of the response variable based on the value of the predictor variable. Calculating the root mean square error, a statistic that shows how far projected values are from the observed values on average, is one technique used to judge how "well" the model fits a specific dataset of the Teak (*Tectona grandis*) plantation at the Owena Dam River Basin of Ondo State and other similar environments.

4.2.1 In-Leaf Model Assessment

There's a slow degradation or dissipation of the signal with increasing depth of the teak (*Tectona grandis*) plantation due to the thickening of the teak tree foliage canopy disturbing point-to-point connection or direct or line-of-sight communication and shading the radio waves from the receiver antenna. For the in-leaf model, the values of variables A, B, and C in the preceding model Eq. (2) have been correspondingly regulated to 0.2113, 0.5644, and 0.6733. Observations reveal that when the teak (*Tectona grandis*) has enough leaf on its branches during the time of year when it rains, the variation that was found in the calculated path loss has been addressed, as shown in Fig. 5. The computed RMS error is 11.3 dB between the developed model predictions and the actual recorded data. When compared to the recorded data, COST 234 and Weissberger yield respectively 15.7 dB and 11.6 dB. Fig. 5 shows the measured data, the decay model, and the developed model. This demonstrates that the created model works better in the teak (*Tectona grandis*) plantation's in-leaf circumstances.

4.2.2 Out-of-Leaf Model Assessment

When there is no rain or during the dry season, the foliage provides little resistance. Hence, there is little disturbance to point-to-point connection, direct or line-of-sight communication, and shading of the radio waves from the receiver's antenna. The values of variables A, B, and C in the preceding model Eq. (2) have been correspondingly regulated and Fig. 6 illustrates how the developed model performs admirably in contrast to COST 234 and Weissberger. Calculations show that there is an RMSE error of 7.4 dB between the model predictions and the measured dataset. When compared to the observed data, COST 234 and Weissberger yield 4.5 dB and 22.4 dB, respectively. Fig. 7 shows the observed data, the decay model, and the created model. The variance in RMSE value of the developed model plants in and out-of-leaf circumstances in the teak (Tectona grandis) plantation at the Owena Dam River Basin of Ondo State, when contrasted with COST 234 and Weissberger, which stand at 11.2 dB and 10.8 dB, respectively, This demonstrates the developed model's superior performance in both situations as well as across the teak tree's diverse depths, which is proof of its appropriateness for these species of trees in the tropical rain forest.

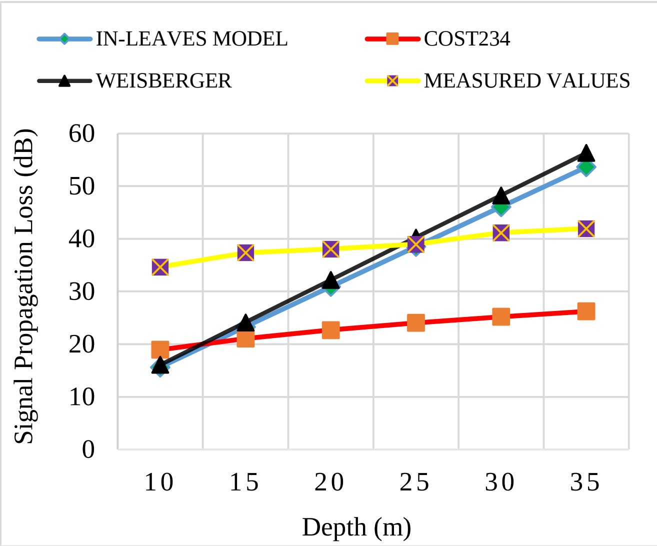

Fig. 6 In-Leaf Propagation Loss

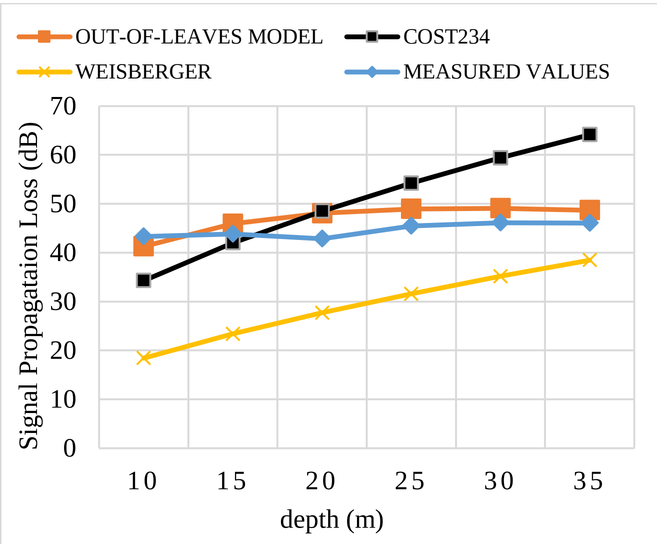

Fig. 7 Out-Of-Leaf Propagation Loss

4.2.3 Propagation Loss for Three FM Stations

To assess the level of impact of obstruction by the teak (*Tectona grandis*) tree plantation at the Owena River Basin of Ondo State on the three FM station signals used as the case study for this research along the line-of-sight path of the radio station signals and confirm the usefulness of the developed model. The developed in-leaf and out-of-leaf propagation models were applied to the data set of three FM stations used for this study. Fig. 8 illustrates how the depth and amount of foliage in the teak (*Tectona grandis*) tree plantation affect the amount of attenuation that occurs there when the teak (*Tectona grandis*) tree plantation is in its in-leaf state. The three FM stations behave quite differently when the plantation is not in leaf, as shown in Fig. 9, and the amount of attenuation is significantly lower than it was when the plantation was fully covered in foliage. In both the in-leaf and out-of-leaf circumstances, the newly developed prediction model performed better than the COST 234 and Weissberger models. Its root mean square error difference was just 3. 9 dB, compared to discrepancies of 11. 2 dB and 10. 8 dB for the COST 234 and Weissberger models, respectively.

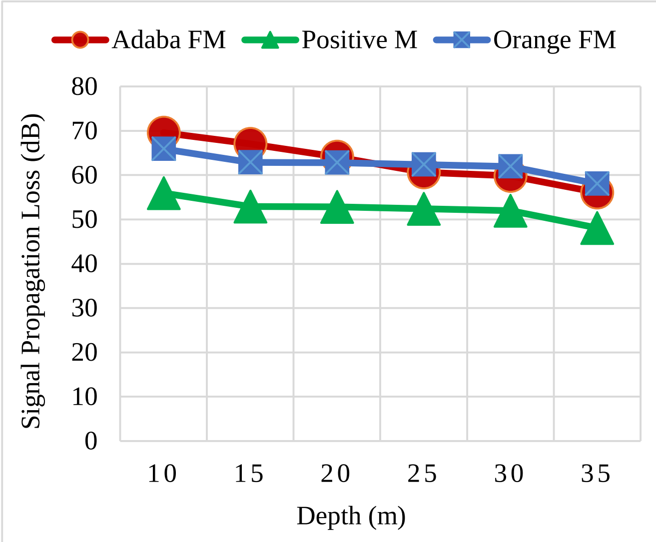

Fig. 8 In-Leaf Propagation Loss for the three FM stations

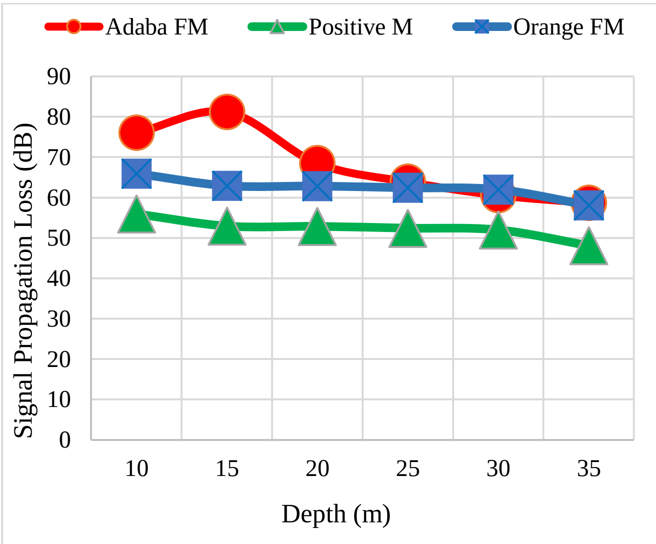

Fig. 9 Out-of-Leaf Propagation Loss for the Three FM Stations

5 Conclusion

Adaba 88.9 MHz, Orange 94.5 MHz, and Positive 102.5 MHz FM Broadcast Station power density (attenuation or signal strength) are observed to decrease along part of their broadcasting area at the Teak (*Tectona grandis*) tree plantation at the Owena River Basin of Ondo, according to the results of field measurements taken and the analysis of the measured signal strengths. but it was primarily influenced by the amount of leaf on the branches of the Teak (*Tectona grandis*) tree plantation, the depth of the teak tree, as well as the altitude and location of the teak tree relative to the three FM radio stations. The newly designed propagation prediction model was discovered to be more appropriate when compared to the two reference prediction models of COST 234 and Weissberger because it gives the least difference in root mean square error of 3.9 dB in the two scenarios, as opposed to COST 234 and Weissberger, which stand at 11.2 dB and 10.8 dB, respectively, and because The newly designed propagation prediction model was more in line with the assessed dataset obtained from the carried out measurement.

6 Recommendations

Distance, transmission power, antenna gain, and terrain are the fundamental factors that determine the effectiveness of radio propagation. It is necessary that radio stations know the terrain of their coverage area to know how to improve the quality of their signal within the primary coverage area in order to meet the recommended level of 60 dB for urban FM broadcasting stations and 48 dB for rural FM broadcasting stations as stipulated in the 5th edition of the Nigerian broadcasting code and be cognizant of the drop in their signal strength during the rainy season, which must be between 3 and 5 dB of the signal strength during the dry season. Therefore, during the planning and designing of radio stations and wireless communication systems that fall within the tropical rainforest area covered by this study, they can predict propagation loss for their service area using the path loss model developed in this study.

References

[1] Zhang, Y., Wen, J., Yang, G., He, Z. and Wang, J., 2019. Path loss prediction based on machine learning: Principle, method, and data expansion. *Applied Sciences, 9*(9), p.1908.

[2] Popoola, J. and Adesanya, A., 2018. A Versatile Wave Propagation Model for Very High-Frequency Broadcasting Band in Vegetation and/or Rocky Environment. *International Journal of Engineering Science and Application, 2*(1), pp.18-26.

[3] Li, L.W., Lee, C.K., Yeo, T.S. and Leong, M.S., 2002. Radio wave propagation along earth-space paths in the presence of a multilayered anisotropic forest. *Electromagnetics, 22*(3), pp.235-260.

[4] Popoola, J.J., Ponnle, A.A., Olasoji, Y.O. and Oyetunji, S.A., 2018. Investigation of the need for a specific propagation model for specific environments based on different terrain characteristics. *IIUM Engineering Journal*, *19*(2), pp.90-104.

[5] Enders, P., 2009. Huygens' principle is a universal model of propagation. *Latin-American Journal of Physics Education, 3*(1), p.4.

[6] Rani, P., Chauhan, V., Kumar, S. and Sharma, D., 2014. A review of wireless propagation models. *International Journal of Engineering and Innovative Technology, 3*(11), pp.256-261.

[7] AS, A., Siddle, D. and Salami, S.O., 2016. Vegetation attenuation and its dependence on foliage density. *European Journal of Engineering and Technology, 4*(3), pp.1-7.

[8] NBC, Nigeria Broadcasting Code. 2002, p.1-196. Available at: http://www.nbc.gov.ng/uploads/nbc_documents/1466685527-code%20third%20edition.pdf, Retrieved July 18, 2023.

[9] Meng, Y.S., Lee, Y.H. and Ng, B.C., 2009. Study of propagation loss prediction in a forest environment. Progress In *Electromagnetics Research B, 17*, pp.117-133.

[10] Seybold, J.S., 2005. Introduction to RF propagation. John Wiley & Sons.

[11] Oke, M. and Raji, R., 2014. Exponential models of signal strength of a television station in Nigeria. *International Journal of Mathematics and Statistics Studies, 2*(1), pp.45-54.

[12] Fagbohun, O.O., Studies on Electric Field Strength Distribution of UHF Television Signal Propagation in Ekiti-State. Nigeria. *International Journal of Electronics and Communications Engineering (IOSR-JECE)*, *9*(2)pp.111-121.

[13] Obot, A., Simeon, O. and Afolayan, J., 2011. Comparative analysis of path loss prediction models for urban macrocellular environments. *Nigerian Journal of Technology, 30*(3), pp.50-59.

[14] Peden, S., Bradbury, R.C., Lamb, D.W. and Hedley, M., 2021. A model for RF loss through vegetation with varying water content. *Journal of Electromagnetic Analysis and Applications*, *13*, pp.41-56.

[15] Cama-Pinto, D., Damas, M., Holgado-Terriza, J.A., Arrabal-Campos, F.M., Gómez-Mula, F., Martínez-Lao, J.A. and Cama-Pinto, A., 2020. Empirical model of radio wave propagation in the presence of vegetation inside greenhouses using regularized regressions. *Sensors, 20*(22), p.6621.

[16] Weissberger, M.A., 1982. An initial critical summary of models for predicting the attenuation of radio waves by trees (pp. 121-123). Department of Defense, Electromagnetic Compatibility Analysis Center.

[17] CCIR, Influences of terrain irregularities and vegetation on troposphere propagation, 235-236 CCIR Report, Geneva, 1986.

[18] Savage, N., Ndzi, D., Seville, A., Vilar, E. and Austin, J., 2003. Radio wave propagation through vegetation: Factors influencing signal attenuation. *Radio Science, 38*(5), pp.9-1.

[19] Stephens, R.B.L. and Al-Nuaimi, M.O., 1998. Measurement and prediction model optimization for signal attenuation in vegetation media at centimeter wave frequencies. *IEE Proc Microw Antennas Propag, 145*, pp.201-206.

[20] COST235, Radio propagation effects on next-generation fixed-service terrestrial telecommunication systems, Final Report, Luxembourg, 1996.

[21] Shaw, J.A., 2013. Radiometry and the Friis transmission equation. *American Journal of Physics, 81*(1), pp.33-37.

SciEn
Journal of Engineering Advancements Vol. 04(03) 2023, pp 64-69 https://doi.org/10.38032/jea.2023.03.002

Forecasting Model Selection with Variables Impact to Predict Electricity Demand at Rajshahi City of Bangladesh

Md. Rasel Sarkar, Rifat Afroz Orpe and Lafifa Margia Orpa*

Department of Industrial & Production Engineering, Rajshahi University of Engineering & Technology, Rajshahi, Bangladesh

Received: May 07, 2023, Revised: August 05, 2023, Accepted: August 05, 2023, Available Online: August 18, 2023

ABSTRACT

The purpose of this study is to forecast electricity demand by using the best-selected method which untangles all the factors that affect electricity demand. Three different methods traditional methods (Multiple Regression Model), modified-traditional methods (ARMA), and soft computing method (Fuzzy Linear Regression Model) are selected for prediction. Environmental parameters like temperature, humidity, and wind speed are included as variables as Rajshahi has very impactful weather. The impact of each variable was calculated from their standardized values to know the effect of environmental parameters. The accuracy of the three forecasting models is compared by different statistical measures of errors. Using Mean Absolute Percentage Error (MAPE), the errors of the Multiple Regression Model, ARMA, and Fuzzy Linear Regression (FLR) Model are 6.85%, 22.24%, and 4.45%. The other three measures of error also give the FLR gives the best results. Finally, the electricity demand of Rajshahi City for the next five years is forecasted using the Fuzzy Linear Regression Model.

Keywords: Forecasting, Soft Computing, Fuzzy Linear Regression, Root Mean Square Error, Correlation Coefficient, Forecasting Error.

1 Introduction

In developing countries like Bangladesh, the electricity problem would create lots of hassles and problems. Rajshahi the fourth biggest city in Bangladesh has a population of over 880,026 residents [16]. Rajshahi is called the "education city" of Bangladesh and it has very impactful weather the weather is very hot during the summer season and very cold during the winter season also humidity is high due to the nearby Padma River. Here electricity demand is high because there are a lot of students in this city and the extreme weather affects the demand during the summer season. Here, Northern Electricity Supply Company (NESCO) calculates the demand manually by predicting values depending on previous data. If the demand can be forecasted by using advanced methods, then the supply calculation would be more accurate. Again, sometimes lack of data on any variable can cause problems in forecasting. If the weights of the variables are known, then data can be collected and used according to priority.

This research aims to forecast electricity demand using the best available tool, which unties all the factors that cause demand changes and pinpoints the root causes. This study is a continuation of various previous studies that analyzed different forecasting methods for calculating load forecasting, now focusing on involving weather variables in forecasting and computing the importance of weather variables, and selecting the best model for electricity demand prediction.

Researchers have used a lot of forecasting techniques from different perspectives. Five artificial intelligence forecasting methods were compared to forecast the monthly flow discharge of the Lancangjiang river [1]. Different forecasting techniques like artificial neural networks, support vector machines, genetic programming, adaptive neural-based fuzzy inference system, and autoregressive moving average are used as the methodological approaches for assessment. Correlation coefficient (R), Nash-Sutcliffe efficiency coefficient (E), root mean square error (RMSE), and mean absolute percentage error (MAPE) were used for the computation of error. Different qualitative and quantitative methods of forecasting, their advantages, disadvantages, and applications were described [2]. Some methods of model selection such as forecast error measures, information criterion, cross-validation, stepwise model selection, and residual diagnostic were pointed out. The classification, advantages, and limitations of different forecasting techniques were discussed [3] Authors have categorized forecasting methodologies into three primary classes, including soft computing forecasting techniques, modified traditional forecasting techniques, and traditional forecasting techniques. Soft computing methods are said to be more effective forecasting methods. One method from each of the three groups for load forecasting is chosen for comparison in this research work. For taking uncertainties into account, an integrated approach to electricity consumption in Iran was described. It included fuzzy linear regression (FLR), time series analysis, and principal component analysis (PCA) [4]. To address the uncertainties of meteorological factors and statistical model inaccuracy in electric load forecasting, fuzzy logic was used in conjunction with the min-max algorithm [5]. Forecasting the load for the city of Dhaka was done to test the performance of fuzzy logic, and the results showed daily forecasting of similar days was extremely accurate. Short-term electrical load forecasting was done for a remote area in Bangladesh where there were no historical data on load demand [6]. For demand forecasting, inverse matrix computation and linear regression analysis were utilized.

To predict Turkey's electricity energy usage, regression analysis, neural networks, and least square support vector machines (LS-SVM) were all compared [7]. The population,

*Corresponding Author Email Address: smdrasel10@gmail.com Published by: SciEn Publishing Group

installed capacity, total subscriber count, and gross electricity generation are all employed as independent variables in these models. By assessing various errors and doing a Receiver Operating Characteristics (ROC) study, LS-SVM prevailed. Using a fuzzy linear regression model, Rajshahi City's electricity demand was predicted by taking into account the number of consumers and temperature [8]. This research also used an autoregression model for forecasting the future values no of consumers and temperature. They worked with one weather variable which is temperature. The importance of wind variables was presented in load forecasting [9]. They used the sample of eight load zone and a total load of ISO New England for forecasting. They included wind variables in a regression analysis framework. The out-of-sample tests proved that variables related to wind velocity improve the models only related to temperature. But this paper has a gap in that it didn't show any complete forecasting model which can forecast the demand by combining the weather variables. A fuzzy logic model is used to forecast short-term (hourly) loads [10]. Using historical load data and the time of day, the method developed a fuzzy rule base to forecast the daily load curve. The future energy consumption of the Indian state of Tamil Nadu was forecast using an artificial neural network (ANN) enhanced by particle swarm optimization (PSO) and genetic algorithms (GA) [11]. The anticipated outcomes from the hybrid ANN-PSO model have been compared to those from the ARIMA, hybrid ANN-GA, ANN-BP, and linear models. A functional vector autoregressive state-space model's historical data on power use was the only source of information used to forecast future electricity demand [12]. The variables that comprise the model were determined using likelihood maximization, spline smoothing, functional principal components analysis, and Kalman filtering.

For a yearlong time frame, the three major Australian states' peak electricity demand was predicted [13]. This research demonstrated how crucial environmental elements are to raising predicting precision. The maximum temperature, minimum temperature, and solar exposure were the weather variables used in this paper's usage of the seasonal autoregressive integrated moving average (SARIMA) model. It had been demonstrated that when factors related to the environment were taken into account, MAPE generally improved by at least 38%. The authors also suggested that other variables like humidity and wind strength, added to the existing ones can give better prediction accuracy. Two more parameters like wind velocity and humidity to increase the accuracy of the models are added in this research work according to the suggestion of this paper. A deep learning-based approach was presented [14] for predicting power usage while considering long-term historical dependence. The study's objective was to investigate the predictive capabilities of models based on functional data analysis, an area of energy research that has received little attention to date [15]. Functional autoregressive (FAR), FAR with exogenous variable (FARX), and traditional univariate AR models are used to simulate and forecast the stochastic component, whereas generalized additive modeling is used to handle the deterministic component. Therefore, long-term (yearly) forecasting is done in our research by calculating the impact of different parameters also comparison among different forecasting methods has been shown.

2 Methodology

Electricity demands depend on a lot of parameters. Researchers have used a lot of techniques and parameters based on their locations. As Rajshahi has impactful weather its parameter was selected carefully. Based on a lot of research papers and expert's opinions we have selected four parameters for our research. Three different methods traditional methods (Multiple Regression Model), modified-traditional methods (ARMA), and soft computing method (Fuzzy Linear Regression Model) are selected for prediction.

2.1 Multiple Linear Regression Model

Multiple linear regression is a model of traditional forecasting methods that permits a statistician to form predictions about one variable using data from another variable. Electricity demand prediction has been done from this model using the parameters considered. The equation for multiple linear regression,

$$Y_i = a_0 + a_1 X_{1i} + a_2 X_{2i} + \dots\dots + a_k X_{kn} \tag{1}$$

where Y_i = i^{th} observation of the output variable, a_j = coefficient of slope for the input variables, X_{ij} = i^{th} observation of the j^{th} input variable.

2.2 ARMA Model

ARMA stands for Auto Regressive Moving Average. This model uses the information obtained from the past data of the variable to forecast its trend which is based on uni variant analysis. For an ARMA model, the formula for forecasting any value (yt) at period t is,

$$y_t = c + \sum_{i=1}^{p} \varphi_i y_{t-i} + \epsilon_t + \sum_{j=1}^{q} \theta_j \epsilon_{t-j} \tag{2}$$

Here, the dependent variable has p lags, and the error term has q lags in this model. y_t and y_{t-i} represent the values in the current period and i period ago respectively.

2.3 Fuzzy Linear Regression Model

Conventional regression model faces some problems when the number of observations is high, or the sample is huge. A normal distribution of error cannot be guaranteed and defining the relationship or vagueness between the dependent and independent variables is difficult. A fuzzy regression model is used to test the functional relationship between input and output variables to solve these problems. In a fuzzy environment, the input or output can be crisp which is converted to fuzzy by the fuzzification process. If the independent variables are denoted by X_1, X_2, X_3, ..., X_n, and the dependent variable is denoted by Y, then the general form of a fuzzy regression model is,

$$Y = A_0 + A_1 X_1 + A_2 X_2 + \cdots + A_n X_n \tag{3}$$

Here, A is a fuzzy number which is a function of middle (p) and spread (c).

In the present study, the probabilistic fuzzy approach is used which tries to reduce the fuzziness of the whole model by minimizing the total spreads of its fuzzy coefficients. The linear programming model to minimize the spread is,

$$Z = minimize \sum_{i=1}^{4}\sum_{j=1}^{13} c_i x_{ij} \quad (4)$$

Subject to,

$$y_j \geq \sum_{i=1}^{4} p_i x_{ij} - (1-h)\sum_{i=1}^{4} c_i x_{ij}$$

$$y_j \leq \sum_{i=1}^{4} p_i x_{ij} + (1-h)\sum_{i=1}^{4} c_i x_{ij}$$

$$p_i \geq 0 \qquad c_i \geq 0$$

where, h is the degree of fit of the estimated fuzzy linear model to the given data, and its value ranging from 0 to 1, will be assumed by the decision maker.

2.4 Forecasting Errors

The accuracy of the three forecasting models is compared by calculating the Mean Absolute Percentage Error (MAPE), Root Mean Square Error (RMSE), Mean Absolute Deviation (MAD), and Normalized Correlation Coefficient (r). Finally, the best forecasting method was selected. And then the electricity demand of Rajshahi City for the next 5 years using the best model was also forecasted.

Mean Absolute Percentage Error (MAPE):

$$MAPE = \sum_{t=1}^{n} \frac{\left|\frac{A_t - F_t}{A_t}\right|}{n} * 100 \quad (5)$$

Mean Absolute Deviation (MAD):

$$MAD = \sum_{t=1}^{n} \frac{|A_t - F_t|}{n} \quad (6)$$

Root Mean Square Error (RMSE):

$$RMSE = \sqrt{\frac{\sum_{t=1}^{n}(A_t - F_t)^2}{n}} \quad (7)$$

Normalized Correlation Coefficient:

$$r = \frac{\sum_{i=1}^{n}(A_t * F_t)}{\sqrt{\sum_{i=1}^{n}\{(F_t)*(F_t)\} * \sum_{i=1}^{n}\{(A_t)*(A_t)\}}} \quad (8)$$

3 Data Analysis

Two major sources were used for collecting the necessary data. Required data was collected from 2001 to 2018 from NESCO (Northern Electricity Supply Company Ltd.), Rajshahi, and Bangladesh Meteorological Department (BMD), Dhaka. The data of Annual numbers of consumers and annual Electricity demand of Rajshahi city were collected from NESCO. The meteorological data, which included averages for temperature, humidity, and wind speed was collected on a yearly basis from BMD.

3.1 Empirical Results for Variable Weights

First, the mean, standard deviation, and standardized values (z) of the annual number of consumers, average temperature, average humidity, and average wind speed were determined. From that, the weight of each variable was calculated using MS Excel solver which is shown in Fig. 1.

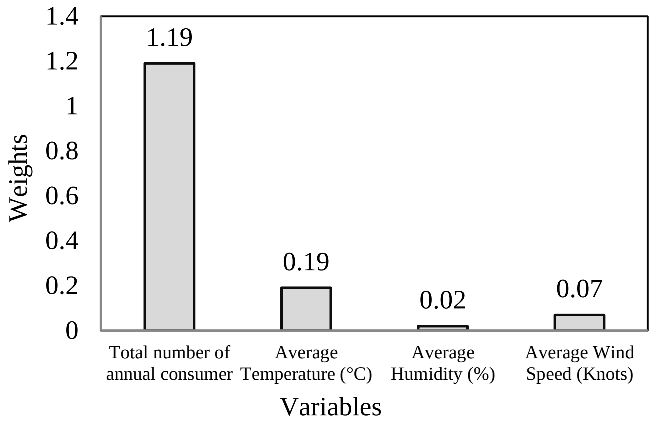

Fig. 1 Weights of the total number of annual consumers, average temperature, average humidity, and average wind speed on electricity demand

Fig. 1 shows that the number of annual consumers has the highest weight of 1.19, so it is the most impactful variable on electricity demand.

3.2 Empirical Results for Multiple Linear Regressions

Using the MS Excel solver function, the intercept and the coefficients of each variable were obtained which are presented in Table 1.

Table 1 Intercept and the coefficients of all variables

Intercept and the variables	Coefficients
Intercept	140.39648
No. of Annual Consumers	0.00044
Average Temperature (°C)	-3.16319
Average Humidity (%)	-0.61482
Average Wind Speed (knots)	0.24850

Then, putting all the coefficients, observed values, and the intercept at the regression equation, forecasted values were obtained. Similarly, electricity demand for 2015 to 2028 is forecasted and the values are presented in Table 2 with the actual electricity demands.

Table 2 Actual electricity demand and forecasted demand

Year	Actual Electricity Demand (MW)	Forecasted Demand (MW)
2014	70	67.78
2015	74	72.74
2016	82	78.39
2017	92	82.85
2018	102	86.68

3.3 Empirical Results for ARMA Model

EViews10 software was used for the identification, estimation, diagnostic, and forecasting of electricity demand by the ARMA model. A correlogram, graph of the model, and unit root test were done. The correlogram and the graph showed no trend. The null hypothesis can be disproved because the p-value is less than 0.05. Thus, the model used for this case study can be described as stationary. Moving average 1 is determined by the autocorrelation function, and autoregression 1 is determined by the partial autocorrelation function. As a result, the ARMA (1,1) model is used in this case study.

The residual diagnostic was carried out after estimating an expression for the ARMA (1,1) model. Because the p-value is higher than 0.05, the null hypothesis cannot be disproved. The residuals are hence white noise. Both the AR and MA roots are located inside the unit circle, which guarantees that the process is invertible and conforms to the covariance stationary condition. So long as the model met all requirements, predicting was feasible.

The electricity demand from 2014 to 2018 in Rajshahi City was forecasted using the forecast function of EViews. The forecasted values and the actual values are given in Table 3.

Table 3 Actual electricity demand and forecasted demand by ARMA Model

Year	Actual Electricity Demand (MW)	Forecasted Demand (MW)
2014	70	65.15
2015	74	64.54
2016	82	63.95
2018	92	63.39
2019	102	62.86

3.4 Empirical Results for Fuzzy Linear Regression

A LINGO code was generated to solve the fuzzy linear programming model and determine the fuzzy parameters. The fuzzy parameter values are obtained in Table 4.

Table 4 Fuzzy parameters obtained from LINGO code

Fuzzy Parameters	Obtained Values	Fuzzy Parameters	Obtained Values
P0	2.78522	C1	2.4404E-05
P1	0.00045	C2	0
P2	0	C3	0
P3	0	C4	0
P4	3.21209	H	0
C0	0		

The values of fuzzy parameters were put into the fuzzy regression functions to determine the upper bound and lower bound of the forecasted electricity demand values. The central value of these two bounds was taken as the forecasted value given in Table 5.

Table 5 Actual electricity demand and forecasted demand by FLR model

Year	Actual Electricity Demand (MW)	Forecasted Lower bound (MW)	Forecasted Upper bound (MW)	Forecasted Central Value (MW)
2014	70	69.09	75.77	72.43
2015	74	73.69	80.84	77.27
2016	82	79.43	87.22	83.33
2018	92	84.12	92.44	88.28
2019	102	88.70	97.61	93.16

The value of forecasted electricity demand by different models along with the actual value is presented in Fig. 3. It is seen that the ARMA model is most deviated from the actual demand line. Deviations of fuzzy linear regression are the least.

3.5 Empirical Results for MAPE, RMSE, r-value, MAD

The outcomes are displayed in Table 6 below. According to experimental findings, the fuzzy linear regression model's MAPE is the lowest of all, at 4.45%. When compared to the autoregressive moving average model, the MAPE for multiple linear regression is similarly incredibly low. The fuzzy linear regression model's RMSE, which is the lowest of all, is 4.6967.

Table 6 MAPE for different forecasting techniques

Forecasting Techniques	MAPE (%)	RMSE	r value	MAD
Multiple Linear Regression	6.85	8.2216	0.9984	6.312
Autoregressive-moving average	22.24	23.6190	0.8111	20.022
Fuzzy Linear Regression	4.45	4.6979	0.9986	3.918

The ARMA model shows the maximum error. In calculation, the Normalized correlation coefficient (r-value) for the FLR model is 0.9986 which is the largest among all. This is more accurate as the r value measures the closeness from the actual value. The r value of MLR indicates that this model is also close to the actual value. The Mean Absolute Deviation (MAD) value for FLR is lower than other methods. The FLR model has the lowest MAD value 3.918 which means the deviation from the actual value of this model is less. The results are compared graphically in Fig. 2.

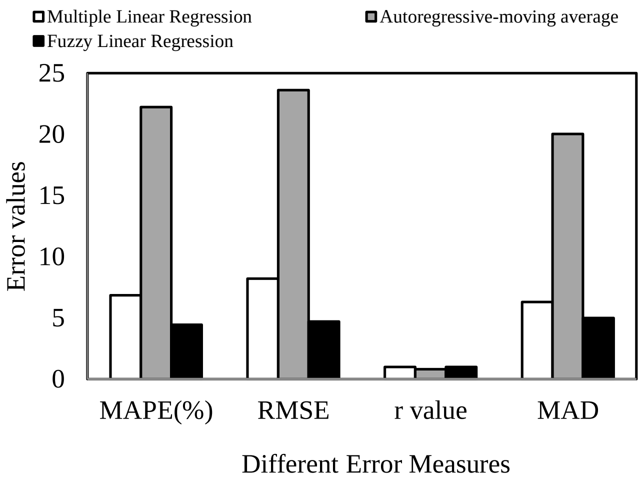

Fig. 2 Error comparison for different forecasting techniques

3.6 Forecast by Fuzzy Linear Regression Model

From Fig. 3 it is obvious that the FLR method's results are the most accurate. The fuzzy linear regression model was also utilized to anticipate Rajshahi's electricity demand for the ensuing five years (2019 to 2023), as it had the lowest error of all the techniques covered in this study.

The values of the four variables from 2019 to 2023 were forecasted using the Autoregression method. These data and values of fuzzy parameters were used in the fuzzy regression equation to obtain the forecasted value. Table 7 gives the predicted electricity demand for the next five years using the fuzzy linear regression model. It is seen that electricity demand will increase gradually in the next five years.

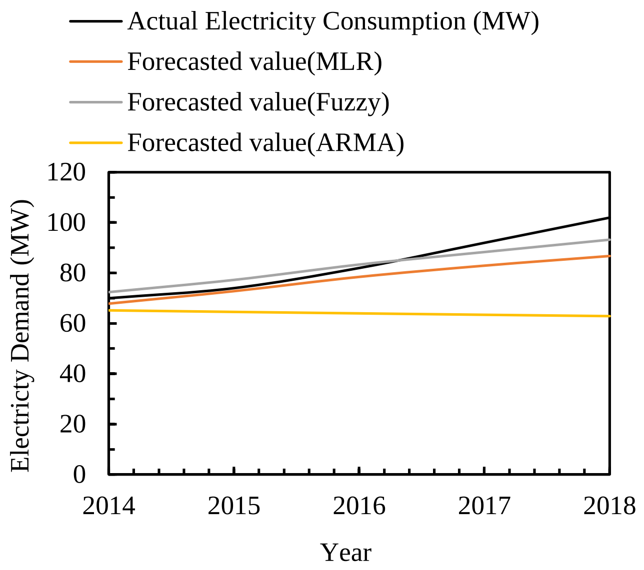

Fig. 3 Forecasted values comparison by different methods

Table 7 The forecasted electricity demand of Rajshahi City from 2019 to 2023

Year	Lower bound (MW)	Upper bound (MW)	Central Value (MW)
2019	94.45	104.01	99.23
2020	100.62	110.88	105.75
2021	107.27	118.29	112.78
2022	114.39	126.21	120.30
2023	122.03	134.72	128.38

The fuzzy linear regression model gives two peak demands – the lowest and highest demands. Central values are calculated from them. Fig. 4 provides a graphical illustration of the central values (forecasted demand) of the fuzzy regression model.

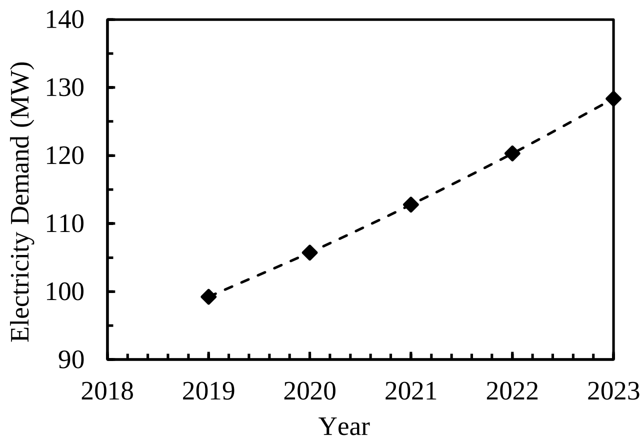

Fig. 4 Forecasting electricity demand for the next five years in Rajshahi City

4 Discussion

The results show some difference between predicted demand and actual demand. This may be due to possible slight data inaccuracies brought on by human data entry, and inherent errors in forecasting models. Only a few previous years' data have been considered, a large database will give greater accuracy. Since the fuzzy linear regression model gives the lowest MAPE, RMSE, and MAD values as well as the highest r value, it was determined to be the best model for predicting electricity demand in Rajshahi. The ARMA model has the biggest forecasting oversights. High errors could happen because of this model's lack of consideration for the variables. The other two models, however, account for the considerations. Consequently, it is true that weather factors play a crucial role in forecasting accuracy.

The first conclusion from this study is that weather factors have a significant influence on projecting electricity demand. The average temperature is also given the most weight among the meteorological factors. Along with the overall number of customers, the mean humidity and average wind speed should also be considered for more precise load forecasting.

Second, accurate forecasting outcomes from comparing various forecasting models from various categories. Different forecasting models have been evaluated using errors. It assessed the forecasting models' accuracy.

5 Conclusions

This study's goal was to explain Rajshahi's electricity demand and how factors affect electricity demand. First, the variable weights were determined. The number of customers, which is given a weight of 1.19, is the variable that affects energy usage the most severely. Next, with rankings of 0.19, 0.07, and 0.02 for average temperature, wind speed, and humidity, respectively. As a result, while average humidity is less relevant, it has a minor impact on projecting electricity demand.

Then, multiple linear regression, autoregressive moving averages, and fuzzy linear regression models were used to forecast the data from previous years. Then, four distinct types of errors were measured to compare the predicted data with the actual data. The fuzzy linear regression model lowered inaccuracy, according to experimental results. The fuzzy linear regression model has the lowest MAPE and MAD values, respectively, at 4.45% and 3.92, respectively. Fuzzy linear regression has a higher normalized correlation coefficient (0.9986) than other normalized correlation coefficients. The fuzzy linear regression model's RMSE is 4.6979. Therefore, among all forecasting models, the fuzzy linear regression model was chosen as the most efficient one.

Using the fuzzy linear regression model electricity demands have been forecasted for the next five years (2019 to 2023). Values of the four parameters from 2019 to 2023 have been forecasted using the Autoregression method. These data and values of fuzzy parameters have been used in the fuzzy regression equation to obtain the forecasted value. And from the fuzzy linear regression model, it is obtained that the electricity demand will increase gradually in the next five years. In the future, to forecast more accurately and especially with weather variables, one may apply a fuzzy linear regression model. Also including more variables will lead to the result being more accurate.

References

[1] Wang, W.C., Chau, K.W., Cheng, C.T. and Qiu, L., 2009. A comparison of performance of several artificial intelligence methods for forecasting monthly discharge time series. *Journal of Hydrology*, *374*(3-4), pp.294-306.

[2] Wang, S. and Chaovalitwongse, W.A., 2011. Evaluating and comparing forecasting models. *International Journal of Forecasting*, *14*(1), pp.35-62.

[3] Singh, A.K., Khatoon, S., Muazzam, M. and Chaturvedi, D.K., 2012, December. Load forecasting techniques and methodologies: A review. In *2012 2nd International Conference on Power, Control and Embedded Systems* (pp. 1-10). IEEE.

[4] Azadeh, A., Saberi, M. and Gitiforouz, A., 2013. An integrated fuzzy mathematical model and principal component analysis algorithm for forecasting uncertain trends of electricity consumption. *Quality & quantity*, *47*, pp.2163-2176.

[5] Monne, M.A. and Alam, K.S., 2013. Application of fuzzy logic to electric load forecasting (ELF). *Int. Journal of Science and Advanced Technology*, *3*, pp.47-50.

[6] Islam, A., Hasib, S.R. and Islam, M.S., 2013. Short term electricity demand forecasting for an isolated area using two different approaches. *Journal of Power Technologies*, *93*(4), pp.185-193.

[7] Kaytez, F., Taplamacioglu, M.C., Cam, E. and Hardalac, F., 2015. Forecasting electricity consumption: A comparison of regression analysis, neural networks and least squares support vector machines. *International Journal of Electrical Power & Energy Systems*, *67*, pp.431-438.

[8] Sarkar, M.R., Rabbani, M.G., Khan, A.R. and Hossain, M.M., 2015, May. Electricity demand forecasting of Rajshahi City in Bangladesh using fuzzy linear regression model. In *2015 International Conference on Electrical Engineering and Information Communication Technology (ICEEICT)* (pp. 1-3). IEEE.

[9] Xie, J. and Hong, T., 2017. Wind speed for load forecasting models. *Sustainability*, *9*(5), p.795.

[10] P. Ganguly, A. Kalam, and A. Zayegh, “Short term load forecasting,” in *International Conference on Research in Education and Science (ICRES)*, 2017, pp.355–361.

[11] Anand, A. and Suganthi, L., 2020. Forecasting of electricity demand by hybrid ANN-PSO models. In *Deep learning and neural networks: Concepts, methodologies, tools, and applications* (pp. 865-882). IGI Global.

[12] Nagbe, K., Cugliari, J. and Jacques, J., 2018. Short-term electricity demand forecasting using a functional state space model. *Energies*, *11*(5), p.1120.

[13] Eshragh, A., Ganim, B., Perkins, T. and Bandara, K., 2022. The importance of environmental factors in forecasting australian power demand. *Environmental Modeling & Assessment*, *27*(1), pp.1-11.

[14] Bedi, J. and Toshniwal, D., 2019. Deep learning framework to forecast electricity demand. *Applied energy*, *238*, pp.1312-1326.

[15] Shah, I., Jan, F. and Ali, S., 2022. Functional data approach for short-term electricity demand forecasting. *Mathematical Problems in Engineering*, *2022*.

[16] Rajshahi Population 2023, Available at: https://worldpopulationreview.com/world-cities/rajshahi-population. Date of Access: 10th April 2023.

SciEn
Journal of Engineering Advancements Vol. 04(03) 2023, pp 70-79 https://doi.org/10.38032/jea.2023.03.003

Automated Object Sorting System with Real-Time Image Processing and Robotic Gripper Mechanism Control

*Safqut Sanwar** and Md. Imteaz Ahmed*

Department of Mechanical Engineering, Chittagong University of Engineering & Technology, Chittagong, Bangladesh

Received: June 09, 2023, Revised: July 05, 2023, Accepted: August 05, 2023, Available Online: September 04, 2023

ABSTRACT

This work represents an industrial sorting system where image processing is accompanied using a pick-and-place robotic gripper. The sorting of objects is done based on their shape and color. Here the color and shape of different objects are identified using image processing. For this, a webcam is used to capture images of the object in real time and then process them via a digital computer. Python programming language is used for image processing in this work. After successfully identifying the color and shape of an object, the object is picked and placed at the desired position using the robotic gripper. Controlling the gripper mechanism is also executed using the Python programming language. It is controlled using the Arduino Uno microcontroller and a few DC servo motors. The gripper can move from 0° to 180°. The objects are brought in front of the camera using a belt conveyor system. After the complete fabrication and assembly, 4 objects of different shapes and colors are used to sort objects at 4 different angles. The objects are picked from 90° and is sorted in either 0°, 45°, 135°, or 180° position. This research work not only gives information about robotics but also can help industries sort complex objects automatically without any human interaction.

Keywords: Image Processing, Arduino UNO, Micro-controller, Object Sorting, Robotic Gripper, Python.

1 Introduction

Using a digital computer and algorithms to process a digital image is known as digital image processing. It is more advantageous than analog image processing because a wider range of algorithms can be applied here. From pattern recognition to feature extraction, many tasks can be done using digital image processing [1]. Image processing is used to not only identify the color but also the shape of the objects in an image. In the modern world, robotics, and automation are making production processes faster and easier and saving both the cost and time of production. Industries around the world are using automation for manufacturing, packaging, and many other applications. Object-sorting robotic arms are a major part of industries. There are thousands of production plants in the world where object sorting is necessary and a vital part of the production process. Sorting objects based on different parameters (i.e., shape and color) is a very important task in the production process [2]. Object sorting robots that operate with the help of image processing can save labor costs as well as increase efficiency in modern-day production. But for this, the program has to be trained more and more so that more complex objects can be sorted easily. This research work is about sorting objects based on shape and color by merging two major tasks together which are the recognition of objects using image processing and sorting objects using a robotic gripper [3].

Image is the best way to perceive one's surroundings. Just like human beings, computer vision, and image analysis can help a machine to understand an image by perceiving it electronically. Image processing is done mainly for two reasons: Analyzing the image to give certain information to the operator (Human). For example, using images from a CCTV camera to identify the face, attributes, etc. of a person. Analyzing the image and then saving and using the information to control or operate another machine automatically. For example, satellites take images in space in a different RGB combination and then the image processing programs convert them to make them understandable [1]. The whole image processing system consists of a few different components such as a sensor (camera), digital computer, display, storage, etc. Image processing uses thousands of images of the same object to make the machine learn and understand the shape, size, and functions of an object. That is why large storage is a very important factor here. A good video camera can help to capture better images and then the computer will process the image using certain algorithms and machine codes. The display is for viewing the acquired images for processing and for viewing the results after processing [4]. The image processing system performs certain operations on an image. These can be simultaneous or individual. The operations are,

Enhancement: Image processing can enhance an image by changing the color grading of the image. An image with low pixels can be enhanced by increasing the pixels using image processing.

Transformation: An image can be transformed into different data by using image processing. Every color has a different hue, saturation, and brightness values which can be separated using image processing.

Compression: If necessary, an image can be easily compressed by using image processing. This is just the opposite of enhancing where the pixels and colors are changed or reduced to reduce the size of the image.

Restoration: An image is nothing but a set of data. If data is lost it can be restored. So, image processing can help to restore lost data. An image is made of thousands of small pixels and image processing can be used to correct these pixels for restoration.

Description: As mentioned above, an image is nothing but a set of data. There are some numerical values in an image,

*Corresponding Author Email Address: u1603050@student.cuet.ac.bd

these values can be hue, saturation, brightness, or any other values. Image processing helps to describe different objects based on these values.

Segmentation: An image can be divided into a few segments so that each segment can be used for one particular task. Image processing divides images into necessary segments to separate different areas of an image and this makes it easier for the program to process the segmented part rather than collecting the whole image.

Interpretation: Image processing helps to explain an image based on different numerical values, data, colors, and many other aspects. The action of explaining a particular parameter using image processing is called interpretation in this case.

Recognition: Image processing can be used to recognize anything present in an image. It can be a person or an object. Whichever it is, the shape, color, size, attribute everything can be recognized using image processing.

These operations help both humans and other machines to find out the details in an image and then use that for different applications [1].

The sorting of the objects based on shape and color is done using a robotic gripper. An industrial robotic arm was first introduced in 1961 by a company named Unimate. It was eventually developed into the PUMA (Programmable Universal Machine for Assembly) arm. Nowadays industries are relying more and more on robotic arms for assembling, sorting, delivering, and other purposes [5]. There are various types of robotic arms, and they all have different applications. For example,

Gantry Robotic Arm – This type of arm uses a Cartesian coordinate system to move and so it is also known as a Cartesian Robotic Arm. The Gantry Robotic Arm is used to perform assembly operations, arc welding, handling machine tools, etc.

Cylindrical Robotic Arm – The axes of this type of robot are from a cylindrical coordinate system. It is mostly used for spot welding and die-casting operations.

SCARA Robotic Arm – Two parallel joints have rotary motion in this type of robot. This motion provides plane compliance. The SCARA robotic arms are used to pick and place objects.

Cobot Robotic Arm – The rounded edges and the lightweight construction of these robots make them safe for industrial applications. The Cobot Arms are usually isolated from contact with humans.

Polar Robotic Arm – Instead of using a cylindrical or Cartesian coordinate system, these robotic arms use a polar coordinate system. These are suitable for gas welding, fettling machines, etc.

Articulated Robotic Arm – A robotic arm with a minimum of three rotary joints is known as Articulated Robotic Arms. Spray painting, welding, diecasting, etc. are some of the main functions of these robotic arms [6].

Robotic arms are often described by their degrees of freedom or DoF in short. DoF defines the state of an object or machine by its independent parameters. There are many types of DoF for robotic arms (i.e., 4-DoF, 6-DoF, etc.). However, this research work will use a robotic arm of 4-DoF with a simple gripper mechanism to pick up an object and place it. The goal is to see how efficiently it can place an object after its image is processed by the computer using certain algorithms [7].

2 Literature Review

Previously many works have been done on automatic object sorting using image processing, sensors, processors, robotic arms, etc. In those works, objects of different colors or shapes or other parameters were detected and then the objects were sorted based on those parameters. Some of the highlighted works are mentioned below.

Joy [8] made an object separating a robotic arm based on the color of the object. An ARM7-2138 microcontroller was used to control the arm, and the object was of three different colors. The color detection was done using the light intensity to frequency converter method. Moreover, the robotic arm was controlled using DC servo motors. For light-to-frequency conversion, the TCS3200 programmable convert was used. Nicolaus et al. [9] used a 6-DoF robotic arm to sort objects based on color as well. Here they used two cameras one of which was used to search for objects while the other one was sending digital feedback to the computer and robotic arm. They used MATLAB for programming the codes for image processing and the robotic arm. Jia et al. [10] used image processing to detect the color of the objects and then used the Phantom X Reactor robotic arm to pick and place the object. The arm was controlled using the ArbotiX-M microcontroller. They used OpenCV rather than MATLAB as it is more convenient. Also, they used the C++ programming language to write the codes for image processing and controlling the robot. Shah and Pandey [11] made an automatic sorting robotic arm at low cost using an Arduino UNO3 microcontroller; VGA camera; barcode and QR code scanner; Tactile, RGB, and color sensors. But they didn't use any image processing here. It was a simple low-cost automatic robotic arm system that could detect obstacles and objects through the sensors and then sort them according to the given commands. Sampreeth et al. [12] used image processing and controlling a robotic arm to sort objects based on shape and color. However, they used the ARM7 microcontroller for controlling the robotic arm. Moreover, they used coding on MATLAB for image processing and microcontroller commands. Kale and Kulkarni [13] proposed an object-sorting system using a robotic arm. The proposal was to use a microcontroller to control the arm and a camera to capture the moving object's color and shape. The object would move on a conveyor belt and the belt would be controlled with a motor drive. For image processing they used MATLAB, and they used the ATmega328 CMOS 8-bit microcontroller. Amin et al. [14] created a mechanism to detect and distinguish the color of an object and then place it in a designated position. They used a robotic arm for the pick and place mechanism, but they did not use any image processing. Instead, they used the TCS 3200 color sensor to detect the color of the object. The robotic arm was controlled using a PIC microcontroller (18F452). The robotic arm could rotate up to 360° angle. Mohammed et al. [15] also used a color sensor (TCS230) and a PIC 16F628A microcontroller to sort objects based on color. A conveyor belt was used to move the objects and the color sensor was placed above the objects that could sense the color and then transfer the object to a predetermined position. Another conveyor belt was used to hold the different boxes where the objects would drop according to color. There was no robotic arm used in this research work. Also, the objects were sorted only based on the colors. Bhaskar et al. [16] made a sorting system based on color using a robotic arm. They used the SSC-32 servo control board to control the robotic arm. They used a webcam to capture the images of the objects and then identify their colors. For color detection, they used an application called Lab Windows/CVI from national instruments. After identifying the color, the computer sent a signal to the robotic arm and the arm placed the objects based on the color. Deshmukh et al. [17] used the PIC 16F877A microcontroller to control a conveyor belt system for sorting objects based on color. Did not use any camera, but the TSOP 1738 color sensor, which detected the colors of the different objects and then the conveyor belt sorted the objects according to their color. A robotic arm was also not used in this case. This research work also did not use the shape of the objects for sorting. Shirgave et al. [18] used an Arduino UNO controller, servo motors, and the TCS3200 color sensor to build a color-sorting robot. The robot was not a moving robot that could rotate its arm at a certain angle to place an object based on color. It was an efficient robot but it could not sort the object based on any other criteria except for the color of the object. Suryawanshi et al. [19] made a robotic arm using the Arduino microcontroller for sorting objects based on color. However, they did not use any camera to capture images of the object for color detection. They used the TCS34725 color sensor to detect the color of the objects. To make the robotic arm move they used DC servo motors, and the motors were driven using the L293D motor driver. Patel et al. [20] made an object-sorting machine based on IOT and color. They used the Arduino UNO microcontroller to control a robotic arm for picking and placing the object. For color detection, they used the TSC3200 color sensor. They also use a GSM module in their research. However, their goal was to sort objects based only on color. Jakkan et al. [21] Used both Arduino UNO and ATmega328 microcontrollers to control a robotic arm that was able to pick and place objects based on their colors. The colors of the objects were identified using the TCS3200 color sensor instead of image processing. They also used a Wi-Fi module (ESP8266) and a mobile device in the research. But they did not show the objects based on any other criteria. Patil et al. [22] reviewed a paper where they introduced a model that could sort objects based on color. They used C++ programming language to create codes for an Arduino microcontroller to control a conveyor belt. The conveyor belt sorted objects based on colors and if the color was not specified by the color sensor, the object went to a separate box. They did not use any robotic arm to sort the objects in this case. Sireesha et al. [23] created an automatic object sorting system that was able to sort waste objects based on thickness and color. They created a system without any robotic arm, but an Arduino microcontroller was used to move a part of the system to a certain angle to place the object. Instead of using an image processing system they simply used a color sensor (TCS3200) which could identify only a certain number of colors. Ghosh et al. [24] made a product-organizing tool based on color. They also used an Arduino UNO microcontroller and TCS3200 and TCS230 color sensors to identify the colors of the objects placed in the system and control the servo motors to control the parts of the objects to a certain position. However, they did not use any image processing or robotic arm for this. Also, the objects were supported only based on color and no other features. Simran et al. [25] developed a system for automatically sorting objects using a conveyor belt. The objects were identified using a photoelectric sensor (beam-type) in this research. The different identified objects were then placed in different positions using the conveyor belt. A programmable logic controller (PLC) helped to control the conveyor belt. The programming was done using the MicroWIN software. This research did not use any method to identify the shape of the object. Shen and Hassan [26] created a robot that could sort objects based on their colors. The robot was controlled using an Arduino UNO microcontroller. They used the TCS3200D color sensor to identify the colors of the objects. After identifying the color, the robot could place the objects into their designated color station in a short time. However, the robot could not sort the objects based on their shapes. Zulfiqar et al. [27] used a programmable logic controller to control a conveyor belt for sorting objects based on their material type. To identify the material, they used a proximity sensor. It detected wood, metal, and plastic and then placed the objects in the required positions. However their system could not detect the objects based on their color. Also, they only used censors, and there was no use of any image processing system. Jahan et al. [28] made an object-sorting machine based on color. They used the Arduino microcontroller to control a belt conveyor system to sort the objects. For color detection, they used the TSC 34725 RGB color sensor. They also included a feature where white objects would make the belt system move backward. However, their goal was to sort objects based only on color.

Most of the previous studies either sorted the robot based on shape or color except for Sampreeth et al. [12]. However, some of the research didn’t even use image processing. Also, one of the types of research used two cameras which is less convenient than using a single camera. Only a few of the research used OpenCV and Python coding, which is more efficient than coding on MATLAB. Finally, the ARM7 microcontroller used in most of the previous research is more complex than Arduino. This research work utilized Python programming language for coding the image processing work, and for giving a command to the microcontroller of the robotic arm. At first, the whole system is designed using SOLIDWORKS. Then each of the parts is fabricated and then parts are assembled to merge the whole system. Instead of the ARM7 microcontroller, Arduino is used which is simpler and less costly. Also, the objects are not sorted only based on the color or the shape but on both parameters. From all the previous studies a conclusion came to that image processing can be a better and more efficient way to identify an object’s shape and color than using any sensor. This is why the goal of this research is to utilize the benefits of image processing and merge it with robotics to create an automatic object-sorting system that will eventually help a lot of industries.

Table 1 Comparative View of the Previous Studies

Author(s)	Summary	Parameter	Detection Process	Sorting Process	Limitations
Joy [8]	Object sorting robotic arm based on color	Color	Light to frequency converter	Robotic arm	Only color detection
Nicolaus et al. [9]	Development of an autonomous ball picking robot	Color	Image processing	Robotic arm	Only color detection
Jia et al. [10]	Real-time color-based sorting	Color	Image processing	Robotic arm	Only color detection
Shah and Pandey [11]	Concept for Automated Sorting Robotic Arm	Undefined	Tactile Sensor	Robotic arm	No particular parameter
Sampreeth et al. [12]	Object sorting robot using image processing	Color and Edge	Image Processing	Robotic arm	No particular shape detection
Kale and Kulkarni [13]	Object sorting system using robotic arm	Color and Shape	Image Processing	Robotic arm	Proposal only
Amin et al. [14]	Detection and distinction of colors using color sorting robot	Color	RGB color sensor	Robotic arm	Only color detection
Kunhimohammed et al. [15]	Automatic color sorting machine using color sensor	Color	TCS230 Color Sensor	Belt conveyor	Only color detection
Bhaskar et al. [16]	Colour sorting system with robotic arm	Color	Image processing	Robotic arm	Only color detection
Deshmukh et al. [17]	Automatic conveyor color sorting	Color	Color sensor	Belt conveyor	Only color detection
Shirgave et al. [18]	Color sorting robot	Color	TCS3200 color sensor	Slot moving mechanism	Only color detection
Suryawanshi et al. [19]	Color sorting robotic arm	Color	TCS34725FN color sensor	Robotic arm	Only color detection
Patel et al. [20]	IOT color-based object sorting machine	Color	TCS3200 color sensor	Robotic arm	Only color detection
Jakkan et al. [21]	Color based product sorting machine	Color	TCS3200 color sensor	Robotic arm	Only color detection
Patil et al. [22]	Review on colored object sorting system	Color	TCS3200 color sensor	Belt conveyor	Only color detection
Sireesha et al. [23]	Automated sorting system based on color and thickness	Color and Thickness	TCS3200 color sensor and ultrasonic sensor	Slot moving mechanism	No particular shape detection
Ghosh et al. [24]	Color-based product organization tool	Color	TCS3200 color sensor	Slot moving mechanism	Only color detection
Simran et al. [25]	Development of automatic sorting belt conveyor	Height	Photoelectric sensor	Belt conveyor	Only height detection
Shen and Hassan [26]	Design and development of color sorting robot	Color	TCS3200 color sensor	Driving robot	Only color detection
Zulfiqar et al. [27]	PLC Based Automated Object Sorting System	Material	Proximity sensors	Belt conveyor	Only material type detection
Nuva et al. [28]	Color and weight-based sorting system on belt conveyor	Color and Weight	TCS 34725 RGB color sensor and load cell	Belt conveyor	No particular shape detection

3 Methodology

This research work is about sorting objects based on their shape and color using image processing. Here a webcam is used to scan the image of objects of different shapes and colors. After scanning the image, the results are sent to the Arduino microprocessor that controls the robotic arm. The robotic arm then picks up the object and places it in the desired place. For example, if the object has a blue color rectangular shape, it is placed in a position. If it has a red color and rectangular shape, it is placed in a different position. Similarly, if it has a blue color and circular shape, it is placed in a third different position, and so on. The objects pass by the camera with the help of a belt conveyor. The camera is placed on one side of the conveyor. The robotic arm is on the end part of the belt conveyor. As soon as the object comes in front of the camera, it captures the image, and the computer identifies it using image processing and then sends a signal to the arm through the Arduino microcontroller for picking and sorting.

3.1 Fabrication and Assembly

Designing a part, component, or setup is one thing, but fabrication is totally different. In this research work, SOLIDWORKS was used to design the main component or the setup of the research. However, these components were fabricated after the design to make the vision of the setup a reality. This chapter describes the fabrication and assembly process of the whole setup.

This research contains a few major components and each of the components was designed, and the models were used to fabricate them. After that, those components were assembled.

1) Fabrication of the Robotic Gripper: The robotic gripper was designed using SOLIDWORKS and it was a typical model of the arm. After designing the arm, it was time to make a list of the components that were needed to fabricate the arm. The components or parts used to fabricate the arm were bolts, nuts, servo motors, 3D-printed arm parts, and wires. At first, the individual parts of the arm were 3D printed. Then the parts were connected to each other using bolts and nuts so that the parts could move but stay connected to each other. Then 4 servo motors were connected to the parts. The function of the motors is as follows. 1 is used to control the base. 1 is used to control the gripper. The other 2 motors on the left and the right side are used to make the gripper move forward-backward and up-down. All the servo motors are connected to wires. There are 3 wires of a servo motor, brown, red, and yellow. The red wire is connected to the voltage source, the yellow wire is connected to the PWM (pulse width modulation) pins of Arduino Uno, and the brown wire is for ground connection. Fig. 1 shows the robotic (arm) after it is fabricated.

Fig. 1 The fabricated robotic gripper

The robotic gripper has a total of 4 degrees of freedom (DOF). Here's an explanation of the DOF for the robotic gripper:

Base Rotation (1 DOF): The gripper arm has a servo motor mounted at the base, which allows it to rotate. This rotational movement provides the arm with the ability to change its orientation within a 180° range. This DOF enables the arm to cover a wide area without physically moving its position.

Arm Forward and Backward Movement (2 DOF): Two servo motors are employed to control the main body of the arm. These motors enable the arm to move forward and backward, extending or retracting the arm's length from its base. This movement provides the gripper with the ability to reach objects at different distances, extending its operational range.

Claw Up and Down Movement (1 DOF): One servo motor is dedicated to controlling the movement of the claw mechanism. This motor allows the claw to move up and down, enabling it to grip objects of varying heights. This DOF is crucial for the gripper to adapt to objects with different vertical positions.

By combining the 1 DOF for base rotation, the 2 DOF for arm movement, and the 1 DOF for claw movement, we have a total of 4 DOF for the robotic gripper. These degrees of freedom provide the gripper with the necessary flexibility and range of motion to perform object-sorting tasks effectively.

2) Fabrication of Detecting Object Shape and Color: The camera or webcam that is used to capture the images for shape and color detection is Fifine K420. This is connected to the computer using the USB port and it captures and sends data to the computer for image processing. In this research work, the object’s shape, and color both are detected using a single camera. An algorithm in Python had to be developed to detect both at the same time. The working mechanism of the algorithm is very simple. At first, the code runs and detects the color of the object. As soon as it detects the color, it then operates to detect the shape of the object. The simple “if” and “elif” statements are used to guide the code to pick the color and then the shape. The color is converted from RGB (Red, Green, Blue) value to HSV (Hue, Saturation, Value) so that they can be captured through the HSV values of the object. This is more precise as different colors have different saturation levels. However, after detecting the color, the code detects the shape of the object. For this, another set of codes is run. Here the higher and lower HSV are set using the trackbar that is also generated when the code runs. This is how the camera is used to detect the color and shape of the object. Here are some key points on image processing or OpenCV used in this work:

Image Acquisition: OpenCV's VideoCapture function is utilized to acquire video frames from a specified video source (in this case, the default camera, identified as index 0). The acquired frames serve as the input for subsequent image-processing operations.

Color Space Conversion: The cv2.cvtColor function from OpenCV is employed to convert the acquired frames from the default BGR color space to the HSV color space. This conversion enables better color-based object detection and analysis.

Thresholding: Within the HSV color space, OpenCV's cv2.inRange function is used to perform thresholding. This function creates a binary mask by selecting pixels within a specific range of hue, saturation, and value (HSV) values. Thresholding helps isolate objects of interest based on their color characteristics.

Contour Detection: OpenCV's cv2.findContours function is employed to detect contours within the binary mask obtained through thresholding. Contours are important for shape analysis and identification of objects within an image. The cv2.RETR_TREE and cv2.CHAIN_APPROX_SIMPLE arguments specify the contour retrieval mode and approximation method, respectively.

Shape Approximation: The cv2.approxPolyDP function from OpenCV is utilized to approximate the contours and simplify their representation. This function uses the Ramer-Douglas-Peucker algorithm to reduce the number of points in a contour while preserving its overall shape.

Object Recognition and Classification: Based on the number of sides in the approximated contour, the objects are classified as either rectangles or circles. This classification enables the identification of different shapes based on their contour characteristics.

3) Fabrication of the Belt Conveyor: The belt conveyor was designed using SOLIDWORKS and it was a typical model of the conveyor system. After designing the belt conveyor, it was time to make a list of the components that were needed to fabricate the system. The components or parts used to fabricate the belt conveyor were ball bearing, conveyor belt, roller pipes, DC motor, bolts and nuts, switches, AC power adapter, and aluminum frame. At first, the roller pipes were attached to the bearings and one roller pipe was connected to the DC motor. Then the belt was mounted over the rollers tightly to achieve enough friction that would move the belt when the rollers rotated. Then the rollers were mounted on the aluminum frame using nuts and bolts. The DC motor can be controlled forward and reverse using a switch. The switches were connected to the AC power adapter so that the voltage level of the motor could be limited. Fig. 2 shows the belt conveyor after it is fabricated.

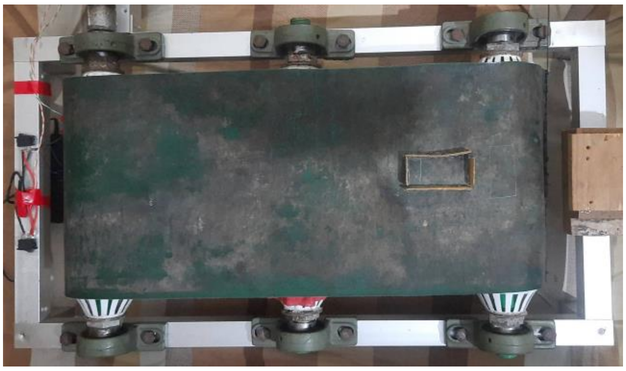

Fig. 2 The fabricated belt conveyor

4) Complete Assembly of the Work: After fabricating all the major components, the complete system was assembled. The robotic gripper was attached to one end of the belt conveyor frame. The servo motors of the robotic gripper were then connected to the Arduino Uno microcontroller. A breadboard was used to distribute the ground and power connection. The microcontroller was connected to the digital computer using a USB cable. Another USB port of the computer was used to connect the webcam to the system. The webcam was placed on one side of the belt conveyor. An AC power adapter was used to supply power to the DC motor of the belt conveyor. The motor and the adapter were connected by 2 switches one of which made the system rotate forward and the other one made it rotate backward. Below is Fig. 3 which shows the fabrication of the complete assembly.

Fig. 3 The actual setup of the system

5) Circuit Design and Diagram of the System:
The circuit design of the robotic arm system incorporates several key components, including servo motors, a 12V DC motor, an Arduino Uno microcontroller, and a 12V 5A AC power adapter. The circuit is designed to enable precise control and manipulation of the robotic arm for object sorting based on shape and color. The novelty of the circuit lies in its integration of different components to achieve the desired functionality. The Arduino Uno microcontroller serves as the central control unit, coordinating the actions of the servo motors and the DC motor. Fig. 4 shows the circuit diagram of the system.

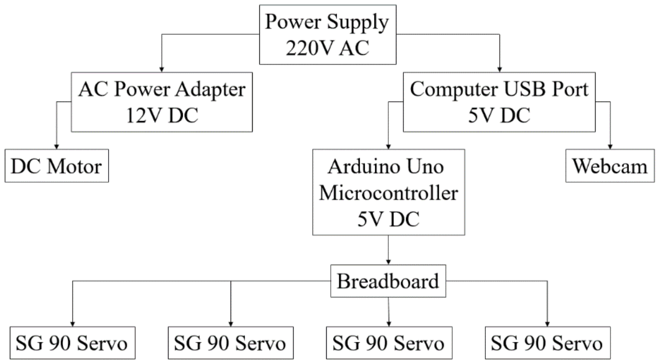

Fig. 4 Circuit diagram of the system

It receives input from the video stream captured by the camera and processes the frames using the OpenCV library. The servo motors, with their specified torque, operating speed, and range of rotation, provide the necessary actuation for the arm's base, main body, and claw. These motors allow the arm to rotate, move forward and backward, lift objects, and grip them securely. The specific angles and durations for the servo motor movements are programmed in the code to perform the desired sorting actions. The 12V DC motor, with its gear ratio and speed specifications, is likely employed to drive specific mechanisms or perform additional functions in the arm assembly.

While the exact details of its usage are not explicitly mentioned in the provided information, it could be utilized for tasks such as base rotation or additional arm movements. The 12V 5A AC power adapter is responsible for providing the necessary power to drive the entire system. It supplies the required voltage and current to ensure reliable and consistent operation of the motors and the microcontroller. The logic flow of the circuit involves capturing video frames, processing them using OpenCV for color and shape analysis, and based on the identified objects, controlling the servo motors to perform the appropriate sorting actions.

The code implements various image processing techniques, such as color space conversion, thresholding, contour detection, and shape approximation, to accurately identify objects and classify them based on their shape and color. The novelty of the circuit design lies in its integration of image processing algorithms with the control of a multi-axis robotic arm. By combining the power of OpenCV for real-time object detection and analysis with the precise control of servo motors, the system enables automated sorting based on shape and color.

6) Flowchart of the Sorting Process: Fig. 5 shows flow chart of the sorting process.

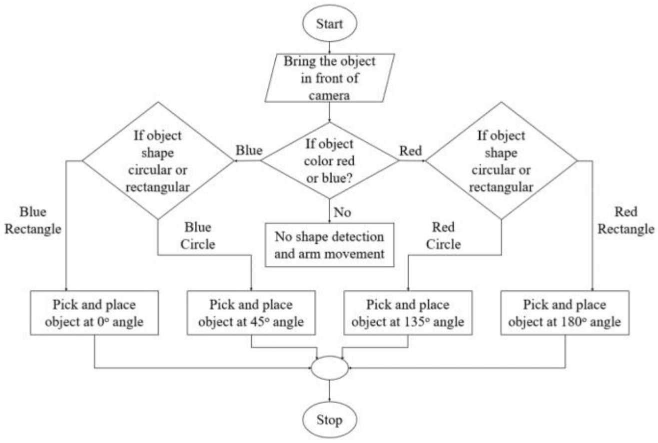

Fig. 5 Flow chart of the sorting process

The algorithm used in the provided code combines computer vision techniques with Arduino control to create a real-time object detection and sorting system. Here's an explanation of why this specific algorithm was chosen over others:

Color-based object detection: The algorithm leverages the HSV color space to detect objects based on their color. HSV representation is often preferred for color-based object detection as it separates the color information (hue) from brightness and saturation. This makes it more robust to changes in lighting conditions and shadows compared to other color spaces like RGB or grayscale.

Shape approximation: The algorithm utilizes contour detection and shape approximation techniques to determine the shape of the detected objects. By approximating the contours, it can classify objects as either rectangles or circles based on the number of vertices. This approach provides a simple and effective way to categorize shapes in real time.

Real-time processing: The algorithm is designed to process video frames in real time, allowing for live object detection and sorting. By continuously capturing frames from the camera, it can detect and respond to objects on the fly, making it suitable for interactive applications and dynamic environments.

Integration with Arduino: The algorithm integrates with an Arduino board to control a robotic gripper. By sending signals to the Arduino, it can manipulate the gripper based on the detected shape and color. This combination of computer vision and hardware control enables the system to perform physical sorting tasks based on visual cues.

Simplicity and versatility: The chosen algorithm strikes a balance between simplicity and versatility. It uses straightforward techniques like color thresholding, contour detection, and shape approximation, making it relatively easy to understand and implement. Moreover, by adjusting the color thresholds and shape criteria, the algorithm can be adapted to detect and sort objects of different colors and shapes, providing flexibility for various sorting scenarios.

While there are other object detection algorithms and frameworks available (such as deep learning-based approaches like YOLO or Faster R-CNN), they may require more computational resources, training data, and specialized hardware. The chosen algorithm, on the other hand, offers a simpler and more accessible solution for real-time object detection and sorting, combining traditional computer vision techniques with Arduino control.

3.2 Working Principal of the System

Here is how the whole system works to automatically sort objects based on shape and color:

1) At first, the code is run with PyCharm IDE, and the camera opens a Window on the desktop that shows an undefined color.
2) Then the object is brought in front of the webcam using the belt conveyor. Here the object is placed on top of the belt and then the forward switch is pressed.
3) As soon as the object comes in front of the camera, the code enables the camera to automatically detect the color of the object.
4) Then another Window opens by the code which enables the camera to detect the shape of the object.
5) After detecting the color and the shape, the code sends a signal to the Arduino Uno microcontroller to operate the servo motors of the robotic gripper.
6) Based on the shape and the color, the robotic gripper then places the object in either one of the 4 co-ordinates:
   a) If the color is blue and the shape is rectangular, the object is placed at a 0° angle.
   b) If the color is blue and the shape is circular, the object is placed at a 45° angle.
   c) If the color is red and the shape is rectangular, the object is placed at a 180° angle.
   d) If the color is red and the shape is circular, the object is placed at a 135° angle.

This is how the whole system works to automatically sort objects of different shapes and colors. Arduino Uno is used as a microcontroller board for the object sorting system. While Arduino Uno is not typically considered an industrial-grade system, it has been used in this context as a model or prototype to demonstrate the concept and functionality of the sorting system. The choice of Arduino Uno in this implementation is primarily driven by its accessibility, ease of use, and widespread adoption in the maker and prototyping communities. Arduino boards, including Arduino Uno, offer a user-friendly development environment, a range of input/output pins, and extensive community support.

These factors make Arduino Uno an ideal choice for quickly developing and testing proof-of-concept systems, such as the object sorting system described in the code. However, in an actual industrial setting, where robustness, scalability, and reliability are crucial, a more advanced and powerful microcontroller or industrial-grade system would be required. These systems often offer features like higher processing power, expanded input/output capabilities, industrial communication protocols, and rugged designs to withstand harsh industrial environments. The implementation described in the code and the provided paper data serve as a starting point or an initial prototype to showcase the feasibility of the object sorting concept.

When transitioning this system to an industrial setting, it would be necessary to select an appropriate microcontroller or industrial automation platform that meets the specific requirements and demands of industrial applications. Using Arduino Uno in the initial development stage, allows for rapid prototyping, iterative testing, and validation of the concept before investing in more specialized and industrial-grade hardware. This approach helps to reduce development time, cost, and risks associated with implementing a complex system directly in an industrial environment.

4 Results and Discussions

Results are the outcomes that are perceived after running a system. Here the system built into this research work automatically sorts objects based on shape and color. After testing several times, the results helped to identify how accurate and precise the sorting system was. Here, two shapes and two colors were used to test the accuracy and precision of the system. In this chapter, the accuracy and precision of the system are discussed via a few tables. Finally, a discussion is included based on the results that are found.

4.1 Accuracy and Precision

The tables below show the accuracy and the precision of the system for sorting 2 different colors and shapes:

Table 2 Color Calibration of the Camera

Actual Color	Color Detected by Camera			Accuracy	Precision
	1st Value	2nd Value	3rd Value		
Red	Red	Red	Red	100%	High
Blue	Blue	Blue	Blue	100%	High

Table 3 Shape Calibration of the Camera

Actual Shape	Shape Detected by Camera			Accuracy	Precision
	1st Value	2nd Value	3rd Value		
Rectangular	Rectangular	Rectangular	Rectangular	100%	High
Circular	Circular	Circular	Circular	100%	High

Table 4 16 Samples' Sorting Chart on the basis of Color and Shape

Sl. No.	Actual Color and Shape	Detected Color and Shape	Angle of Placement	Accuracy	Precision
1	Blue Rectangle	Blue Rectangle	0°	100%	High
2	Blue Circle	Blue Circle	45°	100%	High
3	Red Rectangle	Red Rectangle	135°	50%	Medium
4	Red Circle	Red Circle	135°	100%	High
5	Blue Rectangle	Blue Rectangle	0°	100%	High
6	Red Rectangle	Red Rectangle	180°	100%	High
7	Red Circle	Red Circle	135°	100%	High
8	Blue Rectangle	Blue Rectangle	45°	50%	Medium
9	Blue Circle	Blue Circle	45°	100%	High
10	Red Circle	Red Circle	135°	100%	High
11	Blue Rectangle	Blue Rectangle	0°	100%	High
12	Blue Circle	Blue Circle	45°	100%	High
13	Red Circle	Red Circle	135°	100%	High
14	Red Rectangle	Red Rectangle	135°	50%	Medium
15	Blue Circle	Blue Circle	45°	100%	High
16	Red Rectangle	Red Rectangle	180°	100%	High

4.2 Discussion on Results

This chapter showed several tests performed on the object to identify the shapes and colors and then sort the objects using a robotic gripper at desired angles. After the tests, the results were put down in a table which finally showed the accuracy and the precision. After running the system several times, it is seen that the accuracy and precision are quite good. If the color and shape detection is done using Python OpenCV, then it is always precise and accurate. Moreover, a camera of higher resolution and better specification is also responsible for the outcome. Finally, if the assembly of the robotic gripper is done correctly and the codes are put in proper order, then the sorting is also precise and accurate. The angle accuracy is quite high with an error of ±5%.

In certain instances, the accuracy of the system may experience a reduction of up to 50% when operating at specific angles. This decrease in accuracy can be attributed to environmental factors, particularly variations in lighting conditions, which can impact the camera's ability to accurately capture the true colors or shapes of objects. Lighting plays a crucial role in computer vision systems as it affects the way objects are perceived by the camera. When the lighting conditions are not optimal or inconsistent, the camera may struggle to accurately distinguish between different colors or accurately detect shapes. This can lead to a decrease in the system's overall accuracy when identifying and classifying objects based on their color or shape characteristics. Lighting conditions can vary depending on the environment in which the system is deployed. Factors such as natural lighting, artificial lighting, shadows, and reflections can all contribute to the fluctuations in lighting conditions. These variations pose a challenge for the camera's image processing algorithms, potentially causing a decline in accuracy at specific angles where the impact of lighting is more pronounced.

5 Conclusions and Future Work

In this era of automation, industries around the world are using the most advanced technologies to reduce the time of production as well as save costs. A great contribution can be made here by automatic object sorting via image processing for shape and color detection. A robotic arm that is capable of automatically sorting objects based on shape and color will cut the cost of labor and increase efficiency in the sorting and packaging of products. So, all in all, an advanced object-sorting robotic arm can be a huge benefit for any industry in the future.

A. Recommendations

There are certain things that are recommended for this research. For example,

- The servo motors should be connected to the correct PWM pin of the Arduino. Because, in the code, the pins are defined, and they control which servo should be rotated. The ground and the power connection should also be checked.
- It is important to check the USB port where the Arduino Uno microcontroller is connected. Because, in Python, the Arduino Uno microcontroller is imported via the PyFirmata library, and it is necessary to define the port in the code.
- When the webcam is connected to the computer, it also needs to be defined correctly in the code. Without properly defining the camera, the code will not open the right camera and the system will not work properly.
- Another important recommendation is to use an adapter to supply power to the DC motor of the belt conveyor. Because there is a voltage limit for the motor excess voltage will burn the coil and the motor will fail.

B. Suggestions for Future Work

Suggestions for future work means suggesting such methods that provide a further implementation of this research work. Nowadays automatic sorting process is not only a low-cost operation method but also plays a vital role in the industrial enhancement of any country. Here, this research has been developed for a color and shape-based sorting system and a simple pick-and-place mechanism of the robotic gripper. But this can be improved by:

- Adding a stronger and more versatile robotic gripper arm.
- Adding weight, height, size, and multiple colors, to the objects.
- Automating the belt conveyor and merging it with the whole system.

However, by improving this research work, it can be implemented in production plants to increase efficiency and save time on production as well as reduce cost.

In this work, a small-scale prototype of an industrial sorting system was used to sort objects based on various shapes and colors. However, this can be implemented in industries by making a system on a bigger scale for which a few modifications will be necessary. First, the arm body in this prototype was made of plastic whereas a more durable but lightweight material (such as aluminum alloys) can be used to make the body of the arm. The servo motors that are used in this work to control the arm are less powerful whereas a more powerful motor can help to lift heavier objects. Furthermore, more complex objects with complex shapes and various colors can be handled by implementing image processing in a more versatile way. In this project, the OpenCV library function of Python was used to identify a color by measuring the hue and other parameters. Moreover, the shapes were identified by calculating the contours where OpenCV was used as well. But in industries, more shapes and colors can be detected by either using this method or by implementing other methods of image processing. Overall, there are definite ways to improve the system and upgrade it to an industrial level by improving the specifications of the components used in this work.

Acknowledgments

The Chittagong University of Engineering & Technology’s Mechanical Engineering department provided us with some helpful technology, for which we are appreciative. We want to express our sincere appreciation to everyone who helped us in any manner throughout this research’s development. Lastly, we want to thank the Almighty for everything He has made possible.

References

[1] Gonzalez, R.C. and Woods, R.E. (2018) Digital Image Processing. Uttar Pradesh, India: Pearson.

[2] Groover, M.P. et al. (1986a) Industrial Robotics: Technology, programming and applications. New York: McGraw-Hill.

[3] Siciliano, B., Sciavicco, L. and Villani, L. (2009) Robotics modelling, planning and Control. New York: Springer.

[4] Pratt, W.K. (2007) Digital Image Processing: PIKS scientific inside. Hoboken, NJ: Wiley-Interscience.

[5] Robotics: Modelling, planning and control (2009a). London: Springer.

[6] CORKE, P. (2023) Robotics, vision and Control: Fundamental Algorithms in MATLAB. S.l.: SPRINGER.

[7] CRAIG, J.J. (2005) Introduction to robotics: Mechanics and control. Upper Saddle River: Pearson Prentice Hall.

[8] Joy, A., 2014. Object sorting robotic arm based on colour sensing. *Int. J. Adv. Res. Electr*, *3*(3), pp.7741-7746.

[9] Nicolaus, K., Hooper, J., Wood, R. and Ham, C., 2016, October. Development of an autonomous ball-picking robot. In 2016 International Conference on Collaboration Technologies and Systems (CTS) (pp. 373-378). IEEE.

[10] Jia, Y., Yang, G. and Saniie, J., 2017, May. Real-time color-based sorting robotic arm system. In 2017 IEEE International Conference on Electro Information Technology (EIT) (pp. 354-358). IEEE.

[11] Shah, R. and Pandey, A.B., 2018. Concept for automated sorting robotic arm. *Procedia Manufacturing*, *20*, pp.400-405.

[12] Sampreeth, A., Harsha, A. K., Rao, A., Desai, K. V., Rohith K., Praveena K. S., 2018. Object Sorting Robot Using Image Processing, International Journal of Engineering Research & Technology, 6(13), pp.1-4.

[13] Kale, V.R. and Kulkarni, V.A., 2013. Object sorting system using robotic arm. *International Journal of Advanced Research in Electrical, Electronics and Instrumentation Engineering*, *2*(7), pp.3400-3407.

[14] Amin, U., Ahmad, G., Liaqat, N., Ahmed, M. and Zahoor, S., 2014. Detection & Distinction of Colors using Color Sorting Robotic Arm in a Pick & Place Mechanism. *International Journal of Science and Research*, *3*(6), pp.1164-1168.

[15] Kunhimohammed, C.K., Saifudeen, K.M., Sahna, S., Gokul, M.S. and Abdulla, S.U., 2015. Automatic color sorting machine using TCS230 color sensor and PIC microcontroller, *International Journal of Research and Innovations in Science and Technology*, *2*(2), pp.33-38.

[16] Bhaskar, P. S., Dofe, S. S., Tripahi, S. S. and Banode, H. R., 2016. Colour Sorting System with Robotic Arm, *International Journal for Innovative Research in Science & Technology*, *2*(10), pp.267-272.

[17] Deshmukh, A., Nagane, M. and Awatade, V., 2016. Design & Development of Automatic Conveyor Controlling System for Sorting of Component on Color basis. *Red*, *630*, p.780.

[18] Shirgave, S., Salunkhe, A., Shirgave, K. and Upadhye, S.Y., 2017. Color sorting robot. *International Journal of Advanced Research in Computer and Communication Engineering*, *6*(3), pp.2278-1021.

[19] Suryawanshi, S., Sonone, S., Patil, P. and Parbhane, P., 2017. Color Sorting Robotic Arm. *International Research Journal of Engineering and Technology*, *4*(10), pp.1011-1013.

[20] Patel, H., Joy, R., Macwan, S. and Modi, H., 2018. IOT color based object sorting machine. *International Journal of Applied Engineering Research*, *13*(10), pp.7383-7387.

[21] Jakkan, D.A., Sudhakar, C.B., Vilas, J.S. and Aslam, K.U., 2019. Color based product sorting machine using IoT. *Journal of Embedded Systems and Processing*, *4*(3), pp.25-29.

[22] Patil, P. B., Patil, S. S. and Harugade, M. L., 2019. Review on Colored Object Sorting System Using Arduino UNO. *International Research Journal of Engineering and Technology*, *6*(05), pp.6181-6184.

[23] Sireesha, T., Raghuram, C. H., Surya, K. V., and Venkat, T., 2021. Automated Sorting System Based on Color and Thickness of Waste Management. *International Research Journal of Engineering and Technology*, *8*(2), pp. 229-232,.

[24] Ghosh, A., Mukherjee, D., Das, D., Chakraborty, M., Chandra, S., Mitra, S., Saha, N., and Saha, I., 2019. Colour based Product Organization Tool using Arduino, *International Journal for Research in Applied Science & Engineering Technology*, *7*(5), pp.1895-1898.

[25] Kamboj, D.S. and Diwan, A., 2019. Development of Automatic Sorting Conveyor Belt Using PLC. *International Journal of Mechanical Engineering and Technology*, *10*(8).

[26] Shen, L.J. and Hassan, I., 2015. Design and development of colour sorting robot. *Journal of Engineering Science and Technology*, *10*, pp.71-81.

[27] Zulfiqar, R., Mehdi, B., Ifthikar, R., Khan, T., Zia, R. and Saud, N., 2019, January. PLC based automated object sorting system. In 2019 4th International Electrical Engineering Conference (IEEC 2019) (pp. 1-7).

[28] Nuva, T.J., Ahmed, M.I. and Mahmud, S.S., 2022. Design & Fabrication of Automatic Color & Weight-Based Sorting System on Conveyor Belt. *Journal of Integrated and Advanced Engineering*, *2*(2), pp.147-157.

SciEn
Journal of Engineering Advancements Vol. 04(03) 2023, pp 80-89 https://doi.org/10.38032/jea.2023.03.004

Study on Transmission of Visible Light in Selected Water Bodies of Southwest Nigeria for Underwater Wireless Optical Communication

Oluwabukola A. Ojediran[*], *Akinlolu A. Ponnle, and Samson A. Oyetunji*

Department of Electrical and Electronics Engineering, Federal University of Technology, Akure, Ondo State, Nigeria

Received: May 10, 2023, Revised: August 25, 2023, Accepted: August 25, 2023, Available Online: September 16, 2023

ABSTRACT

A study on the transmission of visible light (400 nm-800 nm) in some selected natural water bodies of Southwest Nigeria was carried out via spectroscopy, and their salinity, total dissolved solids, and electrical conductivity were obtained. Samples of ten selected water bodies comprising rivers, lagoons, and the Atlantic Ocean were taken namely: River Ala, River Ogbese, River Kinira, River Apake, River Odo-Oru, River Odo-Eran, Epe Lagoon, Lagos Lagoon (Lekki Phase 1), Lagos Lagoon (Victoria Island) and the Atlantic Ocean. The absorption of light in them was measured using a spectrophotometer. From the results of the measurements, the rivers showed less conductivity, total dissolved solids, and salinity compared to the lagoons, and the Atlantic Ocean. The Atlantic Ocean gave the highest value. Also, there is varying optical attenuation with different wavelengths. At shorter wavelengths (blue light), there is higher absorbance with an increase in salinity compared to longer wavelengths (red light). At the infra-red end (750 nm – 800 nm), all the samples showed increased absorbance compared to the absorbance at red wavelength (700 nm). From the measurements, an optical beam of a wavelength of 650 nm was found most suitable for optical communication across these water bodies. The transmission was simulated at this wavelength for the water bodies using OptiSystem software linked with MATLAB at different data rates, and their performance was investigated in terms of received quality factor and bit error rate. The quality factor reduces with an increase in salinity, while the bit error rate increases with an increase in salinity.

Keywords: Absorbance, Salinity, Electrical Conductivity, Underwater Wireless Optical Communication, Quality Factor.

1 Introduction

Underwater Wireless Optical Communication (UWOC) has assumed great significance due to its wide application including research, and military operations. It is useful in communication in water (which is a difficult terrain for human beings), security, surveillance, and environmental monitoring for disaster prevention.

Water is an important necessity and a vital resource to man, animals, and plants. Water is used for several purposes: domestic use such as drinking, cooking, and washing, and for agricultural purposes [1]. There are various sources of water in the world. Some of these include rivers, lakes, oceans, streams, and lagoons. About two-thirds of the earth's surface is made up of water [2]. All the bodies of water on earth, such as oceans, lakes, rivers, etc., contain salt of varying concentrations which cause attenuation of light signals. Sea water contains about 35 parts per thousand of salts and is denser than freshwater. One of the most abundant salts in seawater is sodium chloride [3].

In UWOC, absorption and scattering affect the transmission of optical signals, which reduces the power and the effective communication range in the medium. Most water bodies are saline in nature with the limitations of absorption and scattering due to dissolved salts. The preferred range of wavelengths for transmission in particle-free sea water is the blue-green region (450 nm - 570 nm) because of low attenuation at these wavelengths [4]. However, when dissolved salt is present in the water, the attenuation increases at shorter wavelengths (blue-green) than at longer wavelengths (red). Over the years, researchers have been investigating factors that affect the performance of UWOC links.

In literature, some researchers have studied the transmission of optical signals in saline water and some natural water bodies. Authors of [5] measured the absorption coefficient of pure and saltwater in the visible and infra-red range at 15 discrete wavelengths. The temperature and salinity of the water were varied to study their effect on the absorption coefficient of liquid water. Their study revealed that the absorption coefficient of water is highly dependent on temperature in the near infra-red region than in the visible region except around 610 nm. The saltwater solution gave similar results for temperature dependence. An increase in salinity increases the absorption coefficient.

Authors of [6] studied the capability of UWOC links in the Bay of Bengal. Water samples were collected at different locations in the Bay of Bengal (harbor, coastal, and deep-water). The optical attenuation for the different types of water was determined. A numerical model was developed, and simulations of the seawater samples were done to obtain a communication range of 0.5m, 14m, and 35m in harbor, coastal, and deep-water locations respectively. Increasing the transmit power increases the communication range in the water.

Authors of [7] determined the extinction coefficient and transmittance of ocean water and shallow well water in Mombasa Kenya. The transmitted light intensities decrease exponentially with concentration in the two water bodies.

Authors of [8] showed how a message communicated with UWOC can be eavesdropped using a diffraction grating in municipal fresh water. It also showed that UWOC transmission is possible in the ultra-salty water of the Dead Sea.

*Corresponding Author Email Address: bukiojed@gmail.com

The authors of [9],[10] studied the effect of common table salt in water on the transmission of visible light in the wavelength range of 400 nm – 800 nm in different salt solutions of different concentrations ranging from 1g/100ml – 28g/100ml. The absorbance, conductivity, and total dissolved solids of the samples were measured. There is an increase in absorbance and conductivity with increased salt concentration. The absorbance is wavelength dependent with higher values at the blue end than at the red end of the spectrum with increased salt concentration. The performance of UWOC in the samples was also evaluated by simulation using OptiSystem software and showed that the achievable link distance reduced with increased salinity.

The author of [11] investigated the effect of salinity and turbidity in different salt concentrations (10 g/L - 40 g/L (representing the Red Sea salinity) via a white-LED transmitter. The received power decreased with link length and increase in salinity. The transmitted signals are more affected by turbidity than salinity. The transmission distance was limited to 60 cm due to turbidity. The white LED was able to send data at a maximum salinity value of 40 g/L.

Authors of [12] transmitted texts by Pulse Width Modulation (PWM) in an optical communication channel underwater at a wavelength of 532 nm. The salt concentrations were varied from 0 - 90% w/v ranging from clear water to turbid water. Results indicate that the attenuation coefficient is lower in a low concentration of sodium chloride like pure seawater while in turbid harbour water, a higher attenuation coefficient was obtained. The received power and signal-to-noise ratio was lower in the turbid harbour water compared to pure seawater.

Southwestern Nigeria falls within the rain forest belt of Nigeria with great fauna and flora. The people in this region are mainly of the Yoruba tribe and deal mainly in agriculture. In the northern part of this region are the western uplands, and in the southern part are lagoons and the Atlantic Ocean. Because of the uplands on the northern side, many rivers flow from the uplands towards the Atlantic Ocean. Most of these rivers are used mainly for agricultural, industrial, and commercial purposes.

The authors of [13] measured some water quality parameters of Ogbese River in Ondo State which is part of Southwest Nigeria such as electrical conductivity, pH values, total dissolved solids, etc., both during the dry season and wet season. The authors of [14] studied the pollution of Ogbese River in Ovia Northeast local government area of Edo State, Nigeria; and parameters such as pH, temperature, electrical conductivity, total dissolved solids, etc., were measured and analysed.

The authors of [1] assessed the seasonal surface water quality of the Ala River upstream in Akure, Ondo State of Nigeria. Some physicochemical parameters including pH, and total dissolved solids were measured and analysed. Authors of [15] studied the impact of environmental variables and processes of nutrient enrichment on the phytoplankton community at Epe Lagoon. Some physicochemical parameters including pH, total dissolved solids, and salinity were measured and analysed.

In this paper, the transmission of visible light in the waters of some selected rivers, lagoons, and the Atlantic Ocean in Southwest Nigeria was studied via spectroscopy. This kind of study via spectroscopy on these selected water bodies has not been carried out before in Nigeria. While measurements of salinity, electrical conductivity, and some other physiochemical properties of some of these water bodies have been done by some researchers for other purposes, however, the study of absorbance of these selected water bodies to visible light spectrum for optical communication purposes is still lacking. In this work, salinity, electrical conductivity, and total dissolved solids of these water bodies were also measured. Based on the absorbance measurements, this study helps to determine the most suitable wavelength for visible light communication across these selected natural water bodies of Southwest Nigeria at minimal attenuation. The performance of UWOC in them at this wavelength for different data rates was also investigated by simulation using OptiSystem software.

2 Properties of Water

2.1 Optical Properties

The two main optical properties of water which are inherent are absorption and scattering, and they are both dependent on wavelength. The irreversible loss of light intensity in water based on the refractive index of water and the spectral absorption coefficient is absorption [16]. Absorption of light in water is caused by the excitation of the water molecules and other dissolved particles when they are hit with photons of light [17]. The photons lose energy, which is converted into other forms [18].

Scattering is the deflection of light from its main path due to water molecules and suspended particles but with no change in energy [19],[20]. The particles might be comparable in size to the light wavelength leading to diffraction, or the particles might have a refractive index that varies from that of the water leading to refraction [21].

The attenuation coefficient c(λ) is the linear combination of the absorption coefficient, a(λ), and the scattering coefficient b(λ), as expressed in Eq. (1) [4].

$$c(\lambda) = a(\lambda) + b(\lambda) \tag{1}$$

2.1.1 Spectroscopy

A spectrophotometer measures the intensity of light relative to wavelength. It measures the absorbance and/or transmittance of light through a substance [22]. Absorbance (A) is expressed in Eq. (2) from Beer's law as,

$$A(\lambda) = \varepsilon(\lambda) lC \tag{2}$$

where ε is the molar absorptivity which depends on wavelength, l is the length of the path of light through the substance, and C is the concentration.

From [23], the transmittance is related to the absorbance by Eq. (3)

$$T(\lambda) = 10^{-A(\lambda)} \tag{3}$$

Absorption coefficient α(λ) is related to absorbance by Eq. (4) [24]

$$a(\lambda) = (\ln(10)) A(\lambda) \tag{4}$$

2.1.2 Underwater Wireless Optical Communication

(A) Underwater Optical Channel

Beer Lambert's law relates the transmitted optical power with respect to distance and attenuation in the medium which is wavelength dependent as expressed in Eq. (5).

$$P_r(d, \lambda) = P_o e^{-c(\lambda) d} \tag{5}$$

where P_o is the initial optical transmit power, and $P_r(d,\lambda)$ is the received optical power in the medium at distance d, λ is the wavelength, and c(λ) is the attenuation coefficient expressed in Eq. (1) [2].

(B) Quality (Q) Factor

Quality Factor (Q) is a function of the optical signal-to-noise ratio (OSNR) which provides a description of the receiver performance. The quality factor is a measure of how noisy a pulse signal is, and the eye pattern helps to evaluate the Q factor. A large Q factor means that the pulse is relatively free from noise. The Q factor is expressed in Eq. (6)

$$Q = \frac{I_1 - I_o}{\sigma_1 - \sigma_2} \quad (6)$$

I_1 is the 1-bit current value, I_o is the 0-bit current value, σ_1 is the standard deviation of the 1-bit current and σ_2 is the standard deviation of the 0-bit current [25],[26].

The logarithmic value of Q (in dB) is related to the OSNR by Eq. (7):

$$Q_{dB} = 20 \log \sqrt{OSNR} \sqrt{\frac{B_O}{B_E}} \quad (7)$$

where Q is the Q factor, B_O is the optical bandwidth of the receiver photodetector, and B_E is the electrical bandwidth of the receiver filter [26].

2.2 Physiochemical Properties

2.2.1 Salinity

The dissolved salt content in a body of water is salinity which is measured in kilogram of salt per liter of water equal to parts per thousand (ppt). Salinity is important in determining the chemistry of natural waters. Conductivity measures the ability of water to conduct electricity. Dissolved salts conduct electricity hence, conductivity increases as salinity increases [10]. Total dissolved solids (TDS) measure the organic and inorganic substances in a liquid often reported in parts per million. It is applied in the study of water quality for rivers, lagoons, and oceans.

The values of the salinity of some rivers in Southwest Nigeria are Osun River: 0.06 - 0.17 ppt [27]; Ogun River: 50 - 280 mg/L TDS [28]; Osse River: 0.13 – 0.37 ppt [29]. Seawater has average salinity of about 33 - 38 ppt [30].

2.2.2 Different Types of Open Water

There are four main types of open water. They are pure sea water, clear ocean water, coastal ocean water and turbid harbor. In pure sea water, absorption is the major limiting factor, which is the sum of absorption in pure water and absorption by salts like NaCl, $MgCl_2$, Na_2O_4, and KCl. The absorption in pure sea water is increased in the presence of salts and increases with increase in wavelength. Clear ocean water has a higher concentration of salts, mineral components, and organic matter that cause absorption and scattering [31].

Coastal ocean water has more dissolved particles such as water molecules, suspended particles, dissolved salts, mineral and organic matter, phytoplankton, chlorophyll, etc., which increased its turbidity, absorption, and scattering. Turbid harbor has the highest concentration of particles (both dissolved and in-suspension) and hence, the transmission of visible light in it is highly limited by absorption and scattering [3],[31].

3 Materials and Method

3.1 The Study Areas

The selected water bodies in Southwest Nigeria were taken from three different states: Ondo State, Oyo State and Lagos State. The water bodies are Rivers Ala and Ogbese in Ondo State; Rivers Kinira, Apake, Odo-Oru and Odo-Eran in Ogbomoso, Oyo State; and Epe Lagoon, Lagos Lagoon (Lekki Phase 1), Lagos Lagoon (Victoria Island), and the Atlantic Ocean in Lagos State.

One of the important rivers in the central and northern parts of Ondo State, Nigeria is Ogbese River. The source of the river is from Ayede-Ekiti in the western uplands of northern part of Ekiti State, flowing through Ayede-Ogbese town in Ondo State and empties into Ose River in the western part of Edo State. Ogbese town is about 10 km east of Akure which is Ondo State's Capital [13],[32]. River Ogbese is used for agricultural, industrial, and commercial purposes. Wood processing and food processing companies utilize water from the river daily. Ogbese community depends on the river for some other activities such as laundry and disposal of wastes. The use of fertilizers around the farmlands in the areas results in chemical substances in the river. Industrial wastes also flow into the river [13],[14].

Ala River flows from the Northwestern part of Akure to the Southeastern part. It is one of the main tributaries of Ogbese River. The length of the river is about 58 km, with about 14.8 km of it flowing through Akure township [1]. It flows through areas such as Obanla, Awule, Adegbola, Araromi, Oke-Ijebu, Alagbaka and Oba-Ile in Akure town. It also flows downstream to rural towns like Ajegunle, Owode, Ayetoro, Araromi and Ilado [1]. The river is used for irrigation, domestic use, and religious use.

Ogbomoso town is blessed with many rivers such as rivers Kinira, Apake, Odo-Oru and Odo-Eran (Animal River). Poor waste management results to the dumping of wastes along the river course causing great risk to public health. These rivers contain industrial wastes and domestic wastes. Kinira River contains detergents, sewage, and organic chemicals; Odo-Oru River contains plastics, garbage, detergents, sewage, and herbicides; Apake River contains detergents, plastics, garbage, pesticides, oil and cleaning solvents, and sewage while Odo-Eran River has a cow abattoir and both the blood and the animal dung are discharged into the river without treatment. Along the riverbanks, farmers plant maize, yam, and vegetables, and the fertilizers applied to the plants run off into the rivers [33].

Epe Lagoon is between Lekki Lagoon in the east and Lagos Lagoon in the west [34]. River Osun flows into the lagoon. The major source of livelihood for the people is fishing by making use of canoes and boats. Varieties of fish species such as croaker, bonga, catfish, sardine, shiny-nose, and tilapia are caught and taken to the Epe market (which is the biggest seafood market in Lagos) for sale. Aquatic species like crabs, prawns, shrimps, crayfish, turtles, lobsters, and snails are found in the lagoon. The vegetation surrounding the lagoon is swampy mangrove. The lagoon contains domestic wastes and industrial wastes [35].

Lagos Lagoon (Lekki Phase 1) is a large expanse of water between the Atlantic Ocean and Lagos State. The lagoon is utilized for fishing (which is the main occupation of the people living around the lagoon), washing cars, and other domestic uses. Domestic wastes are also being deposited at the shore. Sand-filling companies pack sand for plastering at the bank of the lagoon.

Lagos Lagoon (Victoria Island) lies between the Atlantic Ocean and Lagos State. The lagoon contains different species of fish and aquatic organisms that provide income and food for the people. These are caught with the aid of boats. It is in between two Islands: Victoria Island and Lagos Island. A channel links the northeast of the lagoon to the Lekki Lagoon passing by south of Epe town. Lagos Lagoon empties into the Atlantic Ocean at the Lagos Harbour [36]. There is urban and industrial waste in the lagoon due to wastewater entering the lagoon daily. River Ogun and a tributary of River Osun flow into it and contribute to the waste [37].

The Atlantic Ocean is the second largest among the world's five oceans: Pacific, Atlantic, Indian, Southern Antarctic, and Artic. It covers about 20% of the Earth's surface. The Ocean is bounded on the east by Africa and Europe, and on the west by the Americas. The salinity is between 33 ppt and 38 ppt varying with season and latitude. It is considered the saltiest major ocean. The effects of river inflow, evaporation and precipitation affect the salinity value. The electrical conductivity (EC) is between 3 - 6 S/m. The Atlantic Ocean provides lots of fish (various species) annually for human consumption and the industries [30]. The Atlantic Ocean in Nigeria is part of the North Atlantic and is a route for international trade in Nigeria. It is utilized for exportation and importation of goods and mineral resources (crude oil, cocoa, rubber, palm oil, groundnut, coal, timber) in Nigeria [38]. There are many beaches at the shore of the Atlantic Ocean in Nigeria, some are: Oniru beach, Eleko beach, Alpha beach, Bar beach, Elegushi beach and Kuramo beach. Table 1 shows the selected water bodies, their coordinates, and length. For some bodies, surface area is provided.

Table 1 Location coordinate, and length (or surface area) of the selected water bodies

River	**Coordinate**	**Length (or surface area)**
Ogbese	6.72° N, 5.43° E to 7.28° N, 6.57° E [32]	180 km [32]
Ala	7.26° N, 5.26° E [1]	58 km [1]
Kinira	8.15° N, 4.20° E [33]	4.8 km [33]
Odo-Eran	8.15° N, 4.24° E [33]	
Apake	8.13° N, 4.24° E [33]	
Odo-Oru	8.13° N, 4.27° E [33]	
Epe Lagoon	6.58° N, 3.98° E [34]	(243 km^2) [34],[15]
Lagos Lagoon (Lekki Phase 1)	6.50° N, 3.52° E [36]	Over 50 km [39], (6,354.7 km^2, combined) [36],[39]
Lagos Lagoon (Victoria Island)	6.45° N, 3.47° E [36]	
Atlantic Ocean (Elegushi Beach)	6.42° N, 3.61° E [40]	(85,133,000 km^2, worldwide) [30]

3.2 Collection of Water Samples

Samples of the ten water bodies were collected at Ayede-Ogbese (for River Ogbese), Oba-Ile Housing Estate (for River Ala), Kinira (Kinira River), Ori-Oke Grammar School (for Odo-Eran River), Oke-Elerin Baptist School (for Apake River), Ifeoluwa Baptist Church (for Odo-Oru River), Epe town (for Epe Lagoon), Lekki Phase 1 (for Lagos Lagoon), Victoria Island (for Lagos Lagoon), and Elegushi Beach (for Atlantic Ocean). Fig. 1 shows part of the Atlantic Ocean at Elegushi beach.

Collection of the water samples from the rivers, lagoons and the ocean were done during the rainy season. The water samples were taken with the aid of plastic bottles properly rinsed with clean water prior to being filled with water from the river, lagoon, or ocean. The samples were collected at about 30 cm below the water surface in the direction of the current flow and covered with a cap immediately. The samples were labeled to avoid the error of mixing up the samples during measurements and analysis.

Fig. 1 The Atlantic Ocean at Elegushi beach in Lagos

3.3 Measurement of the Physiochemical Parameters and Absorbance of the Water Bodies

3.3.1 Physiochemical Parameters

The measurements of the physiochemical parameters of the ten water bodies were carried out by utilizing an electronic water quality tester, EZ-9909SP. Some of the measured parameters are salinity, electrical conductivity, pH, and total dissolved solids (TDS).

For the measurements, the cap of the water quality tester was removed, and the device was turned on. The meter was calibrated prior to taking the measurements. The probe was rinsed with distilled water and dipped into the sample of the saline water for a few seconds. The water level covered the probe and the temperature sensor point making sure there was no air bubble trapped on the probe. The sample was stirred gently utilizing the probe to have a homogenous sample. The knob on the meter was pressed to change the mode of the readings (salinity, electrical conductivity, pH, total dissolved solids (TDS) and temperature). The result of the stable readings for each parameter was taken. After each reading, the probe of the water quality tester was rinsed with distilled water prior to taking a new measurement from another sample. When the readings were completed, the probe of the water quality tester was rinsed with distilled water and dried with clean cotton wool.

3.3.2 Measurement of Absorbance

The absorption spectra of the different water samples in the visible light range were determined using a VIS-721 Visible Light Spectrophotometer which is shown in Fig. 2 The measurement of each water sample was done with the aid of a pipette and placed in a cuvette-length of 10 mm. A reference cuvette contained distilled water while the sample cuvette contained the water samples. Each water sample's absorption spectrum in the wavelength range of 400 nm – 800 nm was obtained at intervals of 50 nm and recorded.

Fig. 2 The VIS-721 Spectrophotometer

3.4 Underwater Optical Communication Simulation

From the absorbance measurements, the most frequent wavelength with the least absorbance among the ten water bodies was determined. This wavelength was used in the simulation of underwater optical communication by OPTISYSTEM software linked with MATLAB. The absorption coefficients at this wavelength from the measured absorbance values for the ten water bodies were determined and used in the simulation for the ten water bodies. Simulation was performed at 10 kb/s, 100 kb/s, 1 Mb/s, 10 Mb/s, and 1 Gb/s data rates for transmit power of 30 mW and transmission distance of 100 cm. The results were assessed in terms of the received quality factor (Q) and the bit error rate (BER). The simulation parameters are shown in Table 2, and the design layout of the UWOC in OptiSystem is shown in Fig. 3.

Table 2 Parameters for the underwater optical communication simulation at 650 nm for the ten water bodies

Parameters	Values
Operating wavelength of Laser	650 nm
Power of Laser	30 mW
Bit rate of bit sequence generator	10 kb/s, 100 kb/s, 1 Mb/s, 10 Mb/s, and 1 Gb/s
Modulation	Non return to zero on-off keying (NRZ OOK)
Amplitude of NRZ pulse generator	1a.u.
Modulation index of amplitude modulator	1
Responsivity of photodetector	1 A/W
Dark current of photodetector	10 nA
Cutoff frequency of filter	0.75 x Bit rate
Transmission distance	100 cm

A continuous wave laser produces the light at the specified wavelength and then passes to a Mach-Zender optical modulator. A pseudo-random bit sequence (PRBS) is passed into an NRZ Pulse Generator whose electrical output is passed to the Mach-Zender modulator to optically modulate the light. The modulated light passes through the water body represented by the MATLAB component, and a PIN photodiode receives the light signals at the receiver which converts it to electrical signals. The signals are passed through a Gaussian filter, and then through a 3R regenerator for analysis by the Eye Diagram Analyzer.

4 Results and Discussion

4.1 The Results from the Salinity Measurement

The measured physiochemical parameters of the ten water bodies of Southwest Nigeria are shown in Table 3. From Table 3, the electrical conductivity, salinity, and TDS of the rivers and lagoons increase as the water bodies get closer to the Atlantic Ocean (which has the highest salinity). The rivers sampled in Ondo State, and Oyo State are in the hinterland, far away from the Atlantic Ocean; hence their salinity is lower than those of Lagos Lagoon and the Atlantic Ocean.

The TDS, pH, salinity, and electrical conductivity of River Ogbese obtained from this study lies within the range obtained by [13] for wet season, and by [14]. The domestic and industrial wastes contribute to the total dissolved solids in the water hence increasing the salinity and the conductivity. The electrical conductivity, pH, salinity, TDS, and temperature of River Ala conform to the results obtained by [1]. Akure is an urban city and has a larger population than Ogbese. This increases human activities (and attendant industrial wastes) along the river; hence, the TDS and salinity are higher than River Ogbese. Oba-Ile is at the downstream of the river hence will have a higher TDS value than the upstream.

Kinira River is at the outskirts of the city of Ogbomosho with less human activities hence the conductivity, TDS, and salinity are lower than the other rivers sampled in the city. Apake, Odo-Oru and Odo-Eran are in the city with lots of human and industrial wastes hence, their TDS, conductivity, and salinity increases.

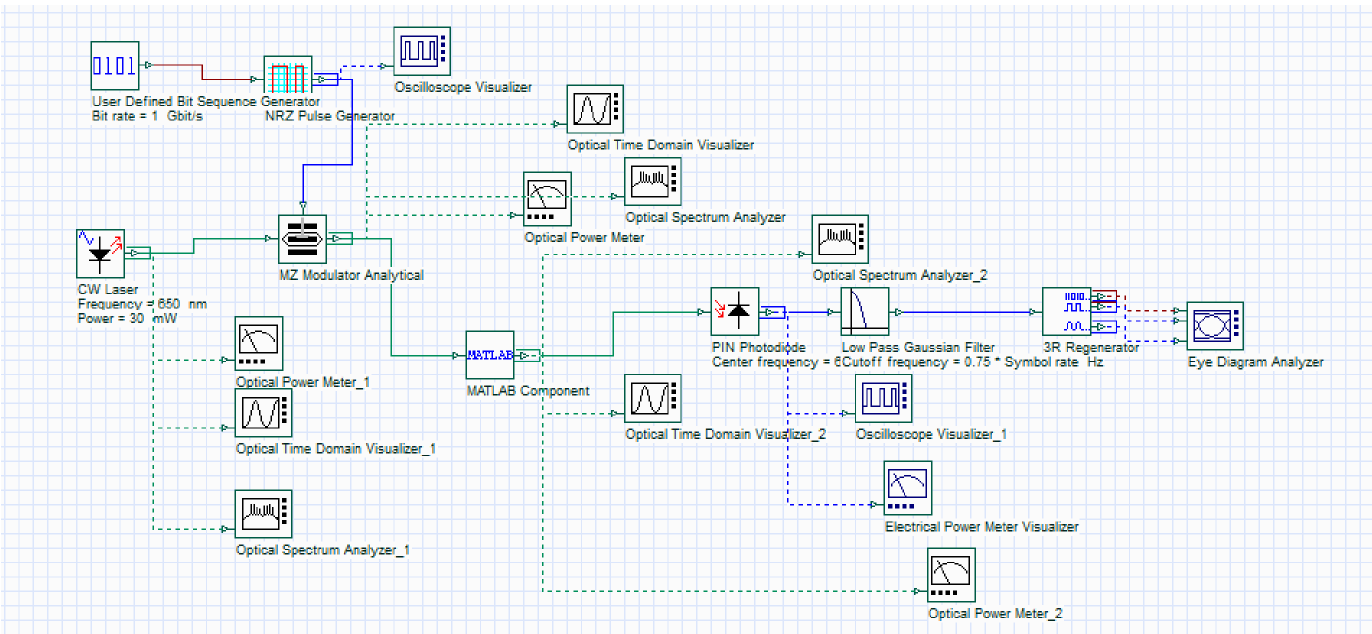

Fig. 3 Design layout of the UWOC in OptiSystem

Table 3 Measured parameters of the selected ten water bodies of Southwest Nigeria

State	Name of Water Body	Conductivity (μS/cm)	Temperature (°C)	TD Salt (ppt)	TDS (ppt)	Salt (%)	pH
Ondo	Ogbese River	185	23.8	0.093	0.094	0.00	5.86
	Ala River	297	23.1	0.149	0.150	0.01	5.90
Oyo	Kinira River	243	23.9	0.120	0.120	0.01	5.90
	Odo-Oru River	674	23.8	0.338	0.338	0.03	5.92
	Odo-Eran River	779	23.9	0.387	0.387	0.03	5.91
	Apake River	907	24.1	0.452	0.453	0.04	5.92
Lagos	Epe Lagoon	258	23.7	0.128	0.128	0.01	5.87
	Lagos Lagoon (Lekki Phase 1)	8090	23.8	4.050	4.130	0.41	5.89
	Lagos Lagoon (Victoria Island)	19750	23.9	9.920	11.30	1.08	5.87
	Atlantic Ocean	59400	23.7	30.00	37.00	3.70	5.96

Epe Lagoon has a somewhat low salinity, conductivity and TDS compared to those of some rivers in the hinterland despite having human activities such as fishing, farming and wastes from domestic use; and lying between Lagos Lagoon and Lekki Lagoon which are both close to the Atlantic Ocean. The values obtained in this study are close to the range of values obtained by [15]. This might be due to Osun River that empties into it which has low salinity, thereby diluting the Epe River and lowering its salinity and conductivity. The obtained salinity of the Atlantic Ocean is 37 ppt and electrical conductivity of 5.9 S/m which agrees with literature [30].

The variation of the electrical conductivity of the water bodies with the total dissolved salt and total dissolved solids is shown in Fig. 4.

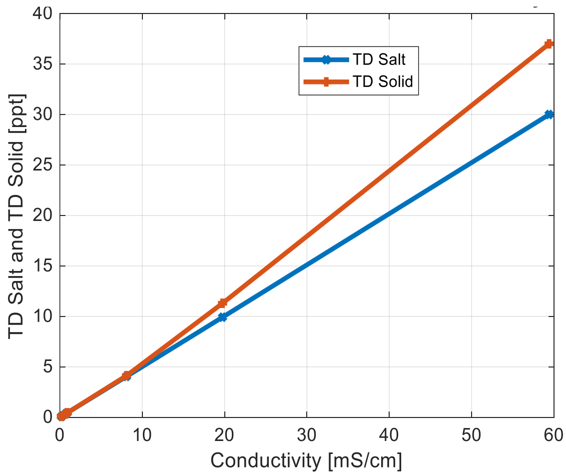

Fig. 4 Conductivity with TD salt and TD solid of the water bodies

There is a linear variation of the electrical conductivity of the water bodies with their total dissolved salts. This shows that any water body with high salinity will have high electrical conductivity and vice versa.

4.2 The Results of the Absorbance Measurement

The results of the measured absorbance within the visible wavelengths of 400 nm – 800 nm for the ten water samples are shown in Fig. 5 and Fig. 6. The rivers (Odo-Eran, Odo-Oru, Apake and Kinira in Oyo State; and Ala and Ogbese in Ondo State) have lower absorbance between 400 nm – 800 nm than the lagoons and the Atlantic Ocean in Lagos State, except Epe Lagoon.

In Fig. 5, River Apake has the highest absorbance, while the absorbance values of Odo-Eran, Odo-Oru, Ala, Epe, and Kinira reduces in this order with River Ogbese in Ondo State having the least absorbance which conforms to their salinity values.

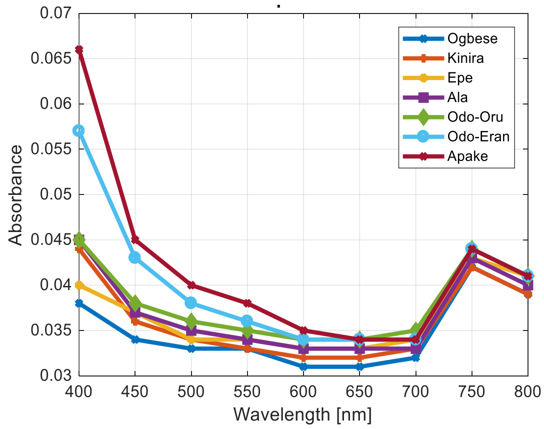

Fig. 5 Plot of the absorbance of the water bodies of Ogbese, Kinira, Epe, Ala, Odo-Oru, Odo-Eran, and Apake between 400 nm – 800 nm

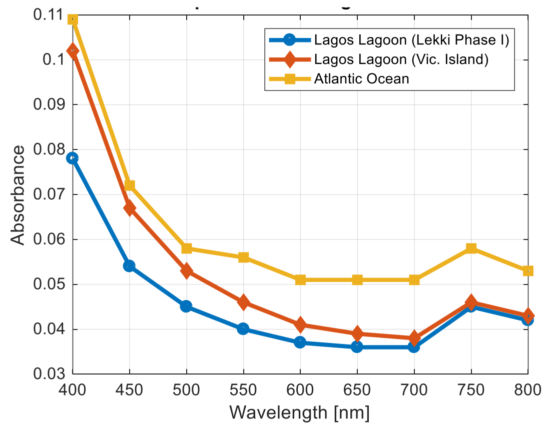

Fig. 6 Plot of the absorbance of Lagos Lagoon (Lekki Phase I and Victoria Island), and the Atlantic Ocean between 400 nm – 800 nm

For the lagoons and the Atlantic Ocean in Lagos State (Fig. 6), Epe Lagoon has the least absorbance, followed by Lagos Lagoon (Lekki Phase 1, Victoria Island) while the Atlantic Ocean has the highest absorbance with the corresponding highest salinity.

The absorbance of all the water bodies is higher at the shorter wavelengths of 400 nm –500 nm (violet–blue light) and decreases towards the longer wavelengths of 700 nm (red light). Between 700 nm – 750 nm (towards infra-red), the absorbance increases and then reduces between 750 nm – 800 nm. This implies that a lot of information would be lost if the shorter wavelengths are utilized for the transmission of signals in these water bodies unless there is an improvement in the transmission. Signal transmission using red light through the rivers, lagoons, and the ocean in the study will yield better reception at the receiver.

Fig. 7 shows the average absorbance with electrical conductivity of the water bodies. The average absorbance values for the water bodies were taken over the entire light spectrum of measurement (400 nm – 800 nm). The horizontal axis is in logarithmic scale. The rivers have lower average absorbance compared to the lagoons, and the highest is Atlantic Ocean.

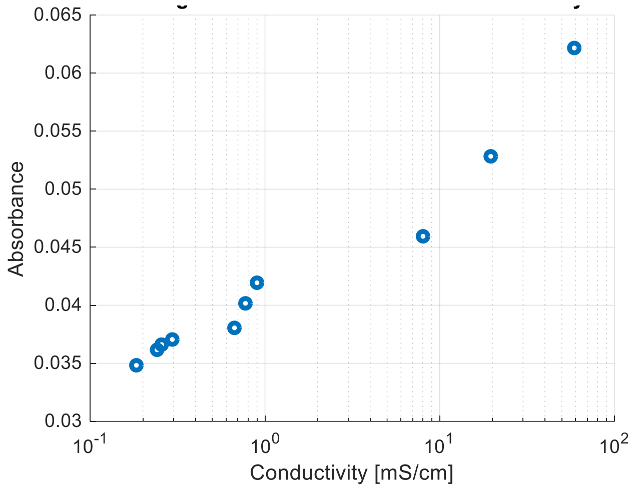

Fig. 7 Average absorbance with electrical conductivity of the ten water bodies. The horizontal axis is in logarithmic scale

4.3 Performance of the Underwater Visible Light Communication Simulation

Considering Fig. 5 and Fig. 6, all the water bodies have minimum absorbance between wavelengths of 600 nm and 700 nm. Four of them have from 600 nm – 650 nm, two of them have from 650 nm – 700 nm, and three of them have from 600 nm – 700 nm, while one of them has from 700 nm. Considering the wavelength with the least absorbance that is most frequently common among all the ten water bodies, it is found to be 650 nm which is away from green light but close to red light. Therefore, an optical beam of a wavelength of 650 nm would be suitable to use for optical communication in all the ten water bodies studied. This value was then used in the underwater visible light communication simulation described in Section 3.4.

Fig. 8 shows the pseudo-random bit sequence (PRBS) from the NRZ Pulse Generator in time domain at the transmitter side for Lagos Lagoon (Victoria Island) at 10 Mb/s, while Fig. 9 shows the same PBRS in time domain from the PIN photodiode receiver after covering 100 cm in the water. The figure shows that noise has been added to the signal with a reduction in signal amplitude. Fig. 10 shows the eye diagram of the detected PBRS signal after reception with a quality factor of 52.354.

Results of the simulation for the ten water bodies in terms of received quality factor (Q) and bit error rate (BER) at 10 kb/s, 100 kb/s, 1 Mb/s, 10 Mb/s, and 1 Gb/s data rate for transmit power of 30 mW and transmission distance of 100 cm are shown in Table 4 and Table 5.

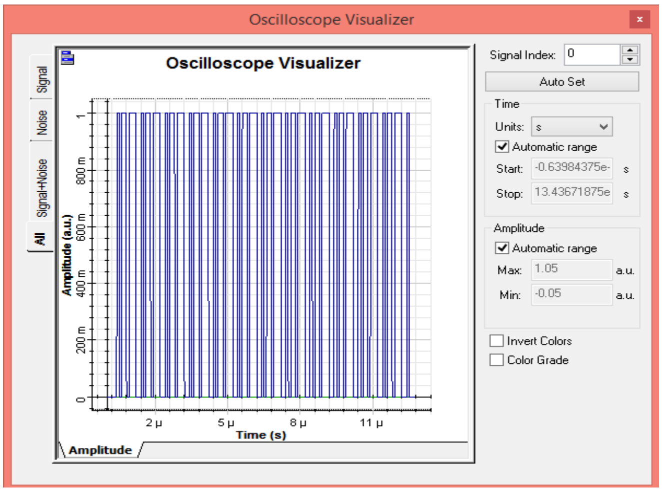

Fig. 8 The PRBS from the NRZ Pulse Generator in time domain at the transmitter side for Lagos Lagoon (Victoria Island) at 10 Mb/s

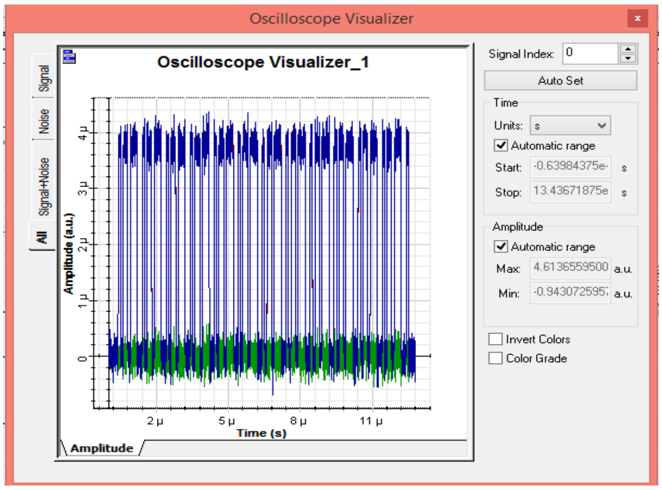

Fig. 9 The PBRS of Fig. 8 in time domain after the PIN photodiode receiver

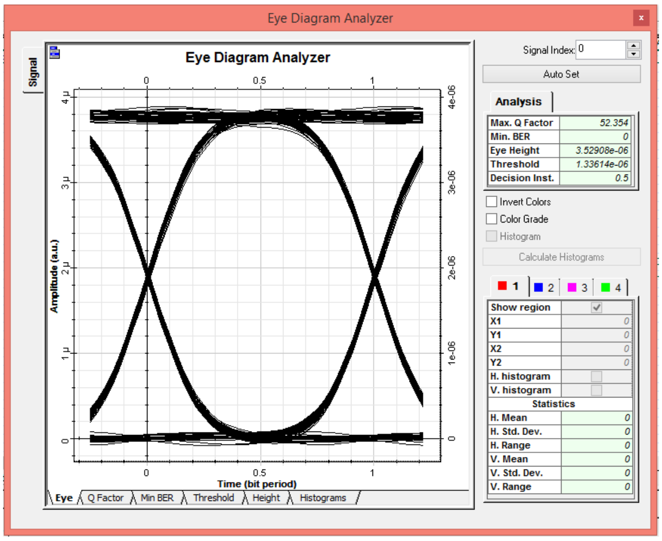

Fig. 10 Eye diagram of the detected PRBS of Fig. 8 after reception

Table 4 UWOC Simulation results at 650 nm for the ten water bodies (10kb/s – 1Mb/s)

Water Body	10 kb/s		100 kb/s		1 Mb/s	
	Q	BER	Q	BER	Q	BER
Ogbese River	341.546	0	333.212	0	326.364	0
Kinira River	342.058	0	334.731	0	292.057	0
Epe River	340.078	0	327.185	0	294.617	0
Ala River	342.796	0	324.474	0	277.686	0
Odo-Oru River	340.96	0	323.34	0	266.794	0
Odo-Eran River	342.158	0	321.479	0	262.932	0
Apake River	340.594	0	314.167	0	266.679	0
Lagos Lagoon (Lekki Phase 1)	341.124	0	313.763	0	232.961	0
Lagos Lagoon (Victoria Island)	339.687	0	262.48	0	143.773	0
Atlantic Ocean	89.745	0	30.742	7.78×10^{-208}	10.282	4.23×10^{-25}

Table 5 UWOC Simulation results at 650 nm for the ten water bodies (10 Mb/s & 1 Gb/s)

Water Body	10 Mb/s		1 Gb/s	
	Q	BER	Q	BER
Ogbese River	189.625	0	32.33	1.33×10^{-229}
Kinira River	172.527	0	24.115	8.57×10^{-129}
Epe River	164.186	0	18.446	2.72×10^{-76}
Ala River	176.746	0	18.263	8.00×10^{-75}
Odo-Oru River	152.512	0	14.928	1.07×10^{-50}
Odo-Eran River	161.209	0	15.365	1.41×10^{-53}
Apake River	134.805	0	14.114	1.55×10^{-45}
Lagos Lagoon (Lekki Phase 1)	92.182	0	9.056	6.71×10^{-20}
Lagos Lagoon (Victoria Island)	52.354	0	5.035	2.37×10^{-7}
Atlantic Ocean	3.055	1.1×10^{-3}	0	1

For each water body, the quality factor of the received data reduces at higher data rates than at lower data rates. Also, the quality factor reduces with an increase in absorbance which depends on salinity. For all the water bodies at 10 kb/s – 10 Mb/s, the BER is zero except for the Atlantic Ocean. At 1 Gb/s, the BER increases with an increase in salinity, and for the Atlantic Ocean at this rate, the quality factor is zero and the BER is 1 indicating no received data. The quality factor and BER suffer more in the ocean and the lagoons than in the rivers due to the relatively higher absorbance of the ocean and the lagoons even at the 650 nm wavelength. It will be difficult to transmit at relatively low power in the Lagos lagoons for a data rate of 1 Gb/s and above, and extremely difficult to transmit at relatively low power in the Atlantic Ocean for a data rate of 10 Mb/s and above.

5 Conclusions

This paper investigated the transmission of visible light (400 nm – 800 nm range) in ten selected water bodies (rivers, lagoons, and the Atlantic Ocean) of Southwest Nigeria via spectroscopy for underwater wireless optical communication. Only attenuation due to absorption was considered. From previous studies, in pure water, blue light (having the least attenuation) is ideal for transmission. However, this study revealed that the absorbance of these water bodies to visible light is wavelength-dependent. It increases at shorter wavelengths (blue-green) than at longer wavelengths (red). The rivers have lower electrical conductivity, salinity, and absorbance compared to the lagoons and the Atlantic Ocean. As the salinity of the water bodies increases, their electrical conductivity increases; and the absorbance is more pronounced on the blue light than the red light. This implies that in the water bodies, blue light is not ideal for optical signal transmission but rather light of longer wavelengths. The study also helped to determine the most suitable wavelength for transmission of visible light signals for underwater optical communication purposes across these selected water bodies of Southwest Nigeria. From the absorbance measurements, an optical beam of a wavelength of 650 nm was found most suitable. Transmission was simulated at this wavelength for the water bodies and their performance was investigated in terms of received quality factor and bit error rate. The results obtained from this work will be useful in setting up UWOC links in these selected water bodies.

Acknowledgment

The authors thank the Department of Electrical and Electronics Engineering, Federal University of Technology Akure, Nigeria for providing some of the facilities for the study.

Conflict of Interest

The authors declare that there is no conflict of interest.

References

[1] Ayeni, A.O., Balogun, I.I. and Soneye, A.S.O., 2011. Seasonal assessment of physico-chemical concentration of polluted urban river: a case of Ala River in Southwestern-Nigeria. *Research Journal of Environmental Sciences*, *5*(1), p.22.

[2] Shen, C., Guo, Y., Oubei, H.M., Ng, T.K., Liu, G., Park, K.H., Ho, K.T., Alouini, M.S. and Ooi, B.S., 2016. 20-meter underwater wireless optical communication link with 1.5 Gbps data rate. *Optics express*, *24*(22), pp.25502-25509.

[3] Gabriel, C., Khalighi, M.A., Bourennane, S., Léon, P. and Rigaud, V., 2012, October. Investigation of suitable modulation techniques for underwater wireless optical communication. In *2012 International Workshop on Optical Wireless Communications (IWOW)* (pp. 1-3). IEEE.

[4] Han, X., Peng, Y., Zhang, Y., Ma, Z. and Wang, J., 2015. Research on the attenuation characteristics of some inorganic salts in seawater. *Journal of the European Optical Society-Rapid publications*, *10*, pp. 15045-1-5.

[5] Pegau, W.S., Gray, D. and Zaneveld, J.R.V., 1997. Absorption and attenuation of visible and near-infrared light in water: dependence on temperature and salinity. *Applied optics*, *36*(24), pp.6035-6046.

[6] Sathyaram, V., Prince, S. and Vedachalam, N., 2018. A study on underwater optical wireless communication link capability in the Bay of Bengal. *Ocean systems engineering*, *8*(1), pp.33-39.

[7] Mogunde, C. and Mosiori, C.O., 2018. Transmittance and Extinction Coefficient of Sea and Well-Water in Mombasa County, Kenya. *Traektoriâ Nauki= Path of Science*, *4*(10), pp.3001-3005.

[8] Shaboy, D., Rockban, D. and Handelman, A., 2018. Tapping underwater wireless optical communication in pure water and natural Dead-Sea ultra-high-salinity water by diffraction grating. *Optics Express*, *26*(23), pp.29700-29711.

[9] Ojediran O.A., Ponnle A.A. and Oyetunji S.A., 2021, October. Attenuation effect of saline water on performance of underwater wireless optical communication within the visible light range, In 2021 *SEET Annual Conference of Federal University of Technology*, Akure, Nigeria, (pp. 472 – 489).

[10] Ojediran, O.A., Ponnle, A.A. and Oyetunji, S.A., 2022. Experimental study on transmission of visible light in table salt water and effect on underwater wireless optical communication. *European Journal of Electrical Engineering and Computer Science*, *6*(2), pp.25-32.

[11] Alatawi, A.S., 2022. A Testbed for Investigating the Effect of Salinity and Turbidity in the Red Sea on White-LED-Based Underwater Wireless Communication. *Applied Sciences*, *12*(18), p.9266.

[12] Adnan, S.A., Hassan, H.A., Alchalaby, A. and Kadhim, A.C., 2021. Experimental study of underwater wireless optical communication from clean water to turbid harbor under various conditions. *International Journal of Design & Nature and Ecodynamics*, *16*(2), pp.219-226.

[13] Akinbile, C.O. and Omoniyi, O., 2018. Quality assessment and classification of Ogbese river using water quality index (WQI) tool. *Sustainable Water Resources Management*, *4*, pp.1023-1030.

[14] Orjiekwe, C.L., Dumo, D.T. and Chinedu, N.B., 2013. Assessment of water quality of Ogbese River in Ovia North-East Local Government area of Edo State, Nigeria. *International Journal of Biological and Chemical Sciences*, *7*(6), pp.2581-2590.

[15] Akagha, S.C., Nwankwo, D.I. and Yin, K., 2020. Dynamics of nutrient and phytoplankton in Epe Lagoon, Nigeria: possible causes and consequences of reoccurring cyanobacterial blooms. *Applied Water Science*, *10*(5), pp.1-16.

[16] Gabriel, C., Khalighi, M.A., Bourennane, S., Léon, P. and Rigaud, V., 2013. Monte-Carlo-based channel characterization for underwater optical communication systems. *Journal of Optical Communications and Networking*, *5*(1), pp.1-12.

[17] Sui, M., Yu, X. and Zhang, F., 2009, February. The evaluation of modulation techniques for underwater wireless optical communications. In *2009 International Conference on Communication Software and Networks* (pp. 138-142). IEEE.

[18] Elamassie, M., Miramirkhani, F. and Uysal, M., 2018, May. Channel modeling and performance characterization of underwater visible light communications. In *2018 IEEE International Conference on Communications Workshops (ICC Workshops)* (pp. 1-5). IEEE.

[19] Jamali, M.V., Khorramshahi, P., Tashakori, A., Chizari, A., Shahsavari, S., AbdollahRamezani, S., Fazelian, M., Bahrani, S. and Salehi, J.A., 2016, May. Statistical distribution of intensity fluctuations for underwater wireless optical channels in the presence of air bubbles. In *2016 Iran Workshop on Communication and Information Theory (IWCIT)* (pp. 1-6). IEEE.

[20] Jasman, F. and Green, R.J., 2013, October. Monte Carlo simulation for underwater optical wireless communications. In *2013 2nd International Workshop on Optical Wireless Communications (IWOW)* (pp. 113-117). IEEE.

[21] Kumar S., Prince S., Aravind J.V., and Kumar S.G., 2019. Analysis on the effect of salinity in underwater wireless optical communication. *Marine Geo-resources and Geo-technology*, *38*(3), pp.1-11.

[22] Atascientific (2020) *Understanding spectrometry and Spectroscopy*, *ATA Scientific*. Available at: https://www.atascientific.com.au/spectrometry/ (Accessed: 29 August 2023).

[23] Al-Azzawi, Z.M., Abdulzahra, N.Z. and Hammood, I.H., 2014. Optical Properties of Tap Water Purity using He-Ne Laser with Different Power Density. *Al-Nahrain Journal of Science*, *17*(3), pp.99-107.

[24] Hu, C., Muller-Karger, F.E. and Zepp, R.G., 2002. Absorbance, absorption coefficient, and apparent quantum yield: A comment on common ambiguity in the use of these optical concepts. *Limnology and Oceanography*, *47*(4), pp.1261-1267.

[25] Stotts, L.B., 2017. Eye diagram and its interpretation. John Wiley and Sons Inc., New Jersey, USA.

[26] Antony, T. and Gumaste, A., 2002. *DWDM network designs and engineering solutions*. Cisco Press, USA.

[27] Anifowose, A.J. and Oyebode, A.W., 2019. Studies on heavy metals contents of Osun River at the pre-urban settlement and across Osogbo City, Nigeria. *Journal of Taibah University for Science*, *13*(1), pp.318-323.

[28] Oketola, A.A., Osibanjo, O., Ejelonu, B.C., Oladimeji, Y.B. and Damazio, O.A., 2006. Water quality assessment of River Ogun around the cattle market of Isheri, Nigeria. *Journal of Applied Sciences*, *6*(3), pp.511-517.

[29] Osagie, E. and Fidelia, A., 2014. Water Quality Assessment of Osse River, Edo State, Nigeria, Using Some Physico-Chemical Parameters. *Nigerian Journal of Life Sciences (ISSN: 2276-7029)*, *4*(1), pp.153-174.

[30] Britannica, T., 2021. Editors of Encyclopedia. Atlantic Ocean. *Encyclopedia Britannica*.

[31] Ponnle, A.A., Ojediran, O.A. and Oyetunji, S.A., 2022. An alternative experimental method for determination of light beam attenuation coefficient in underwater wireless optical communication. *European Journal of Electrical Engineering and Computer Science*, *6*(3), pp.19-26.

[32] Okoli, C.S., Ojo, S.I.A. and Oguntuase, A.M., 2009. Modelling of Sediment Transport Capacities of Ogbese and Owena Rivers in SW Nigeria. *Advanced Materials Research*, *62*, pp.786-796.

[33] Oladeji, O. and Adelowo, F., 2016. The impacts of human activities of Ogbomosho river–causes, effects and role of

an individual (Ogbomosho residents) in prevention of water pollution. *Environmental Science*, *12*(8), pp.1-8.

[34] Olukolajo, S.O. and Hillary, E.C., 2012. Species diversity and growth pattern of the fish fauna of Epe Lagoon, Nigeria. *Journal of Fisheries and Aquatic Science*, *7*(6), pp.392-401.

[35] Travelwaka (2021) *Epe Fish Market – the biggest fish market in Lagos*, *TravelWaka*. Available at: https://www.travelwaka.com/epe-fish-market-the-biggest-fish-market-in-lagos/ (Accessed: 29 August 2023).

[36] Okusipe, O.M., 2003. Lagos Lagoon coastal profile: Information database for planning theory. Department of Urban and Regional Planning, University of Lagos, Lagos, Nigeria.

[37] Aina Adeogun, Professor of Aquatic Toxicology (2020) *How we learnt more about dangerous pollutants in lagos lagoon*, *The Conversation*. Available at: https://theconversation.com/how-we-learnt-more-about-dangerous-pollutants-in-lagos-lagoon-139987 (Accessed: 29 August 2020).

[38] Abuta, C.M.-A. (2018) *The Atlantic Ocean as a nigerian trade route*, *Make Heritage Fun!* Available at: http://www.makeheritagefun.com/atlantic-ocean-nigerian/?amp=1 (Accessed: 29 August 2023).

[39] Tata, H., Nzelibe, I.O., and Faneye, A.J., 2019. Bathymetric mapping for safe navigation: A case study of part of Lagos Lagoon. *Afr. Sch. J. Environ. Des. Constr. Mgt.(AJECM)*, *14*, pp.1-13.

[40] (No date a) *Elegushi beach, postal code, GPS coordinates, Lekki, Lagos 550104 Nigeria - tripexpress.com*. Available at: https://www.tripexpress.org/attraction-elegushi-beach-10081994/ (Accessed: 29 August 2023)

SciEn
Journal of Engineering Advancements Vol. 04(03) 2023, pp 90-100 https://doi.org/10.38032/jea.2023.03.005

A Micro Energy Grid Optimal Design and Economic Operation Using Genetic Algorithms

Ahmed S. Eldessouky [1,*] *and Abbdallah Fahmy* [2]

[1]Faculty of Energy and Environment Engineering, BUE, Cairo, Egypt
[2]Canadian International College, Cairo, Egypt

Received: May 07, 2023, Revised: August 27, 2023, Accepted: August 27, 2023, Available Online: September 29, 2023

ABSTRACT

This paper presents an optimal design procedure and economic operational scheduling of micro energy grids (MEGs). The optimization objectives are to minimize cost, carbon dioxide emissions, and energy deficiency. The energy sources and conversion technologies included in this study are renewable-based sources (wind and photovoltaic), a furnace, an electrical heater, a main power grid, and a local power station. Two proposed control levels are applied to control the operation of the MEG. The supervisor control level selects the energy supplier based on price and/or availability. The inner control level dynamically matches the demand profile with the supply profile. The control loops guarantee dynamic matching between the demand profile and supply profile. Two scenarios are simulated, zero interest rates and 5.25% interest rates. The results showed renewables contribute with a significant share as an energy source, however, higher interest rates would negatively impact this contribution. It also confirms that carbon taxes can reduce the use of fossil fuels as an energy source.

Keywords: Micro Energy Grid, Energy Grid Operation, Optimal Structure of Energy Grid, Genetic Algorithms, Renewable Energy Sources

1 Introduction

In 2019, global energy demand increased by 8.4%. However, due to renewable energy contributing to 29% of total demand growth, greenhouse gas emissions increased only by 1.4% [1]. In the previous 5 years, the greenhouse gas emissions were kept unchanged while the energy demand had increased by a rate of 1.4% [2]. This is due to the significant penetration of renewable-based energy in energy production that reduces greenhouse gas emissions caused by energy production.

A Micro Energy Grid (MEG) can integrate renewable energy sources (RESs) and distributed generators (DGs) in an energy system that satisfies the energy demand in local geographical areas [3]. MEG facilitates better control of energy production and emission, reduces power outage risk, and increases energy reliability [4]. They can utilize local energy resources with a lower dependency on centralized power plants based on their operational mode (islanded or grid-connected). Hence, power transmission loss and transmission infrastructure can be greatly reduced. The term Micro Energy Grid (MEG) was recorded in some articles to replace MG with the same definition. However, some articles use this term (MEG), with the addition of "Energy" to indicate the integration of other forms of energy rather than electricity, such as heat and gas [5],[6]. The integration of other forms of energy provides more effective and optimal solutions with the presence of more supply options. Combined heat and power (CHP) generators with heat generation are examples of supplying energy in other forms rather than electricity. Utilizing wasted energy from such resources increases their efficiency and reduces energy costs and emissions. In this paper, MEG is used to refer to the integration of different forms of energy. MEGs offer many benefits such as

1) Ability to supply growing demand with minimal modification to energy transmission infrastructure of the main grid.
2) Reduce energy loss due to energy transmission.
3) Allow local management of energy demand by load shedding/scheduling.
4) Minimize the risk of a power outage with the presence of different supply resources.
5) Reduce emissions by integrating renewables as a source of energy.
6) Deploy, maintain, and operate energy generators in an efficient manner.
7) Supply isolated areas with required energy using available local energy sources.

MEG planning and operational scheduling is a multi-objective optimization problem where size, structure, and interconnection are among different parameters affecting the optimization objectives (cost and reliability). While some research activities show interest in optimizing MEG locally [6], others focused on the interconnection options with other MEGs and the main utility network [7]-[9], reducing the operation cost by load shifting [10], or scheduling of energy storage systems [11],[12]. The mentioned work used AI algorithms in their optimization processes such as genetic algorithms [10]-[11] and fuzzy logic [12].

Moghaddam et al. [13] introduced MG optimization with local optimization objectives (ignoring the transformer losses). They applied the modified particle swarm optimization technique with adaptation capabilities to reduce optimization dependency on learning factors and momentum weight factors in conventional PSO. They adopted a time of 24 hours for the optimization process, as the algorithm is an online power

*Corresponding Author Email Address: Ahmed.eldessouky@bue.edu.eg

dispatch process. Sizes of DGs are assumed constant, hence, no optimization for the sizes of DGs greatly affects the initial cost.

Díaz et al. [14] developed an optimal energy policy for MG in a grid-connected mode under uncertainty. They considered wind turbines (WT) and gas microturbines as hybrid power systems, in addition to the main grid. Levelized Cost of Energy (LCoE) is used as an objective function for connection policy. The operation expenditures, gas, and electricity prices (OPEX), together with capital expenditures (CAPEX), are used to find the optimal policy for switching between gas microturbine and main grid to compensate for energy deficiencies between demand and WT generation. Their work considers the uncertainty of prices, not energy availability. The CAPEX for grid connectivity was not included. The authors developed the Ornstein-Uhlenbeck (OU) process, which satisfies the stochastic differential equation model to present the uncertainty of both price and load. Another work on optimal energy management under uncertainty can be found in [15]. Katzenbach et al. [8] developed a methodology for energy conservation and resource management in building systems. Their work focused on listing sequential procedures to examine the effectiveness of different energy options. Kouloura et al. [16] presented a methodology for decomposing energy problems for buildings into multi-energy systems in different forms (hyper, parallel, and sub-systems). The methodology allows us to observe the coupling of energy processes in buildings, based on the system analyses of student housing buildings in the city of Xanthi, Greece, as a case study. They proposed a set of interventions to improve energy consumption, cost, and emission. No optimization algorithm is used, and only human knowledge and experience are used for energy optimization measures and evaluation. Zidan et al. [17] presented optimal deployment of distributed generation (DG) based on capacity sizes and types. They assume a static model of energy generators and storage. Hence, only open-loop control was used in their algorithm.

In this paper, an optimal structure and economic operation of MEG is performed. The MEG operation and scheduling are performed by applying two control levels. The upper control level (supervise controller) provides optimal operation of MEG, based on fuel prices and availability, to satisfy the load demand. While energy prices can be easily achievable, the availability of energy from each source is not. In the previous work, the operation and optimization algorithms assume unlimited energy sources, neglecting the limited structure of MEG. In addition, they either neglect the losses of energy generators and converters or consider them as static losses. Hence, their work lacks practicality.

This paper provides a significant contribution by accounting for limited energy sources, and the dynamics of power loss of each component in the MEG. As the losses of different components of MEG are dependent on the load value, they can't be presented as static values. Hence, a lower-level dynamic control process (PI algorithm) was adopted to satisfy dynamic heat and power load in the presence of dynamic losses of energy conversion technologies, and power limitation of those sources. Once the lower control level signals no availability to supply the required power from a selected source, the upper control level shifts demand to the second lower-cost power source. Moreover, the paper accounts for the presence of local power stations that can export surplus energy with prices lower than the prices of the main grid.

With the implementation of two-level control loops to MEG under consideration, an optimal operation is guaranteed; however, it doesn't guarantee its optimal structure. Therefore, genetic algorithms (GA) are implemented to find the optimal structure of the MEG under its optimal operating conditions. Annual capital expenditure, maintenance, operation (M&O) expenditure, emission, and energy deficiency are used to form objective functions for the optimization process. The MEG is designed to supply a small-sized town of 200 midsize houses, located near urban Toronto, Ontario Canada (Heat and power loads).

The paper is organized as follows: Section 2 describes the MEG structure. Each energy source model is presented in the subsections of Section 2. The models included the economic model (annual capital expenses and operation expenditure), the generation model for renewable sources, and the losses model for other energy sources. Section 3 discusses the control algorithm. Section 4 introduces the optimization algorithm. Section 5 presents the simulation process and discusses the results. Finally, the conclusion is presented in Section 6.

2 MEG structure

The proposed MEG structure is shown in Fig. 1. It is composed of renewable sources (wind turbine and PV array), a gas furnace, an electrical heater, and a step-down transformer. The structure assumes direct supply from private/local stations, with the same operating voltage levels of the load (no transformer is required). The MEG is connected to the main grid via a step–down transformer for importing/exporting power from/to the grid. Its model presentation in the simulation is essential for cost and power loss calculations.

It is assumed that heat generation from the furnace is dependent only on furnace capacity and required heat energy. The gas supply to the furnace is assumed to be unlimited. The system is composed of two coupled control loops, one for the power and one for the heat. The required power is satisfied, first, by the renewables. If renewables don't satisfy the required power, a controller requests additional power from the main grid or the private local station, based on price and availability. If renewables produce power greater than required, the heat controller will direct surplus power to satisfy the required heat. If surplus power doesn't satisfy the required heat, the heat controller satisfies the missing heat either from the furnace or from the electrical heater, according to the price and capacity of the furnace and electrical heater. Any surplus energy from renewables, after satisfaction of power and heat requirements, will be exported to the main grid via the utility transformer.

Fig. 2 shows the structure of the two-level control system applied to the MEG. The supervisor controller represents the upper control level at which it determines the required power that should be supplied from each source. The amount of required power from each source is determined based on price and availability. The availability is a feedback signal generated by the source model. This signal is dynamically changed according to current power generation, power losses, and the source capacity (green dashed line in Fig. 2).

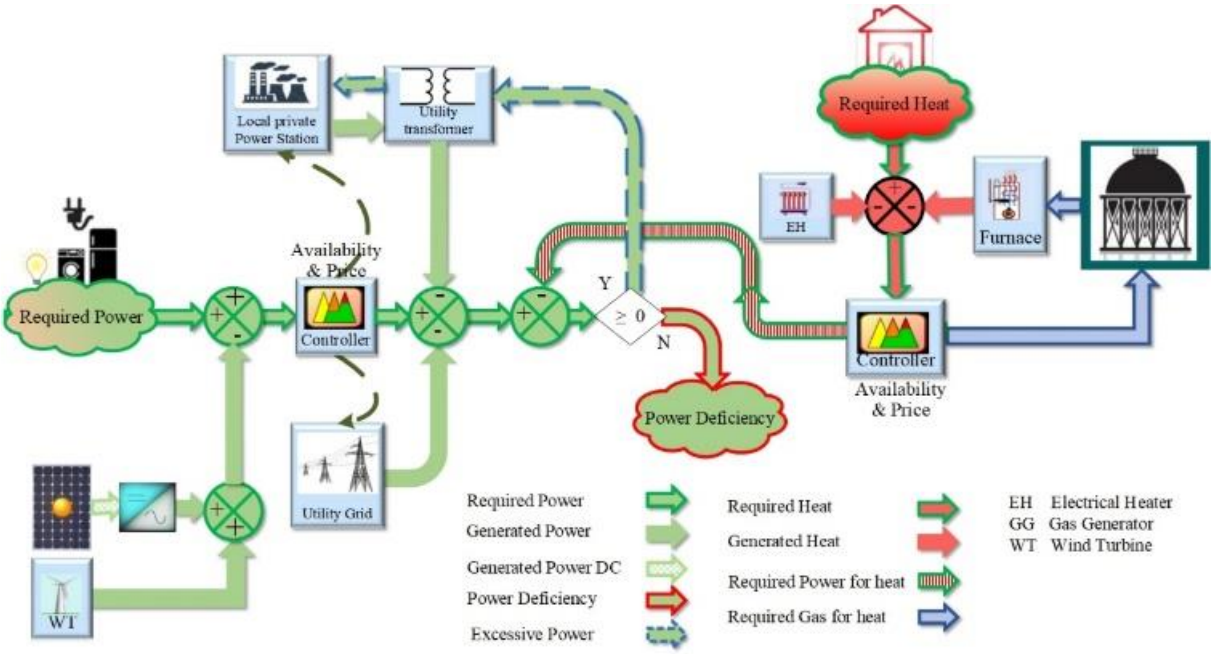

Fig. 1 The proposed MEG structure

The lower control level is a PID algorithm applied for each energy source. It ensures that the source produces the required amount of power, provided that the limits of the source, according to its capacity, were not reached. If the generated power and power loss reach the limits of source capacity, the model signals zero availability to the supervisor controller to shift demand to the next available sources.

The following subsections describe the economic and power models of each energy source.

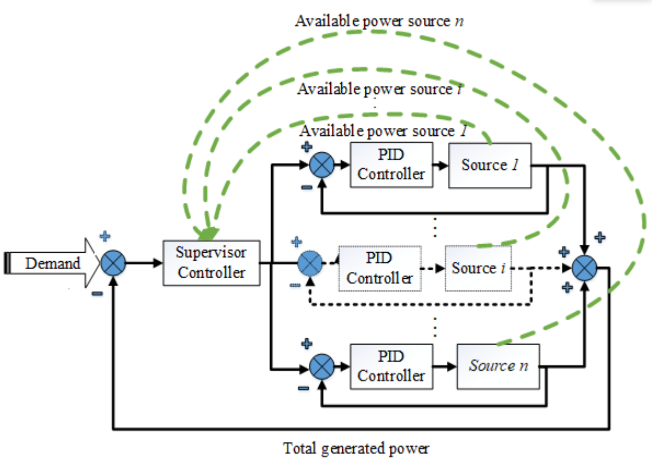

Fig. 2 Two-level Control MEG

2.1 Wind turbine model

Wind turbines (WTs) are among the renewable technologies that have a high penetration rate in MEGs. The global wind power capacity increased from 48,000 MW in 2004 to 370,000 MW in 2014 with a growth rate of 16% in 2014 [2]. In 2019, the total world generation of wind energy increased to 651 GW [1]. Annual wind capacity additions declined by 21% from 2021 to 2022 due to delayed wind projects in China caused by Covid-related restrictions. However, it is expected to rebound by 70% addition in 2023 [18], Due to the limited production time of PV systems (during daytime only), WTs provide an alternative renewable source that can produce power independent of the time of day, but rather depending on the wind power availability at a given time. The wind power (P_{wind} (kW)) at a given wind speed (v (m/s)) can be determined as follows:

$$P_{\text{wind}} = {}^{1}\!/_{2}\, \rho R v^{3} / 1000\ kW \tag{1}$$

where is the air density (nearly 1.225 kg/m^2 $at\ sea\ level$) and R is the radius of the wind rotor. The relation between wind power and wind turbine output power is given by:

$$P_{\text{WT}} = P_{\text{wind}} \times \left(\frac{16}{27}\right) \times C_P \tag{2}$$

Where 16/27 is the Betz limit and C_P is the Turbine capacity. Turbine efficiency was set to 30 % [4] hence, at a wind velocity of 14 m/s, the wind turbine can generate a peak power of 504 W/m^2.

Besides its capital cost and size, the wind power curve is the main characteristic of WT that plays a major role in its selection. A linearized wind power curve is used in this study as shown in Fig. 3 [4].

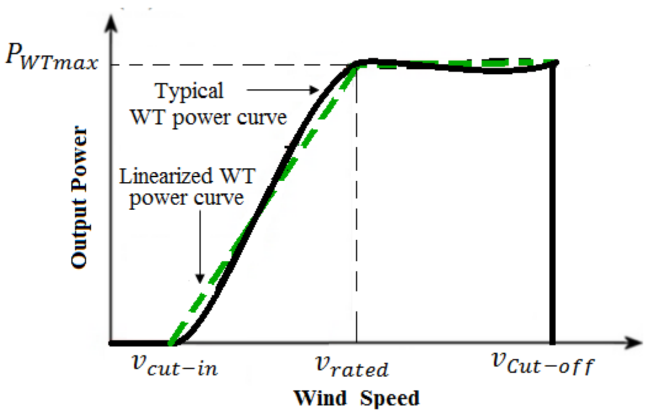

Fig. 3 Typical and linearized wind turbine output power with wind speed curve

According to the trend shown in Fig. 3, the output power of wind turbine is given by [19]:

$$P_{WT}(k) = \begin{cases} 0 & v(k) < v_{in} \\ \dfrac{P_{WTr}}{v_r - v_{in}} \times (v(k) - v_{in}) & v_{in} \le v(k) \le v_r \\ P_{WTr} & v_r \le v(k) \le v_{off} \\ 0 & v(k) > v_{off} \end{cases} \quad kW \tag{3}$$

Where $P_{WT}(k)$ is the generated power of the WT at wind speed $v(k)$, v_{in} is the cut-in wind speed, v_r is the wind speed at which WT generate power at its rated power (P_{WTr}), and v_{off} is the wind speed at which the WT braking system is activated to avoid WT mechanical failure. Further details on the dynamic model of the wind turbine can be found in [7].

The annual generated energy by WT is given by:

$$E_{WT} = \sum_{k=1}^{8760} P_{WT}(k) \quad kWh \tag{4}$$

The capital cost of different-sized WT is given in Table 1.

Table 1 Wind turbine cost base on size [1],[20].

Size	Cost ($/kW)
1kW turbine	10,000
5kW turbine	5,000
250kW turbine	3,500 -2,500

The capital cost of WT can be calculated as follows:

$$C_{CaWT} = \alpha_{WT} \times P_{WTnom} \tag{5}$$

where α_{WT} is the cost of WT per kW, and P_{WTnom} is the nominal power of installed WT. α_{WT} can be calculated as follows:

$$\alpha_{WT} = \begin{cases} \alpha_{WT_1} & P_1 \ge P_{WTnom} \\ \vdots & \vdots \\ \alpha_{WT_i} & P_i \lesssim P_{WTnom} \lesssim P_{i+1} \\ \vdots & \vdots \\ \alpha_{WT_N} & P_N \lesssim P_{WTnom} \end{cases} \tag{6}$$

where α_{WT_i} represents the cost of WT per kW for WT sizes between P_i and P_{i+1}. The annual capital expenses can be calculated as follows:

$$C_{CaWT\_an} = C_{CaWT}/T_{WT} \tag{7}$$

where T_{WT} is the WT lifetime (years). WT operation expenditure is calculated as follows:

$$OpEx_{\mathrm{WT}} = \mathrm{FCR} \times (C_{CaWT}/T_{WT}) + C_{OMWT}E_{WT} \quad \$/year \tag{8}$$

where C_{CaWT} is the WT initial cost ($), FCR is the fixed charge rate (interest, insurance, taxes, and others), C_{OMWT} is the WT operation and maintenance cost (O&M) ($/kWh) and E_{WT} is the produced energy (kWh/year)[20],[21]. The first term of Eq. (7) is independent of the WT energy production (insurance, annual interest rate, land leasing, etc.), while the second term is dependent on the WT energy production (parts replacements, production maintenance, etc.). Eq. (7) can be rewritten as follows:

$$OpEx_{\mathrm{WT}} = \mathrm{FCR}(C_{CaWT}/T_{WT}) + C_{OM} \sum_{k=1}^{8760} P_{WT}(k) \quad \$/year \tag{9}$$

2.2 Solar PV Model

PV represents one of the major renewable energies that achieved significant growth. According to the Solar Energy Industry Association (AEIS) report [22], about 50% of newly electricity-generating capacity added to the US grid in 2022 comes from solar stations. For the fourth year in a row, PV technology came at the top technology for new additions. The PV market grew by more than 95% in the USA. The renewables account for generating +315 GW in 2022, 50% comes from PV [23]. The rapid increase in PV installation is due to the massive production of PV modules from China which produced about 61% of global production in 2016 (about 45000 MW annually). Such a production rate reduced the module cost from $0.65/W in 2015 to $0.39/W in 2016 [22]. The prices were reduced in 2020 to $0.23/W for monocrystalline modules [24]. The selection of PV systems is critical where capital expenditure represents from 75% to 90% of the life cycle cost (the O&M contributes only 10% to 25%) [25].

The output power of the PV module ($P_{PVm}(k)$), at any sample time k, is dependent on ambient irradiance ($P_{irr}(k)$ (kW/m^2)), panel temperature (T), PV area (a_{module}) and PV module efficiency (μ_{PV}) as follows:

$$P_{PVm}(k) = \begin{cases} P_{irr}(k) \times a_{module} \times \mu_{PV} \times D \times \mu_t & P_{irr}(k) \times \mu_{PV} \times a_{module} < P_{PVnom} \\ P_{PVnom} \times \mu_t \times D & P_{irr}(k) \times \mu_{PV} \times a_{module} \ge P_{PVnom} \end{cases} \tag{10}$$

where P_{PVnom} is the nominal power of the PV module under standard test conditions, D is the annual degradation rate of solar panels, and μ_t is the temperature efficiency factor which can be calculated using the following equation:

$$\mu_t = 1 - [\Upsilon \times (T - T_{STC})] \tag{11}$$

where T_{STC} is the Standard Test Conditions temperature, and Υ is the power temperature coefficient (typically 0.005 for crystalline silicon) [9],[26].

The module efficiency (μ_{PV}) can be calculated using the following formula:

$$\mu_{PV} = \frac{P_{PVnom}}{P_{irrSTC}} \tag{12}$$

where P_{irrSTC} is the irradiance under standard test conditions (1000 W/m^2).

Hence the total generated power of an N_{PV} installed PV module is given by:

$$P_{PV}(k) = P_{PVm}(k) \times N_{PV} \tag{13}$$

The annual generated energy using PV is given by:

$$E_{PV} = \sum_{k=1}^{8760} P_{PV}(k) \quad kWh \tag{14}$$

PV systems are composed of PV modules, inverters, wiring, and other hardware components. The rate of change of prices of PV system components differs. While the price of PV panels changes dramatically, the prices of inverters and other hardware do not. In addition to the components of a PV system, the installation cost is another major parameter in the determination of the capital cost of a PV system. The capital cost of the PV system can be calculated as follows:

$$C_{CaPV} = (C_{mod} + C_{inv} + C_{BOS} + C_{ins}) \times P_{PVnom} \tag{15}$$

where C_{mod} is the module cost, C_{inv} is the inverter cost, C_{BOS} is wiring and other hardware costs (Balance of System) and C_{ins} are the installation expenses per kW rating power of the generator. The annual capital expenses can be calculated as follows:

$$C_{CaPV\_an} = C_{CaPV}/T_{PV} \quad (16)$$

where T_{PV} is the PV lifetime.

The O&M (operational and maintenance) expenditure

$$OpEx_{\text{PV}} = \text{FCR} \times (C_{CaPV}/T_{PV}) + C_{OMPV}E_{PV} \quad \$/year \quad (17)$$

Where C_{CaPV} is PV initial cost (\$), C_{OMPV} is the PV operation and maintenance cost (O&M) (\$/kWh), and E_{PV} is the produced energy (kWh/year). Eq. (17) can be rewritten as follows:

$$OpEx_{\text{PV}} = \text{FCR} \times (C_{CaPV}/T_{PV}) + C_{OMPV} \sum_{k=1}^{8760} P_{PV}(k) \quad \$/year \quad (18)$$

Table 2 shows the PV data used for the simulation.

Table 2 PV data [24], [27].

Item	Value
PV efficiency	16%
Degradation	0.4%
PV lifetime	20 years
Module price	0.35 $/W
Inverter price	13 $/Wac
Inverter lifetime	10 years
BOS (Structural and Electrical)	0.4 $/W

2.3 Furnace Model

As a result of low gas prices compared to any other source of energy, furnaces are the first option to produce heat energy. However, the cost of each ton of emission produced by fossil fuel and restrictions by international protocols and agreements concerning the environment may flip the equation in favor of environmentally friendly energy sources. Despite the effort to reduce fossil fuel consumption, they represent a competitive energy source for heat and transportation applications due to low prices and high energy density. In the case study of this paper, in addition to the electrical heater, the furnace is used to satisfy the MEG heat demand.

The capital cost of the furnace (C_{CaFur}) is given by:

$$C_{CaFur} = \alpha_{Fur} \times P_{Furnom} \quad (19)$$

where α_{Fur} is the cost of the furnace per 1kBUT/hr and P_{Furnom} is the nominal power of the installed furnace. α_{Fur} can be calculated as follows:

$$\alpha_{Fur} = \begin{cases} \alpha_{Fur_1} & P_1 \geq P_{Furnom} \\ \vdots & \vdots \\ \alpha_{Fur_i} & P_i \lesssim P_{Furnom} \lesssim P_{i+1} \\ \vdots & \vdots \\ \alpha_{Fur_N} & P_N \lesssim P_{Furnom} \end{cases} \quad (20)$$

where α_{Fur_i} represents furnace initial and installation costs per 1kBUT/hr of furnace size between P_i and P_{i+1}. The annual capital expenses can be calculated as follows:

$$C_{CaFur\_an} = C_{CaFur}/T_{Fur} \quad (21)$$

where T_{Fur} is the Furnace lifetime (years).

Furnace operation expenditure is calculated as follows:

$$\begin{aligned} OpEx_{\text{Fur}} = {} & \text{FCR} \times (C_{CaFur}/T_{WT}) + C_{fuel} \\ & \times C_P \times \sum_{k=1}^{8760} P_{Fur}(k) \times \frac{100}{\mu_{Fur}} + C_{MFur} \\ & \times \sum_{k=1}^{8760} P_{Fur}(k) \quad \$/year \end{aligned} \quad (22)$$

where C_{MFur} is the furnace maintenance cost (\$/kWh), C_P is the Specific energy (MJ/kg), C_{fuel} is the fuel price (\$/kg) and μ_{Fur} is the furnace efficiency. The CO_2 emission (kg/ year) is calculated by:

$$m_{co2} = EF_{co2} \times \sum_{k=1}^{8760} P_{Fur}(k) \times \frac{100}{\mu_{Fur}} \quad (23)$$

where EF_{co2} is the CO_2 emission factor.

The furnace requires electrical power $P_{eleFur}(k)$ for its operation is given by:

$$P_{eleFur}(k) = \beta_{eleFur} \times P_{Fur}(k) \quad (24)$$

where $P_{Fur}(k)$ is the current heat rate of the furnace, β_{eleFur} is the electrical coefficient of the furnace dependent on furnace type as given in Table 3 [28].

Table 3 Electrical coefficient for different furnace types

Furnace type	β_{eleFur}
Non-Condensing Furnace	0.000006 kW/Btu/h
Condensing furnace with PSC motor	0.000009 kW/Btu/h
Condensing furnace with BPM motor	0.000005 kW/Btu/h

2.4 Electrical Heater and Transformer Model

A simplified Electrical heater model is used for the simulation. The efficiency of the electrical heater is set to 100% and the capital cost is given by the following equation:

$$C_{CaeleF} = \alpha_{eleF} \times P_{eleFnom} \quad (25)$$

where α_{eleF} is the average capital cost per 1 kBtu/h (set to \$35) including the unit price and installation cost. The annual capital expenses can be calculated as follows:

$$C_{CaeleF\_an} = C_{CaeleF}/T_{eleF} \quad (26)$$

where T_{eleF} is the electric furnace lifetime (years).

The transformer capital cost ($C_{CaTrans}$) is given by:

$$C_{CaT} = \alpha_T \times P_{Tnom} \quad (27)$$

where α_{Trans} is the cost of the transformer per 1kWh and $P_{Transnom}$ is the nominal power of installed Transformer. α_{Trans} can be calculated as follows:

$$\alpha_T = \begin{cases} \alpha_{T_1} & P_1 \geq P_{Tnom} \\ \vdots & \vdots \\ \alpha_{T_i} & P_i \lesssim P_{Tnom} \lesssim P_{i+1} \\ \vdots & \vdots \\ \alpha_{T_N} & P_N \lesssim P_{Tnom} \end{cases} \quad (28)$$

where α_{T_i} represents the initial and installation costs of the furnace per 1 kWh of transformer size between P_i and P_{i+1}. The annual capital expenses can be calculated as follows:

$$C_{CaT\_an} = C_{CaT}/T_T \quad (29)$$

where T_T is the transformer lifetime (years). The transformer losses are given by:

$$P_{T_{loss}}(k) = \mu_T P_L(k) \tag{30}$$

where μ_T is the transformer efficiency and $P_L(k)$ is the load power at instance k.

3 Control Algorithm

The control flowchart is shown in Fig. 4. The heat and power control algorithms are identical. The algorithms start by sorting the energy sources based on their operational costs (namely the fuel prices, hence, renewable sources costs are negligible during the sorting process). Then, the algorithms request a supply for the current demand (heat or power) from a source with a lower operational cost.

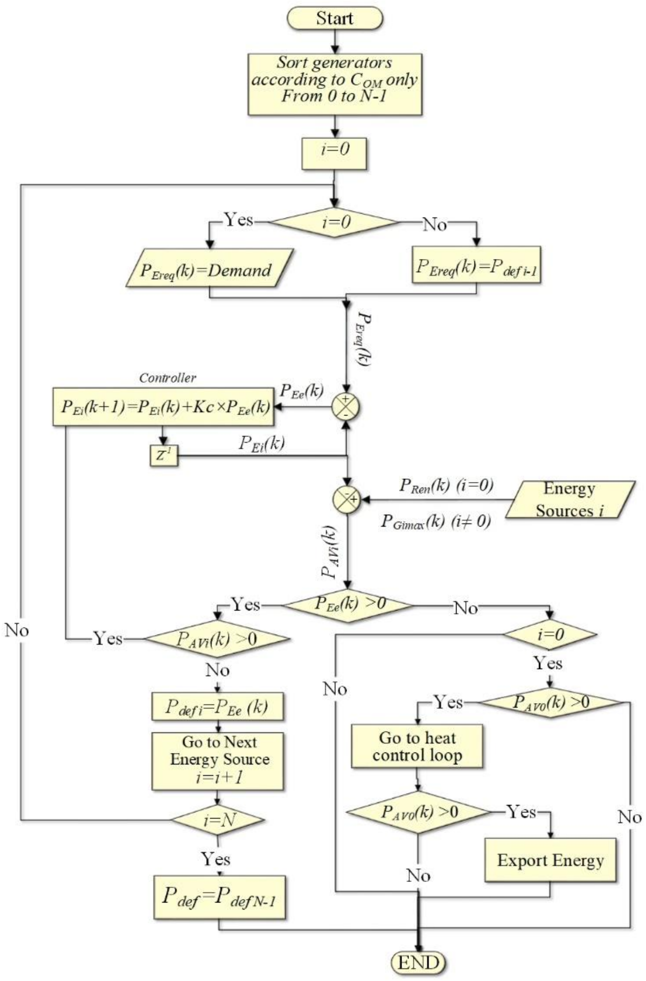

Fig. 4 Control flowchart

The control loop increments the control action dynamically to match the required demand and simultaneously calculate the available power based on both generated power and source capacity according to the following equations:

$$P_{Ee}(k) = P_{Ereq}(k) - P_{Ei}(k) \tag{31}$$

$$P_{Ei}(k+1) = \begin{cases} P_{Gimax} & P_{Ei}(k+1) \geq P_{Gimax} \\ P_{Ei}(k) + K_c \times P_{Ee}(k) & 0 \leq P_{Ei}(k+1) \leq P_{Gimax} \\ 0 & P_{Ei}(k+1) \leq 0 \end{cases} \tag{32}$$

where $P_{Ereq}(k)$ is the required electrical power at instant k, $P_{Ee}(k)$ is the error between currently required power and the delivered power to the load $P_{Ei}(k)$, and P_{Gimax} is the capacity of the generator i. For renewable sources, the equation will be slightly modified to the following:

$$P_{Ei}(k+1) = \begin{cases} P_{Ren}(k) & P_{Ei}(k+1) \geq P_{Ren}(k) \\ P_{Ei}(k) + K_c \times P_{Ee}(k) & 0 \leq P_{Ei}(k+1) \leq P_{Ren}(k) \\ 0 & P_{Ei}(k+1) \leq 0 \end{cases} \tag{33}$$

where $P_{Ren}(k)$ is the generated power from renewables at instant k. If the generated power reaches the capacity limit of the source, the algorithms shift to the next energy source with the next lower operational cost. The process repeats till the load is satisfied or the generated power reaches the full capacity of all generators. The total power deficiency (P_{def}) represents the unfulfilled demand from all given sources.

4 MEG Optimization using Genetic Algorithms

Unlike conventional optimization techniques, GA is a search algorithm that can guarantee a global minimum. Each parameter of the optimization problem is coded in what is called a "Gene". The collection of genes (optimization parameters) forms a chromosome. Individuals in GA are presented by the different settings of the value of the gene and hence the chromosome. Accordingly, everyone is a potential solution. A population of a random set of individuals forms the first generation. The fitness function is a tool to measure how efficient everyone is to be a candidate solution to the problem. According to their fitness, individuals are selected for crossover. Parents and offspring, resulting from the crossover, are used to form the next generation. The process repeats till a significant level of fitness is achieved or the number of generations reaches a predefined value. To avoid getting stuck in the local minimum, a mutation is added to the process. The mutation is the process by which a very low percentage of the genes are exposed to random change. The mutation process forces the search algorithm to skip from the current solution pool to the unexplored area in the search domain. The percentage of crossover and mutation affect the speed of the search process.

The optimization process is performed through two phases. In the first phase, the optimal structure of the supply system is achieved by considering annual capital expenditure, maintenance, and operation (M&O) expenditure, and energy deficiency to form the cost function. The parameters of MEG that are subjected to the optimization process are the sizes of each generator in addition to the required inverters and transformers to connect to loads, grid, and local power station. Hence, the chromosome of everyone is given by:

$$x = [P_{WTnom} \quad P_{PVnom} \quad P_{TRnom} \quad P_{Furnom} \quad P_{eleFurnom}] \tag{34}$$

The fitness function is reciprocal to the cost function as follows:

$$f = \frac{1}{1 + C_I} \tag{35}$$

where C_I is the cost function and is given by:

$$C_I = \eta_1 C_{PPkWh} + \eta_2 C_{E_{def}} \tag{36}$$

where η_1 and η_2 are coefficients representing the significance of each term to the optimization process, C_{PPkWh} is the average price per kWh of electrical or heat energy and is given by:

$$C_{PPkWh} = \frac{C_t}{E_{Dem} - E_{def}} \tag{37}$$

$$E_{Dem} = \sum_{k=1}^{8760} P_e(k) + \sum_{k=1}^{8760} P_h(k) \tag{38}$$

$$C_t = \sum_{\mathrm{i=1}}^{\mathrm{N}} \left(C_{Ca_{an}i} + OpEx_{\mathrm{i}}\right) + \frac{m_{co2}}{1000} \times C_{CO2} - C_{sell} \sum_{k=1}^{8760} P_{sell}(k)$$

where E_{Dem} is the yearly energy demand, $P_{sell}(k)$ is the sold power at instant k and C_{sell} is the selling price in \$ US per kWh, m_{co2} is the emitted CO_2 kg/year, and C_{CO2} is the cost of CO_2 and set to \$37 per ton [29].

$C_{E_{def}}$ represents the normalized energy deficiency of electrical and heat energy demand in one year and given by:

$$C_{E_{def}} = \frac{E_{def}}{E_{Dem}} \tag{39}$$

$$E_{def} = \begin{cases} E_{Dem} + \sum_{k=1}^{8760} \left(\sum_{\mathrm{i=1}}^{\mathrm{M}} P_{Loss}(i,k) - \sum_{\mathrm{i=1}}^{\mathrm{N}} P_g(i,k) \right) & if > 0 \\ zero\ other\ wise \end{cases} \tag{40}$$

where $P_g(i,k)$ is the generated power from generator i, $P_{Loss}(i,k)$ is the power loss of energy element i in MG at instance k, E_{Dem} is the electrical and heat energy demand in one year and $P_e(k)$, and $P_h(k)$ is the power and heat demand at instance k respectively.

5 Simulation and Results

One-year profiles of heat and power loads for midsize houses [30] are used for the simulation. Those profiles were scaled to fit 200 midsize houses located near the urban Toronto area. The irradiance, temperature, and wind speed profiles at the same location are applied [31].

The GA optimization was performed over eight generations each generation is 60 individuals. Each individual represents a potential solution of the size of all generators and energy conversion technologies used in this simulation. The crossover probability was set to 80% while the mutation was set to 5%. The optimization was conducted for two scenarios, the interest rate in the first scenario was set to zero% while it was set to 5.25% for the second scenario.

5.1 Scenario I

In this scenario, the interest rate was set to zero. Fig. 5 shows the optimization results of the first scenario. As can be noted from Fig. 5(a) the maximum fitness was converged to a solution and was close to 7. Fig. 5(b) shows the progress of KPIs (key performance indices) of the best individual (the terms of the cost function of the optimization) vs. the generations. It confirms the stability optimization process, and that the optimization was almost settled after the sixth generation. Table 4 shows the detailed progress of the optimization by the generations. The first four columns represent the parameters that are subjected to optimization (the sizes of the energy generators), the next four columns represent the terms of the cost function, and the last column represent the fitness value of this individual. The table shows how the optimization algorithm reduces the use of gas over generations due to high emission costs. The price of energy is about 11.4 ₵/kWh in addition to the emission price that should be added (0.1 ₵/kWh), the power deficiency is about 2% and the excessive power is close to zero. The results of the best individual over a generation are listed in Table 4.

Table 4 Results of optimization over generations (first scenario interest rate = 0.0%)

Generation	WT (kW)	PV (kW)	Transformer (MW)	Furnace (kW)	Price (\$/kW)	Emission Cost (\$/kW)	E_def ratio	E_excess ratio	Fitness
1	6032	3692	5	21564	0.194	0.097	0.020	0.009	3.120
2	572	3691	5	21564	0.110	0.086	0.020	0.000	4.625
3	270	3217	6	1105	0.099	0.044	0.020	0.000	6.145
4	1900	3216	6	6	0.140	0.000	0.021	0.000	6.211
5	270	3832	4	970	0.105	0.038	0.021	0.000	6.096
6	270	3831	7	35	0.122	0.001	0.021	0.000	6.943
7	170	3216	6	27	0.116	0.001	0.021	0.000	7.262
8	100	3216	6	26	0.114	0.001	0.021	0.000	7.345

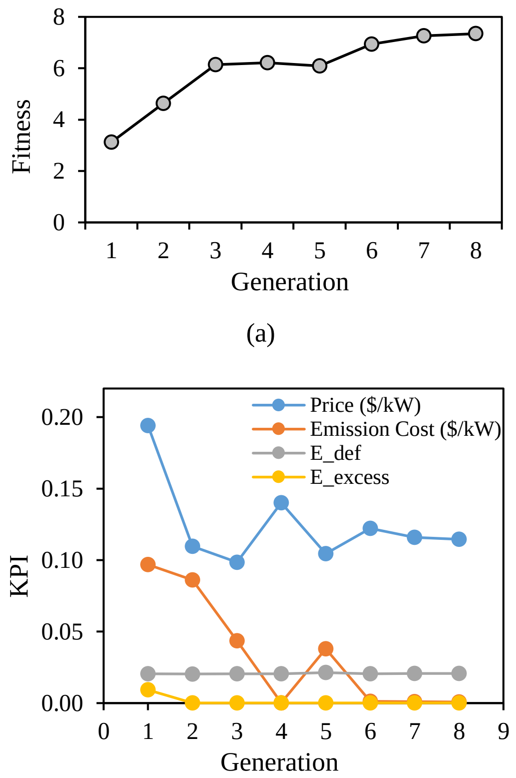

(a)

(b)

Fig. 5 Optimization results for 1st scenario (a) Fitness VS generations (b) KPIs of best individual vs. generation

Fig. 6 shows the energy consumption from different sources vs. time for the optimized structure of the MEG. It also indicates exported and sold energy from renewables to the grid.

Fig. 7 shows the load contribution percentage from different energy sources of optimized MEG for (a) total load (heat and power), (b) heat load, and (c) power load. It shows that around 61% of the supply is satisfied using reliable sources (grid). It also shows that renewables contribution with significant share in total energy required for heat and power loads (20%). Most of the renewable energy go to power load. The renewable sources contribution for heat and power loads is 7% in addition to 14% exported energy to the grid (the percentage of exported energy is calculated based on the total required energy not the generated one).

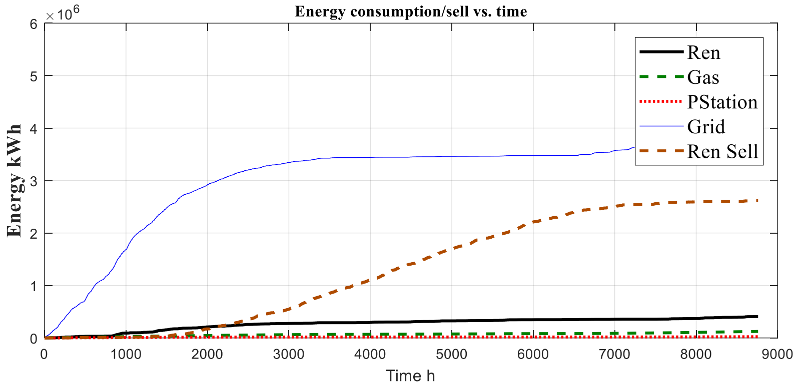

Fig. 6 Energy consumption from different sources vs. time (1st scenario)

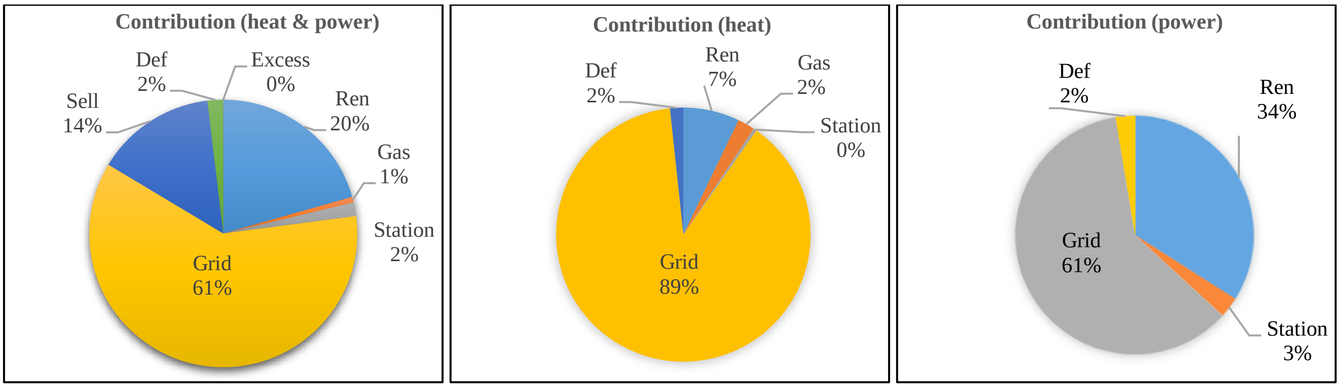

(a) (b) (c)

Fig. 7 Contribution percentage of different energy sources (1st scenario) to (a) total load (heat and power), (b) heat load, and (c) power load. Scenario I (Interest rate is set to zero)

Fig. 8 shows the prices of energy from each source (considering the initial and running cost), the total average cost, and the carbon dioxide cost.

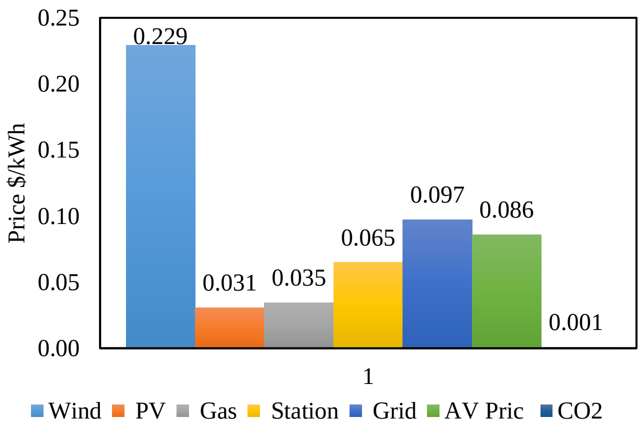

Fig. 8 Energy prices for 1st scenario (interest rate is set to zero)

PV recorded the minimum kWh cost; however, the optimization process didn't favor PV over the conventional energy sources (grid).This is because of the mismatch between the PV energy generation profile and the load profile in addition to a large gap between selling and buying prices from and to the grid (sell price set to 2.5 cents while grid energy price ranges from 8-12 cents). Hence, any increase in PV size would have a negligible effect on the prices of consumed energy per kWh. The figure also indicates that the prices of energy generated by wind turbines are very high. This is due to its high initial cost. However, the wind energy profile has less mismatch with the load profile than PV. Accordingly, wind turbines were among the energy technologies of optimized MEG. It should be noted that the emission cost per kWh is referred to the total generated energy from all sources. Hence, with low share of the furnace in the system, this figure is very small.

5.2 Scenario II

An additional scenario was performed to address the impact of the high initial cost of energy technology on the structure of the optimal MEG by setting high-interest rates (5.25%). It also addresses the effect of high-interest rates on the progress of renewables in any power system. Fig. 9 shows the optimization results of the second scenario as discussed in the first scenario. The results of the best individual over a generation are listed in Table 5. The table shows how the optimization algorithm reduces the use of renewables over generations due to the high interest rates. The lag of renewables was compensated by the grid and the gas. However, the fitness of the fifth generation is very close to the eighth generation with higher share of renewables (note that the total cost of kWh is the addition of the kWh price plus the emission cost).

Table 5 Results of optimization over generations (second scenario, interest rate = 5.25%)

Generation	WT (kW)	PV (kW)	Transformer (MW)	Furnace (kW)	Price ($/kW)	Emission Cost ($/kW)	E_def ratio	E_excess ratio	Fitness
1	6032	3692	5	21564	0.245	0.040	0.020	0.009	3.181
2	572	3691	5	21564	0.129	0.062	0.020	0.000	4.742
3	270	3217	6	1105	0.111	0.036	0.020	0.000	5.963
4	550	3699	3	1105	0.124	0.035	0.029	0.001	5.302
5	270	3866	6	334	0.130	0.010	0.020	0.000	6.201
6	572	3516	9	829	0.128	0.026	0.020	0.000	5.729
7	297	3806	4	6	0.137	0.000	0.032	0.000	5.883
8	407	25	8	829	0.093	0.029	0.020	0.000	7.002

Fig. 9(b) shows that the KPIs are kept nearly the same. The energy consumption from renewable sources was reduced compared with scenario I as can be noted in Fig. 10. Fig. 11 presents a full image of the impact of high-interest rates on MEG structure. It shows that the renewables contribution shrinks to 2%. The gas and grid contribution increased significantly (93%). Fig. 12 presents the prices of energy kWh generated by each technology. The PV kWh prices went higher than first scenario. The contribution of the privet station in both scenarios is the same. This is due to the limited power offered by the station. However, it also indicates the importance of additional sources that can reduce the mismatch between generation and demand profiles.

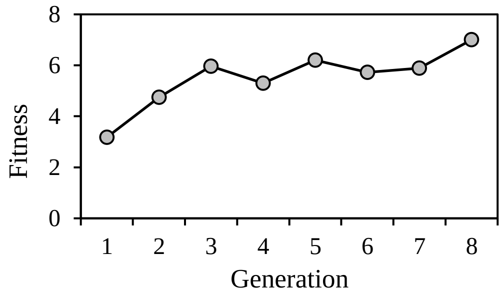

(a)

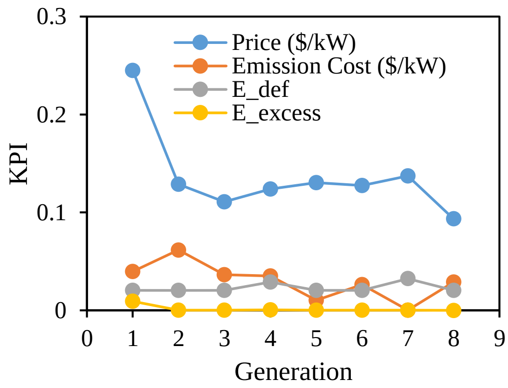

(b)

Fig. 9 Optimization results for 2nd scenario (a) Fitness VS generations (b) KPIs of best individual vs. generation

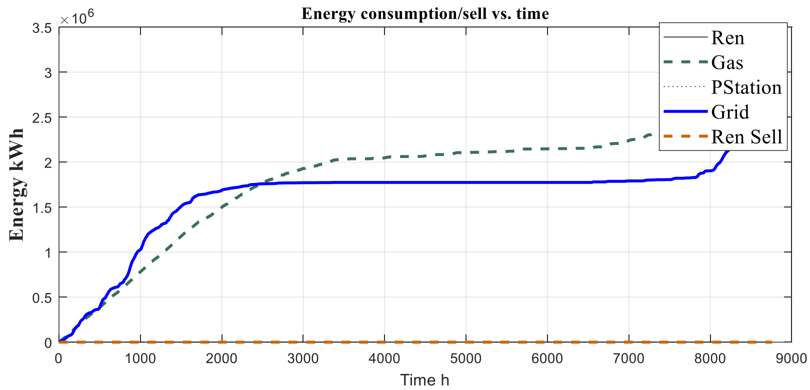

Fig. 10 Energy consumption from different sources vs. time (2nd scenario)

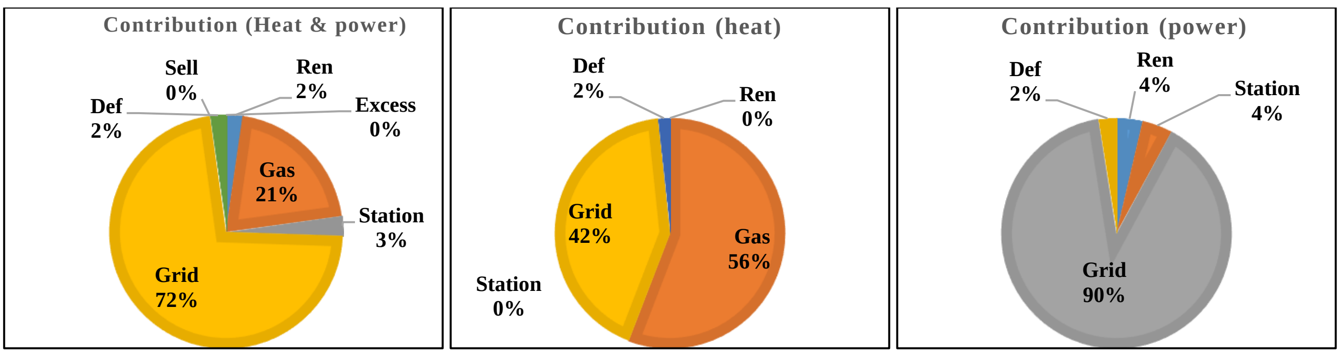

(a) (b) (c)

Fig. 11 Contribution percentage of different energy sources (2nd scenario) to (a) total load (heat and power), (b) heat load, and (c) power load. Scenario II (Interest rate is set to 5.25%)

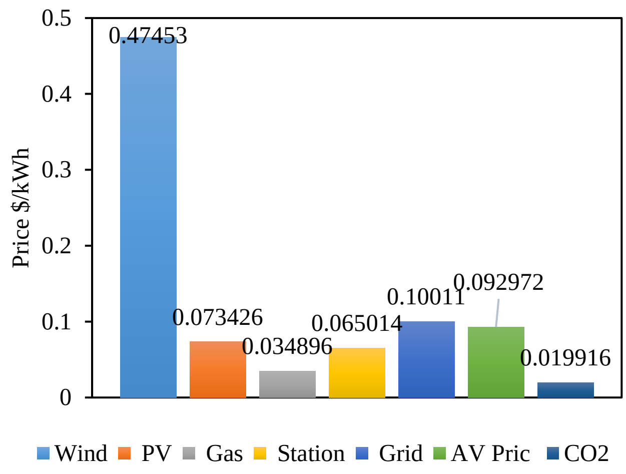

Fig. 12 Energy prices for 2nd scenario (interest rate is set at 5.25%)

Fig. 13 shows the system response for the heat power by applying the two control loops with algorithms presented in section 4. It shows how the control loops ensures close matching between the demand and supply. The control algorithms are applied during the optimization process which insures optimal structure and operation.

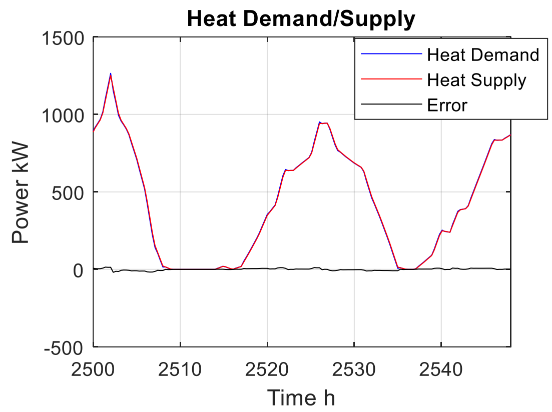

(a)

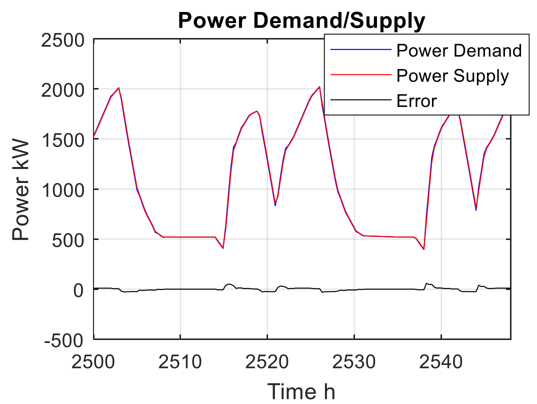

(b)

Fig. 13 The control system response (a) for heat control loop and (b) for power control loop

Table 6 represents the size of each energy technology resulting from the optimization process for the different scenarios.

Table 6 Result of optimization for different scenarios

Scenario	I	II
Total WT size (kW)	100	407
Total size PV (kW)	3215.5	24.75
Furnace (kBtut/h)	88	2830
Grid Transformer size (kW)	5000	4000

6 Conclusions

In this paper, an optimization process to the structure of MEG in grid-connected mode is performed. The optimization objective focused on minimizing cost, carbon dioxide emission, and energy deficiency. The optimized structure was subjected to a scheduling algorithm that guarantee low-price operation considering the availability. In addition, closed-loop feedback operation using a PI controller is implemented at a low control level for both heat and power loops. The control loops guarantee dynamic matching between the demand profile and the supply profile. The results of the optimization and operation of the MEG are presented in two scenarios. The first scenario considers 0% interest rates while the second scenario presents 5.25% interest rates. The results show that due to the high initial prices of renewables (especially WT), their contribution is reduced due to the high-interest rates. In addition, the mismatch between the renewables production profile and load profile, as well as, the low exporting tariff, have a negative impact on renewables' share in the power system. This is evident when we compare the low LCOE for PV with other sources used in this work. Moreover, the addition of a carbon tax effectively reduces the share of gas as a source of energy.

References

[1] Eckhart M., El-Ashry M., Hales D., Hamilton K., and Rae P., 2020 "Renewables, Global Status report," REN21.

[2] Eckhart M., El-Ashry M., Hales D., Hamilton K., and Rae P., 2018 "Renewables, Global Status report," REN21.

[3] "Summary Report: 2012 DOE Microgrid Workshop.," 2012.

[4] Parhizi, S., Lotfi, H., Khodaei, A. and Bahramirad, S., 2015. State of the art in research on microgrids: A review. IEEE access, 3, pp.890-925.

[5] Ma, T., Wu, J. and Hao, L., 2017. Energy flow modeling and optimal operation analysis of the micro energy grid based on energy hub. Energy conversion and management, 133, pp.292-306.

[6] Gabbar, H.A. and Zidan, A., 2016. Optimal scheduling of interconnected micro energy grids with multiple fuel options. Sustainable Energy, Grids and Networks, 7, pp.80-89.

[7] Han, Y. and Shen, P., 2014. Modeling, control and electromagnetic transient simulation of the doubly fed induction generator-based wind energy generation system. Simulation, 90(3), pp.275-289.

[8] Katzenbach, R., Clauss, F. and Zheng, J., 2015, May. Potentials of sustainable energy management in buildings. In 2015 5th International Youth Conference on Energy (IYCE) (pp. 1-7). IEEE.

[9] Luque, A. and Hegedus, S. eds., 2011. Handbook of photovoltaic science and engineering. John Wiley & Sons.

[10] Jiang, X. and Xiao, C., 2019. Household energy demand management strategy based on operating power by genetic algorithm. IEEE Access, 7, pp.96414-96423.

[11] Raghavan, A., Maan, P. and Shenoy, A.K., 2020. Optimization of day-ahead energy storage system scheduling in microgrid using genetic algorithm and particle swarm optimization. Ieee Access, 8, pp.173068-173078.

[12] Teo, T.T., Logenthiran, T., Woo, W.L., Abidi, K., John, T., Wade, N.S., Greenwood, D.M., Patsios, C. and Taylor, P.C., 2020. Optimization of fuzzy energy-management system for grid-connected microgrid using NSGA-II. IEEE transactions on cybernetics, 51(11), pp.5375-5386.

[13] Moghaddam, A.A., Seifi, A., Niknam, T. and Pahlavani, M.R.A., 2011. Multi-objective operation management of a renewable MG (micro-grid) with back-up micro-turbine/fuel cell/battery hybrid power source. energy, 36(11), pp.6490-6507.

[14] Díaz, G., Planas, E., Andreu, J. and Kortabarria, I., 2015. Joint cost of energy under an optimal economic policy of hybrid power systems subject to uncertainty. Energy, 88, pp.837-848.

[15] Zare, M., Niknam, T., Azizipanah-Abarghooee, R. and Ostadi, A., 2016. New stochastic bi-objective optimal cost and chance of operation management approach for smart microgrid. IEEE Transactions on Industrial Informatics, 12(6), pp.2031-2040.

[16] Kouloura, T.C., Genikomsakis, K.N. and Protopapas, A.L., Systemic assessment of measures for sustainable energy management in buildings: The case of a student dormitory, ECOS2006, Crete-Greece, July 2006. In Conference Proceedings (pp. 861-868).

[17] Zidan, A., Gabbar, H.A. and Eldessouky, A., 2015. Optimal planning of combined heat and power systems within microgrids. Energy, 93, pp.235-244.

[18] International Energy Agency, 2022. Renewable Energy Market Update: Outlook for 2022 and 2023. OECD Publishing.

[19] Spertino, F., Di Leo, P., Ilie, I.S. and Chicco, G., 2012. DFIG equivalent circuit and mismatch assessment between manufacturer and experimental power-wind speed curves. Renewable Energy, 48, pp.333-343.

[20] Wiser, R.H. and Bolinger, M., 2019. 2018 wind technologies market report.

[21] Siyal, S.H., Mentis, D. and Howells, M., 2016. Mapping key economic indicators of onshore wind energy in Sweden by using a geospatial methodology. Energy conversion and management, 128, pp.211-226.

[22] Davis M., Sylvia L.M., Zoe G., Sagar C., Caitlin C., Matthew S., Matt I., Elissa P., and Chris S., "Solar Market Insight Report 2022 Year in Review," Solar Energy Industries Association (SEIA), Washington,, 2022.

[23] REN21, P.R.S., 2022. Renewables 2022 global status report. Renewable Energy Policy Network for the 21st Century (REN21).

[24] Feldman, D., Ramasamy, V., Fu, R., Ramdas, A., Desai, J. and Margolis, R., 2021. US solar photovoltaic system and energy storage cost benchmark (Q1 2020) (No. NREL/TP-6A20-77324). National Renewable Energy Lab.(NREL), Golden, CO (United States).

[25] Tjengdrawira, C. and Richter, M., 2016. Review and Gap Analyses of Technical Assumptions in PV Electricity Cost Report on Current Practices in How Technical Assumptions Are Accounted in PV Investment Cost Calculation. No. Solar Bankability WP3 Deliverable D, 3.

[26] Ufluoğlu, E.E. and Kayakutlu, G., 2016. Mathematical model for a microgrid consisting of wind turbine, PV panels, and energy storage unit. Journal of Renewable and Sustainable Energy, 8(5).

[27] Feldman, D., Ramasamy, V., Fu, R., Ramdas, A., Desai, J., and Margolis, R., 2021. U.S. Solar Photovoltaic System Cost Benchmark: Q1 2020. Golden, CO: National Renewable Energy Laboratory. NREL/TP-6A20-77324.

[28] How much does it cost to install an electric furnace? Fixr.com | Electric Furnace Cost | Electric Furnace Replacement Cost. Available at: https://www.fixr.com/costs/electric-furnace.

[29] Canada, E. and C.C. (2021) Government of Canada, Canada.ca. Available at: https://www.canada.ca/en/environment-climate-change/services/climate-change/pricing-pollution-how-it-will-work/industry/pricing-carbon-pollution.html.

[30] "Heating with electricity," Natural Resources Canada's, Office of Energy Efficiency, 2003. https://natural-resources.canada.ca/sites/www.nrcan.gc.ca/files/energy/pdf/energystar/Heating_with_Electricity.pdf

[31] NSRDB. Available at: https://nsrdb.nrel.gov/.

This page is left intentionally blank

Journal of Engineering Advancements (JEA)
DOI: https://doi.org/10.38032/jea

Indexed by:

Volume 04 Issue 03

DOI: https://doi.org/10.38032/jea.2023.03

Published by: SciEn Publishing Group
Website: www.scienpg.com